

PROCESSING AND MECHANICAL BEHAVIOR OF  
POWDER METALLURGY (PM) TI-6AL-4V  
ALLOY MADE FROM  $\text{TiH}_2$

by

Pankaj Kumar

A dissertation submitted to the faculty of  
The University of Utah  
in partial fulfillment of the requirements for the degree of

Doctor of Philosophy

Department of Metallurgical Engineering

The University of Utah

December 2016

Copyright © Pankaj Kumar 2016

All Rights Reserved

# **The University of Utah Graduate School**

## **STATEMENT OF DISSERTATION APPROVAL**

The dissertation of **Pankaj Kumar**  
has been approved by the following supervisory committee members:

<u><b>Ravi Chandran</b></u>	, Chair	<u><b>8/16/2016</b></u> Date Approved
<u><b>Zhigang Zak Fang</b></u>	, Member	<u><b>8/16/2016</b></u> Date Approved
<u><b>Sivaraman Guruswamy</b></u>	, Member	<u><b>8/16/2016</b></u> Date Approved
<u><b>Dinesh K. Shetty</b></u>	, Member	<u><b>8/16/2016</b></u> Date Approved
<u><b>Ashley Spear</b></u>	, Member	<u><b>8/22/2016</b></u> Date Approved

and by **Manoranjan Misra**, Chair/Dean of  
the Department/College/School of **Metallurgical Engineering**

and by David B. Kieda, Dean of The Graduate School.

## **ABSTRACT**

Powder metallurgy (PM) offers a cost-effective approach to produce titanium alloys in near net shape. Conventionally, two general processes have been followed to produce PM titanium alloys: Blended Elements (BE) and the Pre-Alloyed (PA) methods. Cost considerations, however, favor BE over the PA method. BE titanium alloy products are typically characterized by a significant amount of residual porosity. In general, porosity adversely affects the mechanical properties in PM titanium. Porosity acts as stress concentration sites and, at the same time, reduces the load bearing area, which leads to decrease in both the tensile strength and ductility of the material. Pores also have a greater effect in reducing the fatigue life of PM titanium. In order to improve the mechanical properties, porosity needs to be reduced or eliminated. It has been shown that effective densification and therefore improvement in mechanical properties of titanium alloys can be achieved through the use of  $\text{TiH}_2$  powder.

In the first part of the present work, the effects of powder processing and sintering on tensile properties of PM Ti-6Al-4V alloy processes by a newly developed PM process based on  $\text{TiH}_2$ , called “hydrogen sintering and phase transformation (HSPT)”, have been examined. The investigation is aimed at the effect of  $\text{TiH}_2$  particle size and sintering time on the tensile properties of HSPT-processed Ti-6Al-4V. Very fine powder particles lead to enhance densification but increase the interstitial element, leading to reduced ductility of the PM alloy. An increase in sintering time improves the tensile ductility



by reducing the pore size, without affecting the strength of the alloy. In the second part of the present work, the effect of residual pores on the tensile properties of PM Ti-6Al-4V alloys processed by HSPT has been examined. The primary objective is to establish a relation between tensile ductility of the HSPT-processed Ti-6Al-4V and the extreme-sized pores present as a part of the low-volume-fraction porosity in the material. Even though each sample is similar to the other in terms of average volume-fraction porosity, there was unusually large variation in ductility from sample to sample. It is observed that the extreme-sized pores actually control the ductility of the PM Ti-6Al-4V alloy. A strong correlation has been found between the extreme pore size and tensile ductility. A mathematical model is developed to predict the influence of the extreme-sized pores on the tensile ductility based on the assumption that the pore-containing area yields, causing strain concentration and early crack initiation.

A new sintering approach to enhance densification of PM Ti-6Al-4V alloy is investigated in the last part of this work. The hypothesis of the approach is that the continuous phase transition (between  $\alpha$  and  $\beta$ ) leads to strain due to volume change during phase transformation in addition to the enhanced self-diffusivity of titanium, thereby accelerating the sintering kinetics. A phase reversal experiment was performed by cyclic sintering across the phase transition temperature (1010°C) of Ti-6Al-4V alloy. It was found that thermal cyclic across alpha ( $\alpha$ )-beta ( $\beta$ ) transition temperature led to a reduction in residual porosity. A mechanical properties evaluation of Ti-6Al-4V alloy indicated an improved mechanical properties (tensile and fatigue) compared to the conventional vacuum-sintered Ti-6Al-4V alloy.

## TABLE OF CONTENTS

ABSTRACT.....	iii
LIST OF TABLES .....	viii
ACKNOWLEDGEMENTS .....	ix
Chapters	
1. INTRODUCTION .....	1
1.1 Background .....	2
1.2 Objectives of the Present Research .....	5
1.3 References .....	5
2. LITERATURE REVIEW .....	8
2.1 Introduction .....	9
2.1.1 The Blended-Element Method .....	10
2.1.2 Pre-alloyed Powder Method .....	11
2.1.3 PM Methods Based on Titanium Hydride Powder .....	13
2.2 Relative Merits of Processing Approaches for PM Ti-6Al-4V Alloy .....	14
2.3 Microstructure of PM Ti-6Al-4V Alloys .....	17
2.4 Tensile Properties of PM Ti-6Al-4V Alloy .....	20
2.4.1 Strength-Ductility Map of PM Ti-6Al-4V Alloy .....	20
2.4.2 Factors Affecting Strength-Ductility of BE PM Ti-6Al-4V Alloy .....	21
2.4.2.1 Effect of Density and Purity .....	22
2.4.2.2 Effect of Post Sintering Treatment .....	23
2.4.3 Factors Affecting Strength-Ductility of PA PM Ti-6Al-4V Alloy .....	24
2.4.3.1 The Role of Microstructure and Heat Treatment .....	25
2.5 The Specific Effects of Porosity on Tensile Properties of PM Ti-6Al-4V .....	27
2.5.1 Effect on Tensile Strength .....	27
2.5.2 Effect on Tensile Ductility .....	29
2.5.3 Strength-Ductility Maps at Constant Microstructure .....	32
2.6 Microstructure Factors Affecting Tensile Properties .....	33
2.7 Effect of Manufacturing Process on the Tensile Properties .....	36
2.8 Summary .....	40
2.9 Acknowledgement .....	42

2.10 References .....	52
3. MATERIALS AND EXPERIMENTAL PROCEDURE.....	63
3.1 Starting Powder Preparation .....	64
3.2 Powder Compaction.....	64
3.3 Sintering.....	65
3.3.1 Hydrogen Sintering and Phase Transformation (HSPT) Processing.....	65
3.3.2 Thermal Cyclic Sintering .....	66
3.3.3 Isothermal Vacuum Sintering.....	66
3.4 Density and Chemical Analysis .....	66
3.5 Microstructure Analysis.....	67
3.6 Mechanical Testing and Fractography.....	67
4. EFFECTS OF POWDER PROCESSING AND SINTERING ON TENSILE DUCTILITY OF PM Ti-6Al-4V ALLOY MADE BY HYDROGEN SINTERING OF TITANIUM HYDRIDE POWDERS.....	71
4.1 Introduction.....	72
4.2 Experimental Procedure.....	72
4.3 Results and Discussion .....	73
4.4 Conclusions.....	75
4.5 References .....	75
5. THE NATURE OF TENSILE DUCTILITY AS CONTROLLED BY EXTREME- SIZED PORES IN POWDER METALLURGY Ti-6Al-4V ALLOY .....	77
5.1 Introduction.....	78
5.2 Experimental Procedures .....	79
5.3 Results .....	80
5.3.1 Microstructure .....	80
5.3.2 Tensile Properties .....	81
5.4 Discussion.....	83
5.4.1 Effect of Porosity on Strength .....	83
5.4.2 Effect of Porosity on Tensile Ductility.....	85
5.4.3 Mechanism of Pore Size Effect on Ductility .....	87
5.5 Conclusions.....	89
5.6 References.....	89
6. A CONSTITUTIVE EQUATION TO PREDICT THE PORE SIZE EFFECT ON TENSILE DUCTILITY OF LOW POROSITY MATERIALS .....	90
6.1 Introduction.....	91
6.2 Mechanism of Fracture Due to Presence of a Large Pore .....	93
6.3 Analytical Model .....	95
6.3.1 Case I: Material Containing Uniformly Distributed Small Pores .....	96

6.3.2 Case II: Material Containing Extreme Size Pore .....	97
6.3.3 Fracture Conditions .....	98
6.4 Stress Concentration Factor .....	99
6.5 Comparison with Experimental Data.....	100
6.6 Effect of Strain Hardening on Prediction of Tensile Ductility .....	102
6.7 Conclusions.....	104
6.8 References.....	110
 7. ACCELERATED SINTERING OF POWDER METALLURGY TI-6AL-4V ALLOY BY REPEATED PHASE TRANSFORMATION INDUCED BY THERMAL CYCLING .....	112
7.1 Introduction.....	113
7.2 Experimental Procedure.....	115
7.3 Results and Discussion .....	117
7.3.1 Thermal Cycling and Isothermal Densification .....	117
7.3.2 Microstructure .....	121
7.3.3 Tensile Properties .....	123
7.3.4 Fatigue Performance.....	126
7.4 Conclusions.....	128
7.5 References.....	146
 8. CONCLUSIONS.....	150

## LIST OF TABLES

2.1	Room-temperature tensile properties of lamellar PM Ti-6Al-4V alloy at various density levels.....	43
2.2	Room-temperature tensile properties of lamellar PM Ti-6Al-4V alloy at specific microstructure conditions.....	44
2.3	Room-temperature tensile properties of lamellar PM Ti-6Al-4V alloy made from different initial powders .....	45
4.1	Chemical composition of HSPT Ti-6Al-4V alloys.....	73
4.2	Effect of TiH <sub>2</sub> particle size on the density and oxygen content of HSPT processed Ti-6Al-4V .....	73
4.3	Tensile properties of HSPT Ti-6Al-4V samples.....	74
5.1	Chemical composition of HSPT-Processed Ti-6Al-4V .....	79
5.2	Tensile Properties of HSPT-Processed Ti-6Al-4V samples .....	83
6.1	Parameters used for the prediction of pore size effect on the tensile ductility of cast and PM alloys .....	105
7.1	Chemical composition of vacuum-sintered PM Ti-6Al-4V.....	130
7.2	Density of PM Ti-6Al-4V alloy obtained in three different conditions .....	130
7.3	Summary of tensile properties obtained for isothermal sintered compared with cyclic sintered PM Ti-6Al-4V .....	131

## **ACKNOWLEDGEMENTS**

I take this opportunity to express my sincere gratitude to my advisor, Prof. K.S. Ravi Chandran, for providing me an opportunity to work on this project. His constant guidance and encouragement, and easily approachable personality made my project work experience really enjoyable.

I would like to thank, Prof. Z. Zak Fang for allowing me his facilities to carry out my experiments, and serving on my supervisory committee. I am also thankful to Dr. Sivaraman Guruswamy, Dr. Ashley Spear, and Dr. Dinesh K. Shetty for serving on my supervisory committee. I extend my unlimited thanks to Pei, James, Mark, Matt, Lu, and my lab mates Fei, Yuxuan, Bhaskar, and Madhusudan for their constant support in carrying out my project work and taking their time to help me in getting things done. I express my sincere thanks to James Paramore for his help in setting up the furnace facility. I am also thankful to Kay, Evelyn, and Sara Wilson for administrative support.

Last but not least, I need to thank my parents and sisters for their continued faith in my abilities, their support, and their love, of which I have been the fortunate recipient throughout my life.

Finally, I would like to acknowledge the financial grant from the U.S. Department of Energy, Innovative Manufacturing Office and the Office of Energy Efficiency and Renewable Energy, which made this project possible. The initial raw titanium hydride and aluminum-vanadium powders were supplied by Reading Alloys (AMETEK), USA.

## **CHAPTER 1**

### **INTRODUCTION**

## 1.1 Background

Titanium materials are important engineering materials for structural applications. Despite its excellent structural properties, use of titanium is restricted to a few engineering applications such as aerospace and chemical and medical devices. The common reason for its limited application is its cost. It was pointed out that most of the cost of titanium comes from the cost of manufacturing processing [1]. The raw material cost accounts only for 4% of the total cost of titanium [2]. Since the production and manufacturing of titanium is expensive, its use is limited to high-end engineering applications. Powder metallurgy (PM) processing method, on the other hand, proved to be cost effective, and has been used as an alternative to the conventional processing for titanium [3].

Conventionally, PM titanium and its alloy product follow two general processing methods: Blended Elements (BE) and the Pre-Alloyed (PA) methods [4]. In BE method, the raw powders are blended, compressed, and then sintered. The amount of residual porosity in the final product, however, is large, which ultimately dictates the poor mechanical properties. On the other hand, the PA process uses the pre-alloyed powder to sinter. Though the properties of the final product of the PA process are better than the BE-processed materials, the processing is not cost effective. Therefore, the BE method is preferred over the PA method.

Different alternatives have been tried and applied to reduce the residual porosity in BE product. In recent years, vacuum sintering of  $\text{TiH}_2$  powder emerged as a prevailing technique to produce near porosity-free titanium and its alloy. People have shown the improved sinterability, low residual porosity, and better mechanical properties in titanium



processed by vacuum sintering of  $\text{TiH}_2$  powders [5]. The improved porosity level in the final product has been attributed partially to the hydrogen cleaning of the surfaces during sintering. In addition, hydrogen refines and thus modifies the microstructure of the material, therefore improving the properties. By taking advantage of hydrogen as a temporary alloying element, a new method has been recently introduced to produce fully densified BE product [6]. This process uses a controlled hydrogen atmosphere to sinter the  $\text{TiH}_2$  powder instead of using vacuum sintering. This process is thus called the Hydrogen Sintering and Phase Transformation (HSPT) process. This process is able to produce fully densified and fine microstructure of Ti and its alloys.

Though we can produce high-density PM product, the residual porosity has always been a concern in PM materials. It is well known that the PM-processed components may exhibit different mechanical properties (fracture-related properties) despite having the same processing conditions, average microstructure, and alloy chemistry. The variability can be attributed to the defects present in the materials. As we know in PM materials, porosity contributes the major part of the defect and thus controls the properties of the materials. Several studies have related the effect of porosity on the mechanical properties in various material systems [7–13]. Porosity in materials greatly affects the ductility of the materials. Similar processed components exhibit different ductility levels. Caceres et al. [14] describe a relationship between the ductility and area fraction of porosity. Power-law-type expression is proposed by Gokhale et al. [8] to correlate the tensile ductility and area fraction of porosity in cast Al alloys. Note that all the studies above are focused on the effect of total area fraction of defects on the fracture surface on the tensile ductility. But as we know, the fracture is a highly localized phenomenon, i.e., a crack tends to form

in the weakest cross-section from a large pore. Strain localization at pores leads to early crack initiation, thus limiting the plastic deformation, i.e., the ductility of the materials and the fatigue life. There are pores that are big enough to act as fracture initiation sites during applications. These pores are not part of the average microstructure but occur due to rare events during processing.

Also, processing variables such as initial particle size, impurities, sintering temperature, and time have significant effect on the amount of residual porosity, and consequently the tensile properties of PM titanium change. It would be interesting to study how raw particle size and sintering parameter affect the tensile properties of a PM titanium alloy.

One of the objectives of this research is to systematically study of how the residual pores at low-volume fraction affect the tensile properties of HSPT-processed PM Ti-6Al-4V alloy. The pore size distribution and pore morphology are also investigated as part of the study. A theoretical model based on the local strain concentration needs to be developed to quantitatively illustrate the effect of residual pore on the tensile properties. In addition, effects of powder process and sintering on tensile properties of PM Ti-6Al-4V alloy processes by HSPT are studied.

A unique characteristic of HCP transition metals like titanium is that they show anomalous diffusion behavior at phase transition temperature. In these metals, the self-diffusivities are anomalous higher than at other temperatures, and thus do not follow the Arrhenius law of diffusion [15]. On this basis, one of the hypotheses of this work is that that diffusivity enhancement at phase transition temperature should cause rapid densification at this temperature. The various sintering conditions near phase transition

temperature and their effectiveness in accelerating the densification are investigated in this research.

## **1.2 Objectives of the Present Research**

The general objective of this research is to investigate the processing effects on the microstructure and, consequently, the mechanical properties of PM Ti-6Al-4V alloy. The key objectives are the following:

1. Establish relationship between powder processing, sintering and tensile properties of PM Ti-6Al-4V alloy made by HSPT process.
2. Determine the process variables and the microstructural constituents affecting the tensile properties of PM Ti-6Al-4V alloy. The possible mechanisms responsible for the varying tensile properties are also to be determined.
3. Develop a quantitative model that can explain the tensile behavior with the microstructural discontinuities such as porosity in PM Ti-6Al-4V alloy.
4. Investigate the process that can enhance the sintering kinetics and therefore improve the mechanical properties, including the mechanisms responsible for the sintering kinetics caused during the sintering, and its effect on densification of the PM Ti-6Al-4V alloy.

## **1.3 References**

- [1] V.C. Petersen, V.K. Chandhok, C.A. Kelto, Hot isostatic pressing of large titanium shapes, in: F.H. Froes, J.E. Smugeresky (Eds.), Powder Metall. Titan. Alloy., A.I.M.E, Warrendale, PA, USA, 1980: pp. 243–254.
- [2] A.D. Hartman, S.J. Gerdemann, J.S. Hansen, Producing lower-cost titanium for automotive applications, Jom. 50 (1998) 16–19. doi:10.1007/s11837-998-0408-1.

- [3] I.S. Polkin, V.N. Samarov, Advances in Powder Metallurgy of Titanium, in: Ti-2011, Beijing, China, 2011: pp. 1817–1820.
- [4] F.H. Froes, D. Eylon, Powder metallurgy of titanium alloys, *Int. Mater. Rev.* 35 (1990) 162–184. doi:10.1179/095066090790323984.
- [5] O.M. Ivasishin, D.G. Savvakina, F.H. Froes, V.S. Mokson, K. Bondareva, Synthesis of the Ti-6 Al-4 V alloy having low residual porosity by powder metallurgy method, *Poroshkovaya Metall.* 7 (2002) 54–64.
- [6] Z.Z. Fang, P. Sun, H. Wang, Hydrogen Sintering of Titanium to Produce High Density Fine Grain Titanium Alloys, *Adv. Eng. Mater.* 14 (2012) 383–387. doi:10.1002/adem.201100269.
- [7] G.W. Mugica, D.O. Tovio, J.C. Cuyas, A.C. González, Effect of porosity on the tensile properties of low ductility aluminum alloys, *Mater. Res.* 7 (2004) 221–229. doi:10.1590/S1516-14392004000200002.
- [8] A.M. Gokhale, G.R. Patel, Origins of variability in the fracture-related mechanical properties of a tilt-pour-permanent-mold cast Al-alloy, *Scr. Mater.* 52 (2005) 237–241. doi:10.1016/j.scriptamat.2004.09.011.
- [9] H. Mae, X. Teng, Y. Bai, T. Wierzbicki, Relationships between Material Ductility and Characteristic Size of Porosity Correlated before/after Testing of a Cast Aluminum Alloy, *J. Solid Mech. Mater. Eng.* 2 (2008) 924–942. doi:10.1299/jmmp.2.924.
- [10] R. Haynes, A study of the effect of porosity content on the ductility of sintered metals, *Powder Metall.* 20 (1977) 17–20.
- [11] Y. Yan, G.L. Nash, P. Nash, Effect of density and pore morphology on fatigue properties of sintered Ti–6Al–4V, *Int. J. Fatigue.* 55 (2013) 81–91. doi:10.1016/j.ijfatigue.2013.05.015.
- [12] P. Kumar, K.S. Ravichandran, F. Cao, P. Sun, M. Koopman, Z.Z. Fang, Effects of Powder Processing and Sintering on Tensile Ductility of Pm Ti-6Al-4V Alloy Made by Hydrogen Sintering of Titanium Hydride Powders, in: Ti-2015 Sci. Technol., The Minerals, Metals and Materials Society, 2015: pp. 1355–1359.
- [13] M. Hagiwara, Y. Kaieda, Y. Kawabe, S. Miura, Fatigue Property Enhancement of .ALPHA.-.BETA. Titanium Alloys by Blended Elemental P/M Approach., *ISIJ Int.* 31 (1991) 922–930. doi:10.2355/isijinternational.31.922.
- [14] C.H. Cáceres, B.I. Selling, Casting defects and the tensile properties of an AlSiMg alloy, *Mater. Sci. Eng. A.* 220 (1996) 109–116. doi:10.1016/S0921-5093(96)10433-0.
- [15] B. Sarma, Accelerated Kinetics and Mechanics of Growth of Boride layers on

Titanium under Isothermal and Cyclic Diffusion, PhD Thesis, University of Utah, 2011.

## **CHAPTER 2**

### **LITERATURE REVIEW**

Submitted for publication as:

P. Kumar and K.S. Ravi Chandran

Strength-Ductility Property Maps of Powder Metallurgy (PM) Ti-6Al-4V Alloy: A

Critical Review of Processing-Structure-Property Relationships

Metallurgical and Materials Transaction A, 2016

.

## 2.1 Introduction

Titanium alloys are attractive for light-weight structural applications due to their relatively high specific stiffness and strength properties, good creep resistance, and excellent corrosion resistance [1,2]. Despite the excellent combination of physical and mechanical properties both at ambient and elevated temperature, extensive usage of titanium is limited to high-value aerospace and chemical industry applications. This is largely due to the relatively high costs of the finished titanium products. While the raw material cost is relatively high, a large portion of the total cost of manufacturing titanium components is actually associated with the machining of wrought material into the finished components [3]. A study [4] indicates that about 30% of the total cost of titanium is spent in machining rough-forged titanium components to final product forms. This figure, put in perspective, is notably higher than the cost of metal charge and casting combined (26%). In addition, the total utilization factor (defined as the weight percentage of raw material that becomes the final component) for machining rough-forged components to finish product is about 17% [5]. The combined material loss and fabrication costs inevitably increase the total cost of titanium components. Therefore, production of near net-shape (NNS) titanium components is a very attractive option to reduce the overall cost of the titanium product, especially if the material loss in machining can be largely minimized.

Powder metallurgy (PM) is the principal NNS manufacturing process that has the potential to reduce the material loss, processing steps, and fabrication costs associated with the wrought forms. The PM approach to making sintered titanium compacts was first reported by Kroll [6] in the late 1940s. However, the presence of residual impurities,

especially magnesium chloride in the alloy, severely degraded the mechanical properties and the weldability of titanium alloy [7,8]. Abkowitz et al. [8] studied the effect of chlorine on the mechanical properties of PM Ti-6Al-4V alloy. A significant improvement in density and mechanical properties, especially fatigue strength, was shown when the chloride content was decreased from 0.16 wt.% to 0.016 wt.%. However, the titanium PM route was not pursued widely due to the lack of approaches to produce high-purity titanium powder at that time.

Since Kroll's work, several studies have focused on developing further the PM approach for titanium. The primary goal is to reduce cost and material loss in manufacturing, with the need to improve mechanical properties playing a secondary role. If a commercial NNS-processed PM Ti-6Al-4V alloy could be made at a much-reduced cost, with properties roughly equivalent to the wrought forms, then the hurdles to practical applications will be minimal. With this broader objective, various techniques were developed, first, for the production of high purity titanium alloy powder in 1980s. Secondly, two manufacturing approaches were pursued in order to establish PM of titanium alloys as a low-cost manufacturing technique. One is the blended elemental (BE) method and the other is the pre-alloyed (PA) powder method [9–11]. Prototype components of titanium were made using PM and cost minimization strategies have been demonstrated [12,13].

### **2.1.1 The Blended-Element Method**

The BE method refers to the process of cold pressing of blended elemental powders followed by sintering at a temperature higher than the beta-transus temperature. The



desired alloy composition is attained by mechanically blending the elemental titanium powder and the powders of alloy elements. The blended powder is then pressed into desired shapes and then pressure-less sintered at high temperature, usually in the beta-phase field, in order to homogenize the microstructure with respect to the high-melting-point alloying elements such as V, Mo, Cr, etc. A titanium component produced by the BE method generally tends to have poor mechanical properties, primarily due to a significant residual porosity (94% relative density), coarse microstructure (lamellar colonies with large prior-beta grains), and impurities from the initial powders [7,14]. A major disadvantage of this approach is that the microstructure of the BE PM titanium alloy cannot be refined further without any additional mechanical working, which would very likely increase the cost of the final PM product. In general, the BE PM Ti-6Al-4V alloys have subpar mechanical properties compared to wrought Ti-6Al-4V, especially fatigue strength.

### **2.1.2 Pre-alloyed Powder Method**

The PA method, on the other hand, has been found to produce components with mechanical properties comparable to those of wrought Ti alloys. It was pursued extensively in the 1980s for the production of Ti-alloy components with superior mechanical properties, especially fatigue strength, the levels of which were often targeted to rival those of the wrought titanium and with an intention of introduction into aerospace applications. This method also uses sintering of pre-alloyed powders in the beta-phase field. This process uses very high-purity pre-alloyed powders made by, for example, the rotating electrode (PREP-plasma rotating electrode process) process [15]. Additionally,

gas-atomization (GA) and electrode-induction-gas-atomization (EIGA) are some of the techniques that have been used to produce spherical pre-alloyed titanium powder [15]. However, the pre-alloyed powders showed poor pressability or deformation characteristics. Hence, they had to be consolidated using pressure-assisted consolidation techniques such as hot iso-static pressing (HIP), to achieve nearly 100% density [16–19].

There is no doubt that the PA method can produce titanium components with properties comparable to those of wrought materials, but the energy consumed in both the powder production and the HIPing steps makes the PA method significantly more expensive than the BE method. Cost consideration therefore strongly favors the BE method over the PA method. Therefore, substantial research efforts, from powder production to postsintering treatments, have been directed to improve the properties of BE titanium. An example is the advancement of the BE approach by the use of low-chlorine titanium powder [20–28]. It is known that a chlorine content of  $> 0.2$  wt% adversely affects the densification process during sintering [8,29,30]. Nearly 100% density in PM compacts was achieved in the BE Ti-6Al-4V alloy using titanium powders with a chlorine content less than 10 ppm [31]. Additionally, several studies have used postsintering thermo-mechanical processing steps, such as hot forging and heat treatment, in an effort to close the residual pores and to increase the levels of mechanical properties [31–34]. It is therefore evident that some form of mechanical working is necessary to bring up the properties of BE PM titanium to the levels of wrought forms—it is the postsintering mechanical working step to close the pores in BE method and it is the HIPing step to consolidate the poorly deformable alloy powders in the PA method. There is no doubt, however, that the postsintering treatments, which are energy intensive,

largely contribute to the increased cost and the complexity of processing steps in PM titanium manufacturing.

### **2.1.3 PM Methods Based on Titanium Hydride Powder**

In this approach, hydrogenated titanium (titanium hydride,  $\text{TiH}_2$ ) powder is used as feedstock to make PM titanium alloy components. In general, hydrogen is considered an unwanted element in titanium alloy, due to the hydrogen embrittlement of titanium at hydrogen concentrations in excess of about 100 ppm. However, due to the high diffusivity of H in Ti and the reversible nature of the hydrogenation reaction, hydrogen can be easily incorporated or removed from a titanium matrix at high temperature. The use of hydrogenated titanium for sintering a niobium-based superconductor alloy was first reported by Gregory in 1969 [35]. Subsequently, a process to make titanium alloy and titanium metal matrix composites using  $\text{TiH}_2$  powder, by hot pressing, was reported and was named, “decomposition sintering” [36]. Obara et al. in 1976 [37] showed that  $\text{TiH}_2$ , blended with alloying elements, can be pressed and sintered between 1273K (1000°C) and 1773K (1500°C) to make PM titanium alloys. Since 2000, significant progress on PM processes based on titanium hydride powder has been made [38–42]. In general, in these studies, an increase in the green density and the green strength of PM compact as well as a significant increase in sintered density, relative to that of conventional PM methods, are often quoted as major advantages [22,43]. Several studies [44–47] have shown that a relatively high-density (>98%) alloy with a highly refined microstructure can be achieved using  $\text{TiH}_2$  powder as feedstock, without using any additional mechanical or heat treatment steps after sintering. Consequently, a significant

increase in tensile and fatigue strengths of PM Ti-6Al-4V alloy, made using  $\text{TiH}_2$  powder, was achieved [48,49]. A detailed discussion of PM processes based on titanium hydride powder is given in section 2.7.

The objective of this review is to present a comprehensive assessment of the tensile property levels that can be achieved in various PM manufacturing approaches of Ti-6Al-4V. The focus is to identify critical raw-material, processing, and microstructural issues that need to be addressed for property improvement, which could help steer further research and development. The present study tries to achieve these objectives by organizing data logically in the form of strength-ductility property maps such that meaningful comparisons can be made. There has not been any previous attempt to collectively present the data in such a format to critically assess the processing-structure-property relationships in PM titanium alloys. The large collection of works compiled in this study have provided ample mechanical property data under varying powder, processing, and microstructural conditions, and they have helped greatly in making this critical assessment.

## **2.2 Relative Merits of Processing Approaches for PM Ti-6Al-4V**

### **Alloy**

A flow sheet of processing routes that have been followed to produce PM titanium alloys is outlined in Figure 2.1. In general, the type of starting powder (BE or PA) and the number of PM processing steps greatly influence the microstructure and the mechanical properties of PM titanium alloys. In general, in the BE approach, three different approaches have been followed.

First, traditionally, the BE methods have used powders made by crushing and milling of Ti sponge [50] or by melting and gas atomization [51], as the feedstock. The melting and atomization may use either pure or alloy melt to produce the required powder. However, in pure form Ti sponge is very ductile and very difficult to produce powders of the required mesh size for PM processing. Melting and gas atomization (GA) of Ti sponge or alloy adds to the cost of processing. Hence this approach, although one of the feasible methods of making PM Ti alloys, is rarely practiced in making the BE components. The majority of Ti powder for the BE approach, however, has come from the sponge fines obtained from Kroll's magnesium reduction process.

In the second approach, blended elemental powders or powders obtained by hydriding and dehydriding of Ti sponge fines (HDH process) are generally used as the feedstock for manufacturing PM titanium components. In the HDH process, first, the hydriding of titanium sponge fines is performed to convert them into  $\text{TiH}_2$ . The  $\text{TiH}_2$  particles are brittle and they can be easily milled to the required particle size. The milled powders are then dehydrogenated to yield pure Ti powder (known as HDH titanium powder) of that size. Although a majority of conventional BE approaches have employed titanium sponge fines, the amount of impurity in the as-milled sponge fines is fairly high, which leads to a large amount of porosity in the final product, causing poor mechanical properties of the BE PM alloy. This is because significant chlorine impurity levels, often up to 1500 ppm, are present in the titanium sponge [29,30]. It is important to note that a large increase (up to 90% increase) in tensile elongation is achieved for PM Ti-6Al-4V alloy by using HDH powders with low oxygen and chlorine content [52,53]. Therefore, for superior mechanical properties, the use of HDH titanium powders as elemental titanium powder

feed stock in PM is quite attractive.

In the third approach, the titanium hydride powder has been directly used for making titanium alloy. The hydrogenated titanium powder, blended with the powder of desired alloy constituents, is cold pressed and sintered, followed by the removal of hydrogen by vacuum dehydrogenation [40,54–57]. In some recent studies [46], an additional processing step that involves transformation of the sintered  $\beta$ -Ti through the eutectoid temperature ( $\sim 800$  for Ti-6Al-4V-H system) is inserted to produce a very fine  $\alpha+\beta$  microstructure after dehydrogenation. In literature, this process is called the hydrogen-sintering-and-phase-transformation (HSPT) process. Studies relying on this processing route [45–48,58–61] indicated that a density  $>99\%$  and a very fine  $\alpha+\beta$  microstructure can be achieved in PM Ti-6Al-4V alloys. Therefore, there is a significant growth prospect for this approach in producing titanium components with high strength and ductility.

The conventional PM titanium processing involves a consolidation step in which titanium powders, mixed with desired alloy constituent powders, are compacted by cold-isostatic pressing (CIP) at room temperature to make the desired shapes. The compacts are then sintered at high temperature either in vacuum or in inert atmosphere (Figure 2.1) in the sintering step. This process (CIP + sinter) is suitable for producing low-cost titanium alloys for applications where dynamic mechanical properties such as fatigue resistance may not be critical. This is because the fatigue properties of the titanium component produced in this process are relatively inferior due to a significant amount of residual porosity. The porosity, however, can be reduced by applying thermo-mechanical treatments and this helps to significantly improve the fatigue properties [31,32]. Thus, the

sintering step is followed by the thermomechanical processing step and/or heat treatment step to reduce the residual porosity and refine the microstructure (Figure 2.1).

The alloyed powders produced by the pre-alloyed-rotating-electrode-process (PREP) method or by the gas atomization technique, although more expensive, are desired because of the homogeneity of alloy composition in the powders. In the PA method using these powders (Figure 2.1), the powders are generally hot compacted, usually using hot-isostatic-pressing (HIP), into the final shape in relatively very short time (~ 2 hrs). The properties of the as-HIPed PM titanium compact made from these powders can be further improved by optimizing the microstructure using the secondary processing steps such as thermo-mechanical processing and/or heat treatment. Alternatively, the pre-alloyed powders can also be cold pressed (CIP) and sintered to produce the titanium component. However, the mechanical properties of CIP+sinter compacts are generally inferior to that of HIPed equivalent due to large residual porosity [62]. It will be shown later that the tensile strength and ductility maps compiled in this review reveal the differences in properties between these two approaches.

### **2.3 Microstructure of PM Ti-6Al-4V Alloys**

The typical microstructures of PM Ti-6Al-4V alloys made using different PM approaches are shown in Figure 2.2. The microstructure of the alloy produced by conventional BE (CIP+sinter) PM approach consists of large colonies of lamellar  $\alpha$  plates and massive grain boundary  $\alpha$  (GB- $\alpha$ ) network with distributed porosity (Figure 2.2a). This particular specimen was sintered at 1573K (1300°C) and the reported relative density is 94%. A significant reduction in porosity was observed when the sintered

specimen was subjected to HIPing treatment, increasing the relative density to 99.4% (Figure 2.2b). Almost all the pores were eliminated by HIPing, and the microstructure morphology, although similar to that of the as-sintered specimen, exhibited some coarsening.

The microstructures obtained using pre-alloyed powders are shown in Figure 2.2(c&d). Figure 2.2c is the typical microstructure obtained in PA PM Ti-6Al-4V alloy after the HIPing of the powders at 1188K (915°C). The microstructure consists of large colonies of lamellar  $\alpha$  plates with almost no porosity in the microstructure (relative density > 99%). The average size of the  $\alpha$  plates or lamellar colonies in the microstructure of the as-HIPed specimen is an important variable affecting the mechanical properties. These sizes generally are affected by (a) type of feedstock powder (GA or PREP), and (b) the HIPing temperature and time [63]. The microstructure of PA PM titanium alloy that was hot-forged (at 1223K (950°C)) and heat treated (at 1233K (960°C) for 1 hr., then water quenched, followed by annealing at 973K (700°C) for 2 hr.) after the HIPing of PREP powders, is shown in Figure 2.2d. The microstructure shows a fine transformed  $\alpha+\beta$  microstructure with nearly globular primary alpha ( $\alpha$ ) phase.

A variety of microstructures in PA PM alloys have been produced with additional thermo-mechanical processing [64,65] after the primary HIPing consolidation step. Thus, a significant variation in tensile properties of PA PM Ti-6Al-4V alloy has been obtained, which can be attributed to the variation in the microstructure cause by the thermo-mechanical and/or heat treatment processing.

Figure 2.2(e) shows the microstructure of vacuum-sintered PM Ti-6Al-4V alloy, made using the BE method with  $\text{TiH}_2$  powders as the feedstock. A lamellar colony



microstructure with elongated  $\alpha$  plates can be seen, which is very similar to that of the conventional BE alloy made from elemental powders. However, the amount of residual porosity in the hydride-powder-based process is significantly lower compared to that in the conventional BE approach. The microstructure obtained by heat treating the vacuum-sintered specimen, made using  $\text{TiH}_2$  powder, is also shown in Figure 2.2f. It can be seen that heat treatment does not change the microstructure noticeably, because the lamellar structure, already coarsened and equilibrated in the vacuum sintering step, does not possess sufficient driving force to coarse the microstructure or recrystallize into the  $\alpha+\beta$  microstructure.

A high density and a refined microstructure of PM Ti-6Al-4V alloy can be obtained by the HSPT processing approach as shown in Figure 2.2g. The microstructure consists of very fine  $\alpha$  grains and discontinuous  $\beta$  phase (forming a very fine  $\alpha+\beta$  microstructure) inside the grains. The prior  $\beta$  grains in this microstructure have a relatively much thinner GB- $\alpha$  phase, unlike the vacuum-sintered microstructures. The refinement of the  $\alpha+\beta$  microstructure in the HSPT process is attributed to the eutectoid transformation ( $\beta\text{-Ti(H)} \rightarrow \beta\text{-Ti(H)} + \delta\text{-TiH}_x$ ) step and this is discussed elsewhere [45]. It is to be noted that the amount of residual porosity in the HSPT microstructure depends on the size of the initial  $\text{TiH}_2$  powder used [48, 59]. Due to high density and refined microstructure, the HSPT-processed PM Ti-6Al-4V alloy achieved tensile strengths higher than, and ductility levels equivalent to, that of the wrought Ti-6Al-4V alloy. Tensile strength levels are generally  $> 1000$  MPa and ductility levels are  $> 10\%$ , with this type of microstructure. However, the HSPT process does result in a relatively low amount of residual porosity. This residual porosity can be eliminated by using additional thermo-mechanical treatments or HIPing.

The microstructure of HSPT processed compact that was subjected to pneumatic-isostatic-forging (PIF) specimen is shown in Figure 2.2h. In the PIF step, which is a variant of the HIPing process, the sample is rapidly heated to a temperature and pressure is applied to close the porosity. This process has eliminated the porosity in the microstructure completely. Reduction in the porosity, however, did not significantly improve the tensile properties anymore, but a significant increase in fatigue strength resulted [48].

## **2.4 Tensile Properties of PM Ti-6Al-4V Alloy**

### **2.4.1 Strength-Ductility Map of PM Ti-6Al-4V Alloy**

Presented in Figure 2.3 are the tensile strength ( $\sigma_{UTS}$ ) data and the ductility (% elongation) data in the form of strength-ductility maps for variously processed Ti-6Al-4V alloys. Most of the data available in literature for PM-processed Ti-6Al-4V alloy are included in this compilation. Specifically, the tensile results of PM Ti-6Al-4V alloy made by both the blended element (BE) and the pre-alloyed (PA) method [7,8,10,11,14,31–34,53,62–83] are compared with that of the wrought Ti-6Al-4V alloy [84–91] in Figure 2.3. The property map of the wrought Ti-6Al-4V alloy exhibits a narrow range of tensile strength, varying from ~850 MPa to ~1200 MPa, and the ductility varies in between 3% to 26%. These variations in wrought Ti-6Al-4V alloy can be attributed to the possible variations in composition (interstitial level, especially oxygen) and microstructure variations of the alloy. This is because the wrought alloy is usually free from defects and the microstructure, although generally refined and homogeneous, is sensitive to the process temperature and cooling rate. For example, the martensitic microstructure of Ti-

6Al-4V alloy, which forms due to high cooling rates, can lead to a very high tensile strength but will greatly reduce the tensile ductility [87]. It is known that a microstructure with lamellar  $\alpha$  plates increases the ductility at the expense of tensile strength[86]. The microstructure modifications due to heat treatment, which result in a change in the properties of the wrought Ti-6Al-4V alloy, do so through the changes the volume fraction, the shape and the size of phases (mainly the alpha phase) in microstructure. In addition, oxygen content is known to affect the tensile properties of titanium. An increase in oxygen content from 0.12 wt.% to 0.19 wt.% increased the tensile strength of Ti-6Al-4V from 856 MPa to 994 MPa, without causing a significant change in tensile ductility [91]. Also, the oxygen content in the wrought Ti-6Al-4V alloy is not supposed to exceed 0.2 wt.% according to ASTM Grade 5 specification. The oxygen content below 0.2 wt.% has almost an insignificant effect on the tensile ductility of the Ti-6Al-4V[91].

#### **2.4.2 Factors Affecting Strength-Ductility of Blended Element**

##### **PM Ti-6Al-4V Alloy**

Figure 2.3 reveals that, similar to the wrought Ti-6Al-4V alloy, the PM BE Ti-6Al-4V alloy shows a significant spread of the property domain in the map of tensile strength versus ductility, although this spread is not as wide as that of the wrought condition. In contrast to the wrought version, the tensile properties of PM Ti-6Al-4V are affected primarily by porosity and impurities, although some effect of microstructure is to be expected. The conventional PM-processed (identified as BE: CP+sinter; Figure 2.3) Ti-6Al-4V alloy shows relatively inferior tensile properties among all that have been made by various PM processes. The tensile strengths are near the lower bound value of the

wrought alloy. The tensile strength varies in a narrow range (750 MPa - 900 MPa), but a significant variation in the tensile elongation (ranged from 3% to 13%) is also observed (Figure 2.3). Because the BE PM titanium alloys are vacuum sintered generally, it can be said that the tensile properties of the BE Ti-6Al-4V alloy would be primarily affected by porosity.

#### 2.4.2.1 Effect of Density and Purity

Commonly, the as-sintered density of the BE Ti-6Al-4V alloy, made using Ti sponge fines, reached only about 95% of the theoretical density [14]. A maximum elongation of 6%, at this density level, was reported [14]. A high residual porosity leads to a rapid decrease in tensile ductility, although the tensile strength is much less affected. Further, as discussed in section 2.1, the presence of high impurity levels, especially the chloride content, limit the maximum density that can be achieved in BE PM Ti-6Al-4V alloys. The impurities volatilize during sintering and create pores with insoluble gas bubbles. Thus, it was possible to achieve a high relative density when low impurity (chloride content) HDH titanium powder [70] was used in BE PM processing. The increased density led to simultaneous increases in both the tensile strength and the ductility. This is probably the reason for the ductility level of 13% in conventional BE Ti-6Al-4V alloy (the right most point in the property map for BE: CP+Sinter in Figure 2.3), made using the HDH powder [70]. It can thus be concluded that the large variations in ductility in BE PM titanium alloys are due to the variations in porosity and/or chloride level.

#### 2.4.2.2 Effect of Post Sintering Treatment

Further improvements in the tensile properties of the BE Ti-6Al-4V alloy, to reach the property levels of the wrought alloy, were sought through processing methods that help to increase the density to nearly 100%. Over the years, various processes have been developed for achieving the density close to the theoretical density of the alloy. The use of postsintering consolidation techniques such as hot isostatic pressing (HIP) is mainly to close the residual pores and to get a density level  $> 99.8\%$ . The tensile property range of such high-density samples of BE Ti-6Al-4V alloy (identified as CP/CW+sinter+HIP in Figure 2.3) has significantly improved compared to that of BE:CP+Sinter alloys. This is evident from the shift of the center-of-gravity of the strength-ductility data domain of the former materials toward the right and toward the top, relative to that of the latter materials. The property range now falls well within the domain of wrought Ti-6Al-4V alloy, as illustrated in Figure 2.3.

Near-theoretical-density ( $> 99\%$ ) in BE Ti-6Al-4V alloy could also be achieved by cold working of the blended alloy powder while making the green compact [71], but before sintering. The increased contact area between the powder particles and the generation of dislocations and shear bands during the cold working have been suggested to cause enhanced diffusion during sintering, thus leading to high-density samples. The increasing of density this way, to  $> 99\%$ , resulted in the tensile strength of BE Ti-6Al-4V reaching about 1000 MPa and, more importantly, the tensile ductility reaching to about 18% [71] as shown by the right-most data point in this property map. Nevertheless, it is intriguing that the postsintering consolidation has not eliminated the significant variation of ductility. Although the BE:CP/CW+sinter+HIP alloys have relatively higher density

levels, the tensile strength levels do vary over a range (920 - 1069 MPa), with a wide range of tensile ductility (6-18%), as seen in Figure 2.3. This domain of strength-ductility map was constructed based on the data collected from literature for BE PM Ti-6Al-4V. It is not clear at present why the variability in ductility is not reduced after applying HIPing or postsintering treatments to the compacts made by BE method. This variability in ductility must be resolved before one can hope to make commercially viable BE PM Ti-6Al-4V alloys.

#### **2.4.3 Factors Affecting Strength-Ductility of PA PM Ti-6Al-4V Alloy**

In Figure 2.3, the strength-ductility property map pre-alloyed (PA) PM Ti-6Al-4V alloy is also given using the data from literature [63–65,67,74–83]. A wide range of tensile properties can be observed for PA Ti-6Al-4V alloy, as well. The properties of PA PM Ti-6Al-4V are rarely compared on the density basis, since this method for making PM Ti-6Al-4V is intended to achieve nearly 100% density. In one of the processing approaches, the PA Ti-6Al-4V powders are HIPed to ~100% density into the desired shape. Alternatively, the PA powders have been first cold pressed and then hot isostatic pressed (CHIP process) to 100% densification. The strength-ductility data map for as-HIPed and -CHIPed PA Ti-6Al-4V is identified with the caption PA: HIP in Figure 2.3. A surprising finding is that a much higher level of variability in both the tensile strength (700-1068 MPa) and ductility (7.5- 21%) is observed, contrary to the expectation of a narrower property domain, relative to the BE PM Ti-6Al-4V alloys.

It is not possible here to resolve the reasons for the high degree of property variability in the high-density PA:HIP materials, but further research should aim to understand the

sources of this variability. The data map for PA:HIP, however, overlaps with the property domain of wrought Ti-6Al-4V alloys. However, few samples with exceptionally low tensile strength and ductility have also been observed. A tensile strength level as low as 700 MPa has been reported for a PA PM Ti-6Al-4V alloy [80]. This low tensile strength, however, corresponds to the low density (97% - 98%) of this Ti-6Al-4V alloy. Thus, the low tensile strength may be explained on the basis of low density. This may be an anomaly for PA:HIP PM alloys because, in general, PA method after HIPing produces approximately 100% dense PM Ti-6Al-4V alloy component. In Figure 2.3, most of the data points for PA:HIP are located between the tensile strength values of 850 and 1068 MPa and ductility levels of 8 and 20%. Another anomaly is the 7.5% ductility data, which is for the hot-pressed alloy [72], which is supposedly a fully dense PM T-6Al-4V alloy. An important factor to be considered is whether a solid material, free from any flaws, results from such processing approaches. It is important to note that an achievement of ~100% density, either in HIPing or CHIPing or hot pressing, does not necessarily mean that the walls of the closed pores have been completely welded during these processes. Part of the property variations are also likely related to the microstructure differences arising from the differences in the processing parameters. Again, an in-depth investigation of this is warranted.

#### 2.4.3.1 The Role of Microstructure and Heat Treatment

For PA PM Ti-6Al-4V alloys in particular, considerable work has been done to obtain various microstructures by varying the processing parameters, e.g., the temperature and the pressure of HIPing and/or thermomechanical treatment. Hence, the narrower range of

strength-ductility property map, even after HIP consolidation, as shown in Figure 2.3, may be a behavior to be expected. However, the data available are too few to make such a generalization. Note that PA powders often exhibit a martensitic microstructure due to rapid cooling in the powder manufacturing process, e.g., PREP or gas atomization [79,92,93]. The martensite microstructure and its hardness are the reasons for the poor cold-pressability of PA powders. However, during the thermal exposure due to HIPing, the as-HIPed microstructure of PA Ti-6Al-4V alloy can undergo phase transformation from martensite ( $\alpha'$ ) to  $\alpha+\beta$ , giving rise to a typical microstructure that consists of  $\alpha$  lathes inside prior beta ( $\beta$ ) grains [94]. Further, the formation of equiaxed  $\alpha$  was found to be related to the local deformation of powder particles, which occurs at the particle-particle interface during the HIPing process. This can lead to recrystallization of  $\alpha$  grains. A higher strain energy stored in powders can result in a lower aspect ratio of alpha plate [95–97], which is preferred for attaining a higher level of ductility in the final alloy. Additionally, strain energy in the initial powder can be generally increased by deforming the powder before the final compaction [71,79,98–101].

It is important to note that secondary processing steps such as thermo-mechanical treatments and/or heat treatment do not seem to significantly shift the domain of the strength-ductility map of PA:HIP+HT materials relative to the PA:HIP materials, as shown in Figure 2.3. However, the interesting result is the reduction in the size of the strength-ductility domain after heat treatment in particular, and the large reduction in variability of ductility. However, the data points supporting this notion are relatively few. The lack of a considerable shift in the center-of-gravity of strength-ductility domain is probably due to the fact that nearly 100% theoretical density is already achieved in the



as-HIPed state of PA Ti-6Al-4V alloy. Any additional processing steps will have only a marginal effect on tensile strength and ductility combination, perhaps due to small changes in microstructure. It is, however, difficult to make a clear conclusion here because of the variations in the microstructure and processing parameters. Historically, secondary processing steps were used to enhance the fatigue properties of as-HIPed PA Ti-6Al-4V alloy. A review of fatigue performance of PM Ti-6Al-4V alloy is presented elsewhere [49].

To summarize in this section, on the basis of strength-ductility property maps presented here, it is evident that the PM Ti-6Al-4V alloy can achieve tensile properties similar to that of wrought Ti-6Al-4V alloy by eliminating the porosity and impurities, and modifying the microstructure. The spread of the data map for PM Ti-6Al-4V alloys can be nearly as large as the strength-ductility domain found in wrought materials. Since the strength-ductility property maps for each process heavily overlap with each other, it is evident that multiple variables are at work simultaneously and a more meaningful conclusion requires proper structuring of data by keeping some parameters constant in the course of comparisons. This will be done in the following sections.

## **2.5 The Specific Effects of Porosity on Tensile**

### **Properties of PM Ti-6Al-4V**

#### **2.5.1 Effect on Tensile Strength**

There are several publications in literature that report on the effect of porosity on the tensile strength of PM Ti-6Al-4V alloy. A reduction in the tensile strength caused by the increase in porosity is commonly observed [8,23,28,32]. Generally, the effects of powder

characteristics, sintering, and postsintering treatments on tensile strength are mainly reflected through the effects of porosity on strength. Figure 2.4 reveals the weak correlation of tensile strength with density. This plot was made by compiling the densities and tensile strength levels reported in several studies [7,8,14,18,32–34,53,63–73,76–83,102] for PM Ti-6Al-4V alloy compacts with lamellar microstructure. The data are for PM compacts made by either BE or PA method. The volume fractions of pores were not reported in these studies, but a lower relative density would mean a higher volume fraction of porosity in the microstructure.

In Figure 2.4, it is clear that the tensile strength increases from about 830 MPa to about 1075 MPa, when the relative density increased from 94% to >99% [7,8,14,18,32–34,53,63–73,76–83,102]. The presence of porosity reduces the effective load bearing cross-sectional area, leading to a decrease in strength because of the increased stress on the net section of the specimen during tensile loading [103,104]. It is possible that only a relatively small section of the tensile specimen actually plastically deforms in tension, due to the concentration of stress/deformation between the pores. The stress intensification in the sintered ligaments between the pores causes the ligaments to reach the tensile fracture stress earlier than the solid regions of the specimens, during tensile loading. This process can lead to the observation of a relatively high area fraction of porosity on the fracture surface, compared to the bulk area fraction of porosity observed on a metallographically polished surface. Bourcier et al. [105] indicated that the area fraction porosity on the fracture plane is about 8 to 10 times the porosity level in bulk. This supports the idea of stress concentration in the ligament section that is probably created by the formation of a fracture plane that connects as many pores as possible, yet

the plane being approximately normal to the stress axis. While this clearly leads to the decrease in strength in proportion to the porosity, the actual porosity controlling this behavior may be the volume fraction of porosity on the fracture plane.

### **2.5.2 Effect on Tensile Ductility**

The plot of tensile ductility of PM Ti-6Al-4V alloys as a function of the relative density, made using the compiled data, is presented in Figure 2.5. It is known that microstructure can affect the tensile ductility of the materials. In fact, the wide range of ductility, which is observed at a nearly constant strength level in Figure 2.3 for wrought alloys, is principally attributed to the variations in the microstructure of the Ti-6Al-4V alloy. Therefore, in the interpretations of the effect of porosity or density on tensile ductility of PM Ti-6Al-4V, the effects of microstructure should be decoupled to reveal the true effect of porosity on ductility. This necessitates that the porosity-ductility correlation be examined under constant microstructure conditions for any meaningful conclusions. For this purpose, the data in Figure 2.5, have been restricted to lamellar microstructures of PM Ti-6Al-4V, for which the relative density ranged from ~94% to ~100% [7,8,14,18,32–34,53,63–73,76–83,102]. The data for PM Ti-6Al-4V alloys made by both the BE and PA methods, but restricted to lamellar microstructure, are included in the figure.

It can be seen in Figure 2.5 that the ductility increased from ~ 5% to ~ 25% when the relative density increased from 94% to 100%, which is a much stronger effect than that found between tensile strength and relative density. The presence of porosity causes, first, strain concentration in the vicinity of pores and, secondly, limits the uniform deformation

of gage section, both leading to the reduction in the macroscopic ductility. Cope [106] considered the ligaments between the pores in the sintered specimen as the individual miniature tensile specimens. He showed that during tensile loading, most of the deformation occurs within the narrower parts of the ligament. Most of the strain localization occurred at the shortest distance between the pores, causing localized and inhomogeneous deformation. The inhomogeneous deformation causes material to fracture at a relatively lower applied tensile stress, thus limiting the extent of uniform macroscopic elongation before fracture

An intriguing result that emerges from Figure 2.4 and Figure 2.5 is that, although the tensile strength does not vary much, a large variation in the ductility is observed in the PM materials with the highest density (>99% relative density) level (Figure 2.5). At this density level, the ductility varies from 10%-20%, which is quite surprising. Normally, one would expect the ductility level to be high and much less varied from specimen to specimen, because the porosity is largely eliminated at such high density levels. Such a variation in the well-consolidated or sintered PM materials is unexpected and is not possible to explain on the basis of the diminutive amount of porosity present in highly dense samples. However, this result is consistent with a study on a cast alloy [107] which showed that a large variation in ductility is possible even in a material that is supposedly highly dense. In their study of a cast Al alloy (relative density > 99.9%), Surappa et al. [107] reported that the tensile ductility varied from ~ 2% to ~ 15%. Based on fractography, the authors correlated the decrease in ductility from ~ 15% to ~ 2% to the increase in the size of a crack-initiating pore, from ~ 1 mm to ~ 3 mm, as observed on tensile fracture surfaces. This large variation in ductility was attributed to the strain

concentration in the vicinity of a single large pore which was found on the fracture surface. Chawla et al. [104] also showed (using finite element modeling) that large amounts of strain intensification can occur at a single large pore or an equivalent configuration created by a pore cluster. The strain localization that occurs around a large pore leads to early crack initiation during the tensile loading.

The large variation in ductility in Figure 2.5 at the highest achieved densities of PM Ti-6Al-4V can be explained on the basis of the extreme-sized pores in the tensile specimens. In our recent study [59,108], it was shown that a large variation in ductility of highly dense (>99%) PM Ti-6Al-4V alloys can occur due to the presence of extreme-sized pores. Figure 2.6 illustrates the variation in tensile ductility, as a function of the largest pore size that was found on the fracture surface, in PM Ti-6Al-4V alloy containing about 0.4 wt.% oxygen. The alloy was made from titanium hydride powders using the HSPT BE approach. In the sintered samples of this material, it was found that, due to process-induced effects, large pores randomly occur, even at a very low volume fraction of bulk porosity (<0.1%). In this scenario, each tensile sample will have a different extreme-sized pore in its volume, based on the statistical chance of occurrence. Thus, the variability in the elongation in the high-density PM Ti-6Al-4V alloy can be attributed to statistics of occurrence of the largest pore in the tensile samples. The extreme-sized pores in PM Ti-6Al-4V alloy can limit the extent of uniform elongation that can be attained before the fracture initiated from the pore. It has been shown [59,108] that the extreme-sized pores in the test volume initiate tensile fracture due to strain concentration next to the pores. The strain concentration next to the pore arises from the localization of plastic deformation caused by the increased net section stress as well as

the stress concentration due to the pore itself. Consequently, at any applied stress, the plastic strain in the deformation-localized region is larger than the plastic strain in the uniform gage section. In one extreme case, a pore having a cross-sectional area of about 50% of solid specimen localized plastic deformation severely, to the point of fracture strain, even though the uniform gage section was nominally elastic and showed no evidence of plastic deformation.

### **2.5.3 Strength-Ductility Maps at Constant Microstructure**

In addition to the porosity, the microstructure of the alloy has a significant effect on the tensile properties of PM Ti-6Al-4V alloy. In Table 2.1, a compilation of tensile properties of PM Ti-6Al-4V alloy with lamellar microstructure at various density levels is presented. The data included in the Table are only a sample of the dataset that was used to make Figure 2.7. In this dataset, the reported tensile strength values vary in the range of ~ 750 MPa to ~ 1200 MPa, while ductility varies from ~ 5% to ~ 20%. The strength-ductility maps of tensile properties of PM Ti-6Al-4V alloy with a constant microstructure, when compared on the basis of nearly constant density, help to isolate the shifts in property ranges, as caused by density alone. Such maps for three density levels have been compiled and are presented in Figure 2.7. The PM Ti-6Al-4V alloys having densities in the range 94%-95% have a poor combination of tensile strength and ductility. Increasing the density (to 97%-98%) resulted in a large increase in tensile ductility, and causes the properties domain to shift towards the right, with little change in tensile strength. When the densities increased to more than 99%, a further large increase in ductility, with one sample having 20% elongation at a tensile strength of about 1000 MPa, is found. It is

noted that this may be the best combination of tensile strength and ductility that was ever achieved in a PM product, especially with the lamellar microstructure. Thus, for a given microstructure, a high level of strength-ductility combination can be achieved by focusing on increasing the density as much as possible during the powder metallurgical processing of Ti-6Al-4V alloy.

## 2.6 Microstructure Factors Affecting Tensile Properties

The true effect of microstructure on the relative placement of the property domains in strength-ductility maps for PM Ti-6Al-4V alloys can only be assessed on the basis of largely pore-free microstructures. For this purpose, the tensile properties of the high-density (> 99% relative density) PM Ti-6Al-4V alloys reported in the literature have been grouped here into three common microstructure classes: lamellar, equiaxed, and fine-widmanstätten microstructure. The grouped data are presented as strength-ductility maps in Figure 2.8 [7,8,14,18,32–34,53,63–73,76–83,102]. The data included in this figure come from a large number of sources, and only a sample of the property data that were used in Figure 2.8 is given in Table 2.2. From the behavior of wrought Ti-6Al-4V alloys, it is generally known that the lamellar microstructure provides limited barriers to dislocation motion and deformation during tensile straining is inhomogeneous. This deformation behavior leads to a relatively low strength and ductility combination. The equiaxed  $\alpha$  microstructure tends to show relatively higher values of strength and ductility in general, because of an increased number of barriers to dislocation motion and a relatively more homogenous deformation due to the fine, equiaxed nature of alpha phase. For example, Lee et al. [33] reported the tensile properties of equiaxed and lamellar

microstructure PM Ti-6Al-4V alloys that had nearly the same density. A significantly higher ductility (11% El.) was observed for the equiaxed microstructure compared to the lamellar microstructure (7.5% El.). The strength of the lamellar microstructure (1090 MPa) was comparable to that of the equiaxed microstructure (1050 MPa).

The most significant observation that emerges from the strength-ductility maps in Figure 2.8 is that the largest variation in tensile properties, both in strength and ductility, is seen in the lamellar microstructure group. There are a number of microstructure factors that can cause this variation—the size of the lamellar colony, the size of prior  $\beta$  grains, and the size of grain boundary  $\alpha$  (GB $\alpha$ ). Lutjering et al. [109,110] showed that the tensile strength of ( $\alpha$ + $\beta$ ) alloy depends moderately on  $\alpha$  colony size—the strength increased slightly with a decrease in the colony size. Additionally, the average size of prior- $\beta$  grains has a significant influence on the tensile properties. Studies indicate that a decrease in the prior- $\beta$  grain size led to an increase in both the tensile strength [84,109–115] and the ductility of the alloy [109,113]. A significant increase in the elongation (from 6% to 12%) was observed when the prior  $\beta$  grain size was reduced from 600  $\mu\text{m}$  to 100  $\mu\text{m}$  [109]. The increase in the % elongation in a polycrystal is related to the mean-free distance for slip, which is smaller for the smaller  $\beta$  grains. The shorter dislocation pile-up length, due to the smaller prior beta grains, helps to reduce the stress concentration at the grain boundary, thus delaying the crack initiation during tensile deformation. This is reflected as an increase in the ductility of the microstructure. The size and the shape of  $\alpha$  lamellae are also known to affect the tensile strength and the ductility of Ti-6Al-4V alloy. A lower aspect ratio of  $\alpha$  lamellae exhibits a relatively high ductility—the tips of the large-aspect-ratio  $\alpha$  plates in the lamellae act as stress concentration sites, leading to the reduction in



ductility [96]. Which of these microstructural factors becomes a dominant factor that would dictate the tensile performance, depends on the powder parameters, the processing approach, and the postsintering processes such as thermomechanical processing and heat treatment.

It is quite surprising that the PM Ti-6Al-4V alloys with an equiaxed alpha microstructure also exhibit a wide range of properties on the strength-ductility map, as shown in Figure 2.8. This variation is as much as that observed for the lamellar microstructure. The tensile strength is found to vary between 700 to 1130 MPa in the literature while ductility varies in the range of  $\sim 6$  to  $\sim 20\%$ . Unlike the lamellar structure, the tensile properties of an equiaxed structure largely depend of the size of the  $\alpha$  phase. It was shown that microstructures with a finer and equiaxed  $\alpha$  exhibited a relatively high tensile strength and a relatively lower ductility [63]. This may be the reason that, in Figure 2.8, the strength data are concentrated in the upper part of the data domain, with the exception of a few data points. The ductility spread is as much as that seen for lamellar microstructures. While this may be difficult to explain, it is not unreasonable to suppose that extreme pores are involved in controlling the ductility here, as discussed in section 2.5.2. According to the studies [116,117], the phenomenon of increased strength is due to the shorter mean-free path for dislocation motion. The increased ductility is due to the difficulty associated with the nucleation and growth of the voids during the tensile deformation. It was noted that most of the voids in  $(\alpha+\beta)$  Ti alloy nucleate at the interface between alpha ( $\alpha$ ) and beta ( $\beta$ ) phase, hence the alpha-beta phase morphology, in addition to extreme-sized pores, may also play a complicating role. It is not possible to isolate the individual variable affecting strength or ductility because of the possible compounding

effects of many microstructural parameters and extreme pores.

The strength levels achieved in PM Ti-6Al-4V alloys with widmanstätten microstructures are significant, as can be seen in the upward shifting of strength-ductility property domain in Figure 2.8. This is again attributable to the refined nature of widmanstätten microstructures with a much smaller dislocation mean-free-path during plastic deformation. The very fine elongated  $\alpha$  phase in such a microstructure acts as a potent barrier for the dislocation motion during deformation, leading to a very high strength. As a result, widmanstätten microstructures show relatively higher strength levels compared to other microstructures, yet with nearly as much variation in ductility as that seen in equiaxed and lamellar microstructures. The extents of ductility domains for all the microstructures are largely similar, which may be due to complex microstructure effects that are discussed before. The specific examples of strength and ductility levels for specific microstructures from selected studies are compiled in Table 2.2.

## **2.7 Effect of Manufacturing Process on the Tensile Properties**

The most common approach to manufacture PM Ti-6Al-4V alloy is through the use of elemental powders, despite the fact that the BE method, in general, shows relatively poor tensile properties (Figure 2.9 and Table 2.3). This was discussed in section 2.2 and was attributed to low density and high impurity levels. Additional processing steps, such as mechanical working and/or heat treatment, can significantly improve (Table 2.3) the tensile properties of BE Ti-6Al-4V alloy, but this comes with increased processing cost. Recently, the use of titanium hydride ( $\text{TiH}_2$ ) powder in the place of Ti powder in the BE method has been shown to be effective in producing a relatively high-density material.

For example, a 98.5% density was achieved for CP titanium when  $\text{TiH}_2$  was used as starting powder, in contrast to the 95% density achieved when Ti powder was used in vacuum sintering under similar processing conditions [118].

The benefits arising from using the titanium hydride powder and vacuum sintering (with dehydrogenation) to obtain PM Ti-6Al-4V compacts have been well documented in the literature. Studies [40,42,57,119] showed that a relatively high concentration of vacancies and dislocations are generated due to the change in volume and shearing during the decomposition of the hydride phase, which can lead to an increase in the rate of diffusion, which helps in PM consolidation. Also, titanium hydride powders fragment during compaction due to their brittleness, resulting in finer particles and producing additional new surfaces for sintering [40,57,120]. In addition, the atomic hydrogen released from hydride powder has been suggested to clean the particle surface, thus increasing the chemical activity of the titanium surface [120,121], which could help the sintering process. Further, the lower oxygen content in the hydride powder is an additional benefit resulting from the use of the hydride powder. It was found that PM Ti-6Al-4V alloys with a remarkably low oxygen content and high density after vacuum sintering can be obtained.

The tensile property domains of BE PM Ti-6Al-4V alloys made by vacuum sintering (conventional Ti powder) and those made by the new HSPT process (see discussion later for more details) are compared in the strength-ductility map in Figure 2.9. The range of tensile strength and ductility domain for BE PM Ti-6Al-4V alloy made by vacuum dehydrogenation sintering of  $\text{TiH}_2$  powder is also presented in the strength-ductility map in Figure 2.9. The typical tensile properties of BE PM Ti-6Al-4V alloys made by the

vacuum sintering of  $\text{TiH}_2$  powder provide a tensile strength range of 950 MPa-1050 MPa and a ductility range of 8%-13% [40,42,55–57,118,122]. This domain for BE:Ti-Hydride is shifted to the top relative to the BE: conventional, indicating that improved tensile strength levels of PM Ti-6Al-4V alloy can be achieved still using the BE and vacuum sintering approach, but employing the  $\text{TiH}_2$  powder. Optimizing the variables such as initial powder size, compaction pressure, sintering temperature and time, the tensile strength can be further improved [120,123] in  $\text{TiH}_2$  approach. When additional mechanical processing is implemented on the conventional BE Ti powder approach (BE: Conventional + MW/HT) and the  $\text{TiH}_2$  powder-based approach (BE: Ti-Hydride + MW/HT), there are clearly significant increases in the strength-ductility combination of the alloy. Two aspects are to be noted here. First, it can be seen that hydride-based BE PM Ti-6Al-4V alloys can provide a strength-ductility property range that is comparable to that obtained by the mechanical working/heat treatment of conventional BE compacts. Secondly, it can be seen in Figure 2.9 that the use of MW/HT leads to a much larger improvement in the mechanical properties of PM articles made with  $\text{TiH}_2$  powder. A tensile strength level as large as ~ 1200 MPa and a ductility level of ~ 20% were achieved for BE Ti-6Al-4V alloy made by  $\text{TiH}_2$  approach followed by additional mechanical working steps [122]. This is probably the highest strength and ductility combination that was ever achieved in PM Ti-6Al-4V alloys.

The use of a vacuum-sintering approach in consolidating BE powders with  $\text{TiH}_2$  as the starting material still results in a relatively coarse microstructure. This presents an inherent limitation to the range of tensile properties that can be obtained in general through a BE approach, even with the use of  $\text{TiH}_2$  powder. It is known [124,125] that

eutectoid phase transformation of hydrogenated titanium alloys refines and modifies the microstructure of the titanium alloys. Based on this, and following some steps of the BE route using the titanium hydride powder, a new process was recently introduced using  $\text{TiH}_2$  as the starting powder, with a view to obtaining the most refined microstructure in PM Ti-6Al-4V alloy. This method uses hydrogen sintering in the  $\beta\text{-Ti(H)}$  phase field instead of the common vacuum-sintering process. The hypothesis is that the presence of hydrogen in solid solution in beta-titanium reduces the activation energy of Ti self-diffusion by decreasing the Ti-Ti bonding strength [126], which could lead to an increase in the densification rate. After hydrogen sintering, the densified samples are cooled to a temperature below the eutectoid transformation temperature for the eutectoid phase transformation to occur. During this process,  $\beta\text{-Ti(H)}$  transformed into  $\alpha\text{(H)}+\beta\text{(H)}$  plus a hydride phase ( $\beta\text{-Ti(H)} \rightarrow \alpha\text{-Ti(H)} + \beta\text{-Ti(H)} + \delta\text{-TiH}_x$ ) and broke the interiors of coarse  $\beta$  grains into fine microstructure, setting the stage for an extremely refined  $\alpha+\beta$  microstructure [46,47]. The hydrogen is then removed by dehydrogenation around 973K (700°C), to a level lower than that is allowed in the ASTM standard (150 ppm H max; ASTM standard B348-10) for wrought titanium alloys. The entire process is referred to as the “hydrogen sintering and phase transformation (HSPT)” process [46]. It was shown that this method is able to produce densities of final alloy close to the theoretical density (> 99%). Also, the oxygen content is generally low in these compacts due to the scavenging action of hydrogen during dehydrogenation.

The strength-ductility map of BE Ti-6Al-4V alloy processed using HSPT (BE: HSPT) is also included in Figure 2.9, along with the data from the conventional BE PM processes discussed above. An excellent combination of strength and ductility in the BE

Ti-6Al-4V alloy can be achieved using the HSPT process. For example, a high tensile strength (1100 MPa) is achieved with a reasonably high elongation ( $\sim 13\%$ ). These improvements in tensile properties were attributed to a very fine and uniform  $\alpha+\beta$  microstructure resulting from the eutectoid transformation step in the HSPT process [45]. The effect of the subsequent MW/HT step on the mechanical properties of HSPT-processed Ti-6Al-4V alloy has been recently investigated [61]. As shown in Figure 2.9, the domain of BE: HSPT+MW/HT[61,127] overlap with the BE: HSPT, which suggests that additional mechanical working and heat treatment of HSPT-processed material has limited or no effect on the tensile properties' combinations. Although some improvement in strength-ductility combination appears to arise [61] after MW/HT of HSPT alloys, the improvement is not as great as that found in other BE approaches.

## 2.8 Summary

Based on the critical analysis of tensile properties of PM Ti-6Al-4V alloys compiled in the form of strength-ductility maps, the following conclusions can be drawn.

1. The principal variable that affects the tensile properties of PM Ti-6Al-4V alloy is the porosity. A relative density  $> 98\%$  is required to achieve tensile properties comparable to that of wrought Ti-6Al-4V alloys.
2. The tensile strength of PM Ti-6Al-4V alloy is only mildly affected by porosity, on the basis of the evaluation of properties of materials with relative densities between 95% and  $>99\%$ . This is explainable on the basis of small variations in net load-bearing area, due to the small changes in porosity.
3. At a nearly constant relative density, a large variation in ductility was seen,

regardless of the microstructure. This is believed to be due to the effect of pores, possibly extreme-sized pores, in causing strain concentration and early crack initiation, thereby limiting the achievement of uniform elongation in tension.

4. A surprising finding is that the variability in ductility is actually the highest at the highest possible densities of PM Ti-6Al-4V alloy, when assessed on the basis of constant lamellar microstructure. This may be due to extreme-sized pores that occur statistically randomly in specimens, regardless of the microstructure condition.

5. The evidence also suggests that although the best tensile properties in PM Ti-6Al-4V alloy can be achieved with very fine widmanstätten microstructure, the same degree of variability of ductility, as found in other microstructures, persisted.

6. Mechanical working and/or heat treatment consistently improved the strength-ductility combination of all PM Ti-6Al-4V alloys, regardless of the process by which they were made. This is clearly due to the elimination of porosity or closing of pores and the refinement of microstructure.

7. The PM Ti-6Al-4V alloy made by the relatively new “HSPT process” is able to produce PM Ti-6Al-4V alloy with a tensile strength level ~ 1100 MPa and ductility ~ 18%, due to an extremely fine  $\alpha+\beta$  microstructure. This process is a promising approach for potentially lowering the cost of manufacturing while maintaining the PM tensile properties close to those of the wrought Ti-6Al-4V alloy.

## **2.9 Acknowledgement**

The authors thankfully acknowledge the financial support from the US Department of Energy, Innovative Manufacturing Initiative (DEEE0005761), through the Advanced Manufacturing Office and the Office of Energy Efficiency and Renewable Energy.



Table 2.1. Room-temperature tensile properties of lamellar PM Ti-6Al-4V alloy at various density levels

Density(%)	Processing	Density(%)	$\sigma_{YS}$ (MPa)	$\sigma_{UTS}$ (MPa)	(% EL.)
<b>(94-96%)</b>	CIP+VS, BE[7]	94	740	830	6
	CP+VS, BE[32]	95	750	810	5
	CP+VS,BA[14]	94.8	683	773	6
	P+ VS, PA,[56]	95	838	937	4
	PIM, PA, [108]	94.8	645	720	4.5
	CIP+VS,BA [15]	96	850	965	10
<b>(96-98%)</b>	Tiara, BE,[16]	97.5	804	912	8
	CP+VS,BE[14]	97	820	880	10
	MIM, PA[109]	97.1	728	832	13.4
	CIP+VS, BA[110]	96.5	815	919	7.1
	Tiara, BE[64]	97.7	833	954	12
	MIM, PA[109]	97.5	748	835	9.2
<b>(&gt; 99%)</b>	HP, PA[77]	99.09	800	950	13
	CP+HP, PA[77]	98.46	740	830	14
	CIP+VS+HIP, BE[66]	~100	864	965	13
	CP+VS+HIP, BE[65]	~100	833	921	14
	HIP, PA[70]	~100	967.3	900	14.5
	CIP+VS+HIP, BE[8]	99.4	827	896	15
	HIP, PA[58]	~100	875	995	16
	HIP, PA[96]	~100	860	937	17
	HIP, PA[75]	~100	931	998	11
	HIP, PA[76]	~100	841	910	18
	HIP, PA[63]	~100	821	910	15
	CIP+VS, BE[103]	99	850	970	12.5
	P+ VS, PA[56]	99	848	925	6.2
	MR-9+TM+HT, BE[33]	99.2	1090	1185	7.5

BE: blended element powder processing, CP: cold press, CIP: cold isostatic pressing, VS: Vacuum sintering, PIM: powder injection molding, MIM: metal injection molding, HP: hot pressing, MR-9: patented BE powder processing, HIP: hot isostatic pressing, HT: heat treatment, TM: thermomechanical treatment, TIARA: patented BE powder processing, PA: pre-alloyed powder processing.

Table 2.2. Room-temperature tensile properties of lamellar PM Ti-6Al-4V alloy at specific microstructure conditions

Micro-structure	Processing	Density (%)	$\sigma_{YS}$ (MPa)	$\sigma_{UTS}$ (MPa)	(% El.)
<b>Lamellar</b>	HP, PA[77]	99.09	800	950	13
	P+ VS, PA[56]	99	848	925	6.2
	CIP+VS+HIP, BE[66]	~100	864	965	13
	CP+VS+HIP, BE[65]	~100	833	921	14
	HIP, PA[70]	~100	967.3	900	14.5
	CIP+VS+HIP, BE[8]	99.4	827	896	15
	CIP+VS, BE[103]	99	850	970	12.5
<b>Equiaxed</b>	HIP, PA[73]	99.23	932	980	14.8
	MR-9, BE[61]	99	825	915	10
	HIP, PA[63]	100	862	951	15
	HIP, PA[79]	>99	880	962	10.47
	CP+VS+HT+CR+HIP, BE[65]	>99	911	990	16
	HSPT+HT[60]	>99	881	952	19.2
	HIP+MW+HT, PA[70]	100	931.4	1047.6	16.7
	HIP, PA[73]	99.71	845	930	18.5
	ROC+RA, PA[95]	>99	827	869	16
<b>Widman-stätten</b>	HIP+HT, PA[58]	100	1000	1105	14
	HIP+HVC, PA[76]	100	931	993	15
	CIP+VS+HIP+HDH, BE[34]	99.9	834	938	13
	CP+VS+HT+HIP, BE[65]	100	862	951	15
	HSPT[46]	>99	930	994	17.8
	HIP+HT, PA[70]	100	931.9	1036.3	13
	HIP+MW+HT, PA[70]	100	989.8	1087.8	12.7
	HIP, PA[80]	100	860	937	17
	CIP+VS+HIP+BUS, BE[83]	99.9	951	1034	7
	CIP+VS+HIP+HDH, BE[83]	99.9	834	938	13

BE: blended element powder processing, CP: cold press, CIP: cold isostatic pressing, VS: Vacuum sintering, ROC: rapid omnidirectional compaction, RA: recrystallization annealing, HW: hot working, HP: hot pressing, MR-9: patented BE powder processing, HIP: hot isostatic pressing, HT: heat treatment, TM: thermomechanical treatment, TIARA: patented BE powder processing, PA: pre-alloyed powder processing, HSPT: hydrogen sintering and phase transformation.

Table 2.3. Room-temperature tensile properties of lamellar PM Ti-6Al-4V alloy made from different initial powders

Base powder	Processing	Density (%)	Micro-structure	$\sigma_{YS}$ (MPa)	$\sigma_{UTS}$ (MPa)	(%El.)
Ti	CIP+VS[7]	94	Lamellar	740	830	6
	CP+VS[32]	94	Lamellar	737	827	5
	CP+VS[32]	95	Lamellar	750	810	5
	CIP+VS[32]	97	Lamellar	820	880	10
	CP+VS[14]	94.8	Lamellar	683	773	6
	CP+VS[32]	98	Lamellar	850	920	13
	CIP+VS+HIP+HDH[34]	99.9	Fine <i>widmanstätten</i>	834	938	13
	CIP+VS+HT+C R+HIP [65]	> 99	Equiaxed	911	990	16
TiH <sub>2</sub>	CP+VS[127]	96	Lamellar	850	965	10
	CIP+VS[46]	-	Lamellar	859	982	12
	CIP+VS[94]	99	Lamellar	850	970	12.5
	CP+ VS[40]	98.3	Lamellar	960	1040	5.7
	CIP+VS+HR [127]	> 99	Fine <i>widmanstätten</i>	1054	1180	20
	CIP+VS+HR+ HT [127]	> 99	lamellar	1100	1180	17
	HSPT[46]	99	Fine <i>widmanstätten</i>	943	1036	15
	HSPT[59]	98	Fine <i>widmanstätten</i>	961	1027	13.7
	HSPT[48]	98.5	Fine <i>widmanstätten</i>	955	1033	13.7
	HSPT[48]	99.2	Fine <i>widmanstätten</i>	946	1032	15.6
	HSPT+HT [60]	99	globularized $\alpha$	881	952	19.2
	HSPT+HIP [48]	99.9	Fine <i>widmanstätten</i>	952	1023	18.2
	HSPT[107]	99	Fine <i>widmanstätten</i>	1016	1102	12.3

CP: cold press, CIP: cold isostatic pressing, VS: Vacuum sintering, HIP: hot isostatic pressing, HT: heat treatment, HR: hot rolling, HSPT: hydrogen sintering and phase transformation.

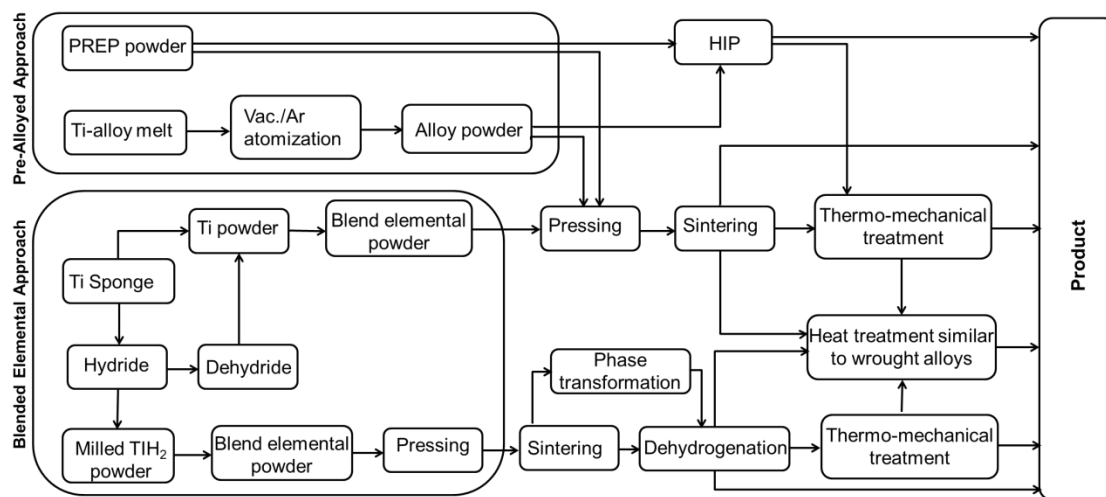


Figure 2.1 Flow sheet of titanium powder metallurgy (PM) processing

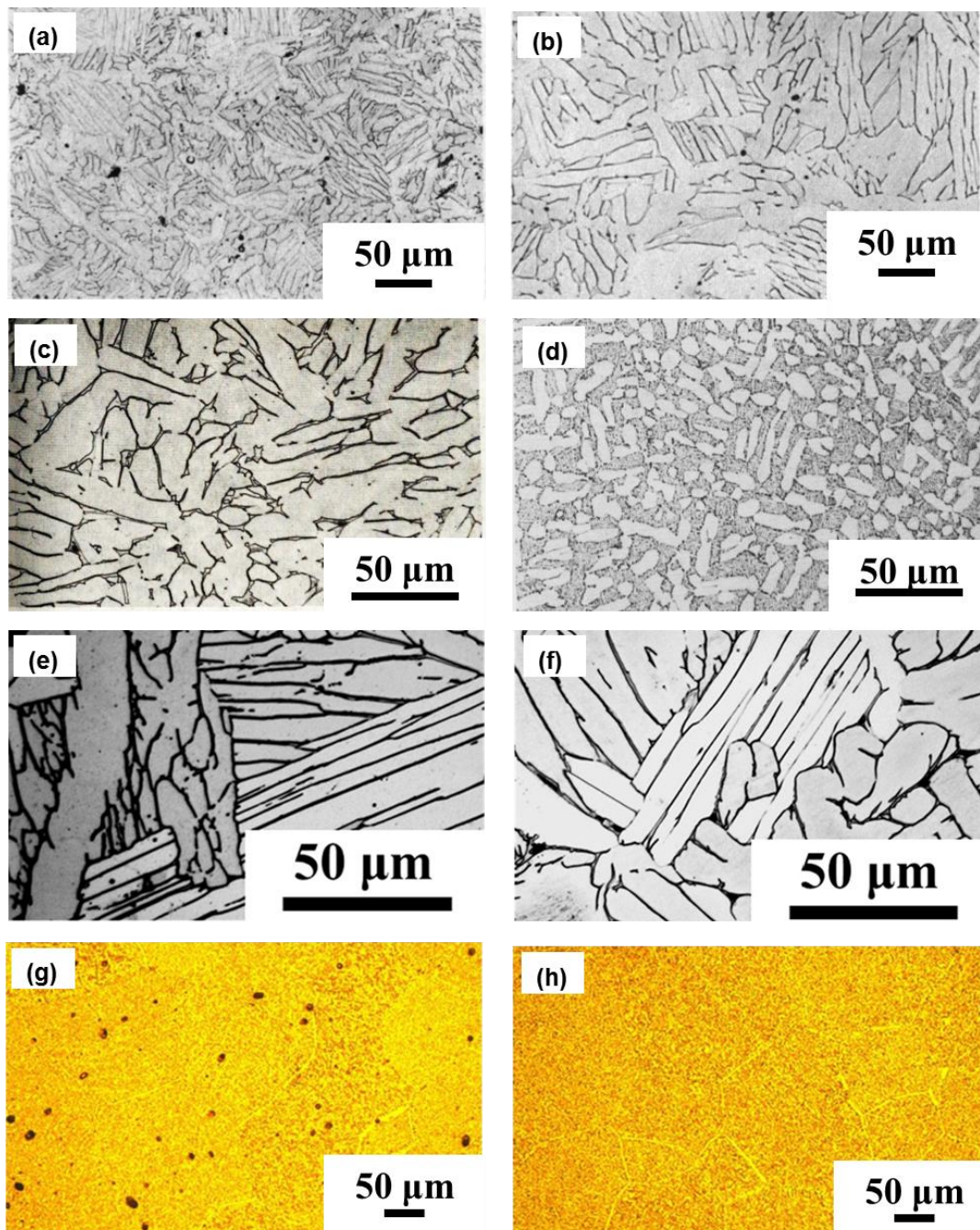


Figure 2.2. Typical microstructures of PM Ti-6Al-4V alloys prepared by (a) BE compact after vacuum sintering [7] (b) BE compact after vacuum sintering and thermomechanical treatment [7] (c) PA compact after HIPing [64] (d) PA compact after HIPing and thermomechanical treatment [64] (e) vacuum sintering of compacts of titanium hydride powder [61] (f) vacuum sintering and heat treatment of compacts of titanium hydride powder [61] (g) HSPT process [48] (h) HSPT process followed by PIF treatment [48]

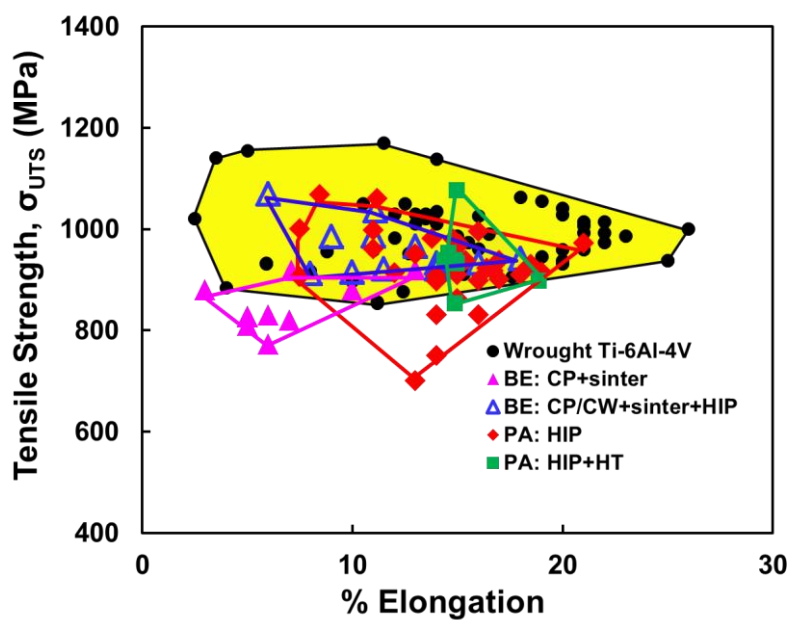


Figure 2.3. Tensile strength versus % elongation of Ti-6Al-4V alloy produced by different route [7,8,10,11,14,31–34,53,62–91]

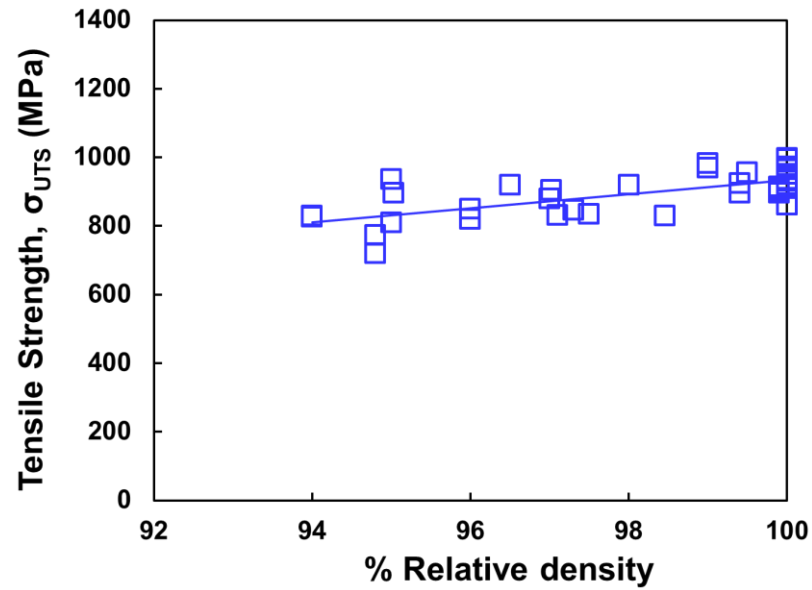


Figure 2.4. Tensile strength versus % relative density of lamellar Ti-6Al-4V alloy produced by BE and PA method [7,8,14,18,32–34,53,63–73,76–83,102]

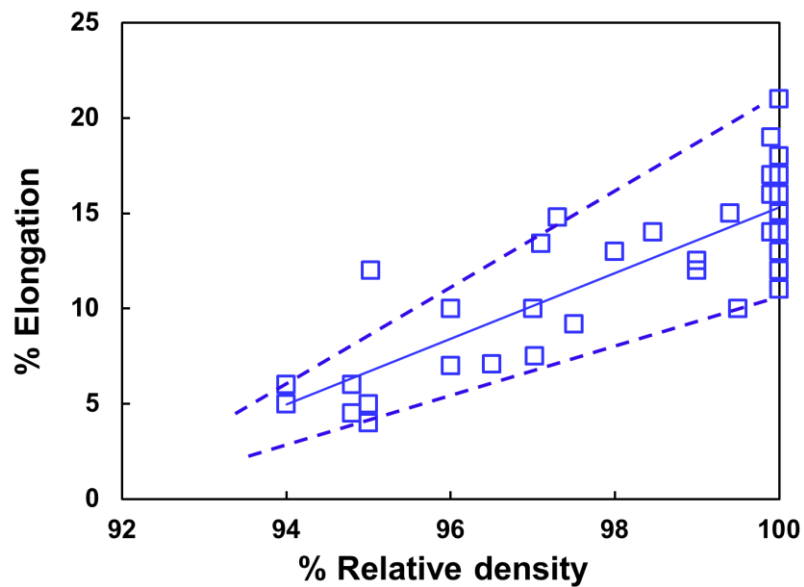


Figure 2.5. % Elongation versus % relative density of lamellar microstructures of PM Ti-6Al-4V alloy produced by BE and PA method [7,8,14,18,32–34,53,63–73,76–83,102]

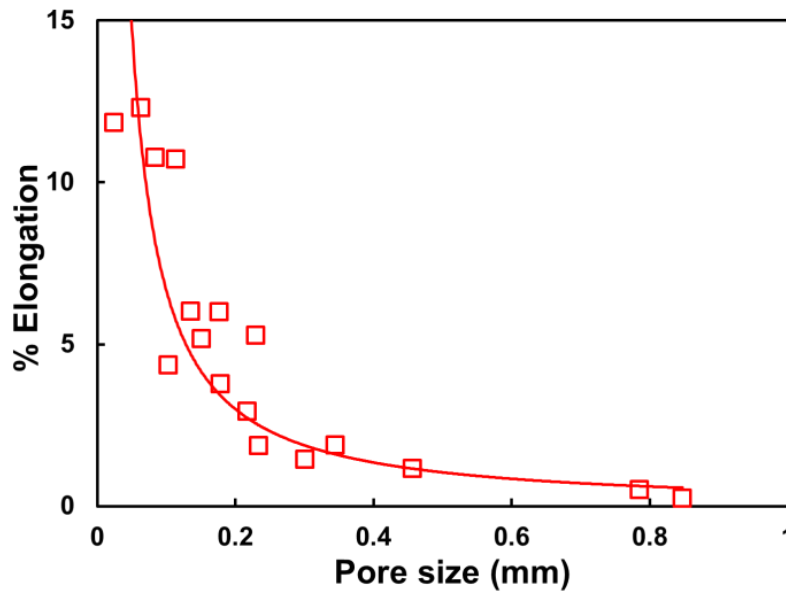


Figure 2.6. % Elongation versus size of the largest pore on the fracture surface [59]

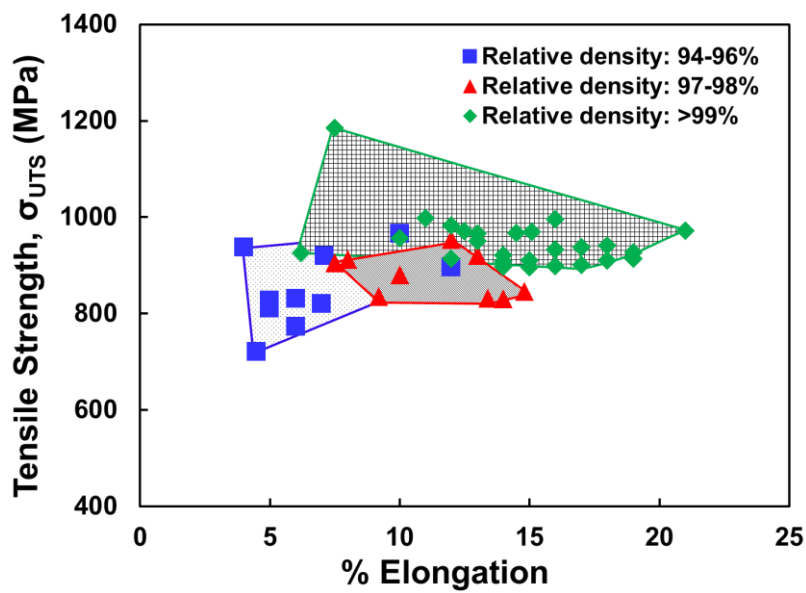


Figure 2.7. Tensile strength versus % elongation of lamellar PM Ti-6Al-4V alloy produced by BE and PA method [7,8,14,18,32–34,53,63–73,76–83,102]



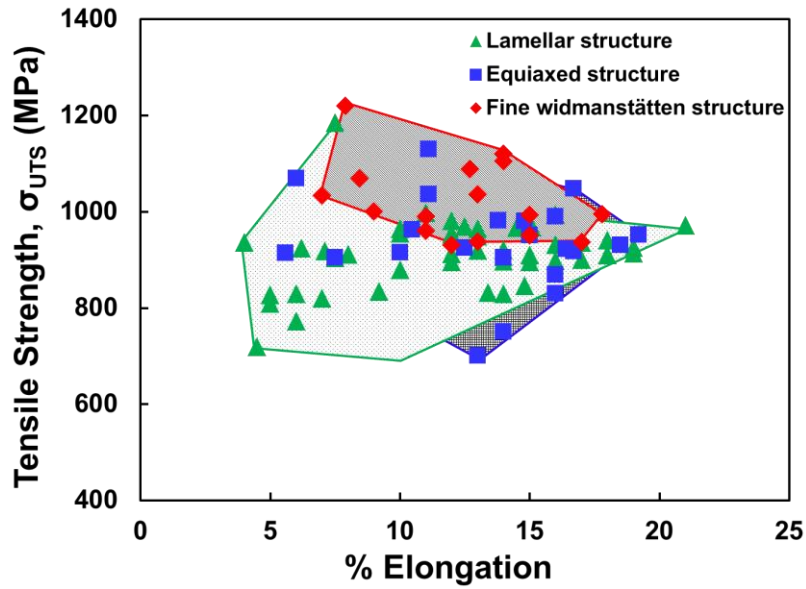


Figure 2.8 Tensile strength versus % elongation of Ti-6Al-4V alloy produced by BE and PA method with density > 99% [7,8,14,18,32–34,53,63–73,76–83,102]

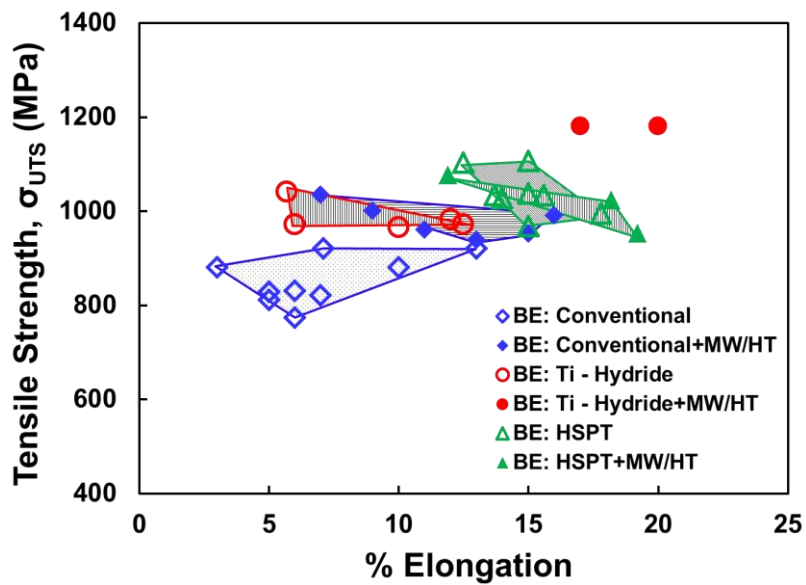


Figure 2.9 Tensile strength versus % elongation of Ti-6Al-4V alloy produced by different route [7–9,14,17,18,32–34,40,42,44,46,47,53,55,57,59,61,66–73,118,122,123,127,131]

## 2.10 References

- [1] J. Zhu, A. Kamiya, T. Yamada, W. Shi, K. Naganuma, Influence of boron addition on microstructure and mechanical properties of dental cast titanium alloys, *Mater. Sci. Eng. A.* 339 (2003) 53–62. doi:10.1016/S0921-5093(02)00102-8.
- [2] S. Tamirisakandala, R.B. Bhat, J.S. Tiley, D.B. Miracle, Grain refinement of cast titanium alloys via trace boron addition, *Scr. Mater.* 53 (2005) 1421–1426. doi:10.1016/j.scriptamat.2005.08.020.
- [3] A.D. Hartman, S.J. Gerdemann, J.S. Hansen, Producing lower-cost titanium for automotive applications, *Jom.* 50 (1998) 16–19. doi:10.1007/s11837-998-0408-1.
- [4] J.D. Cotton, R.D. Boyer, G.R. Weber, K.T. Slattery, Titanium Alloy development needs for commercial air frames Technical fellow, Washington, USA, 2008.
- [5] V.C. Petersen, V.K. Chandhok, C.A. Kelto, Hot isostatic pressing of large titanium shapes, in: F.H. Froes, J.E. Smugeresky (Eds.), *Powder Metall. Titan. Alloy.*, A.I.M.E, Warrendale, PA, USA, 1980: pp. 243–254.
- [6] W. Kroll, Verformbare Legierungen des Titans, *Z Met.* 29 (1937) 189–192.
- [7] S. Abkowitz, G.J. Kardys, S. Fujishiro, F.H. Froes, D. Eylon, Titanium Alloy Shapes from Elemental Blend Powder and Tensile and Fatigue Properties of Low Chloride Compositions, in: D. Eylon, F.H. Froes (Eds.), *Titan. Net Shape Technol.*, The Metall. Soc. of AIME, Warrendale, PA, USA, 1984: pp. 107–120.
- [8] S. Abkowitz, D. Rowell, Superior Fatigue Properties for Blended Elemental P/M Ti-6Al-4V, *JOM.* 38 (1986) 36–39. doi:10.1007/BF03257786.
- [9] F.H. Froes, S.J. Mashl, J.C. Hebeisen, V.S. Moxson, V. a. Duz, The technologies of titanium powder metallurgy, *Jom.* 56 (2004) 46–48. doi:10.1007/s11837-004-0252-x.
- [10] F.H. Froes, C. Suryanarayana, Powder Processing of Titanium Alloys, *Rev. Part. Mater.* 1 (1993) 223–275.
- [11] F.H. Froes, D. Eylon, Powder metallurgy of titanium alloys, *Int. Mater. Rev.* 35 (1990) 162–184. doi:10.1179/095066090790323984.
- [12] F.H. Froes, J.E. Smugeresky, eds., Titanium Powder Metallurgy, in: *Symp. AIME Annu. Meet.*, The Metall. Soc. of AIME, Las Vegas, Nevada, 1980.
- [13] I.S. Polkin, V.N. Samarov, Advances in Powder Metallurgy of Titanium, in: *Ti-2011*, Beijing, China, 2011: pp. 1817–1820.

- [14] J. Park, M.W. Toaz, D.H. Ro, E.N. Aqua, Blended Elemental Powder Metallurgy of Titanium Alloys, in: F.H. Froes, D. Eylon (Eds.), *Titan. Net Shape Technol.*, The Metall. Soc. of AIME, Warrendale, PA, USA, 1984: pp. 95–105.
- [15] C.F. Yolton, F.H. Froes, Conventional titanium powder production, in: M.A. Qian, F.H. Froes (Eds.), *Titan. Powder Metall.*, Elsevier Ltd, 2015: pp. 21–32.
- [16] F.H. Froes, D. Eylon, G.E. Eichelman, H.M. Burte, Developments in Titanium Powder Metallurgy, *JOM*. 32 (2014) 47–54. doi:10.1007/BF03354547.
- [17] F.H. Froes, D. Eylon, Titanium Powder Metallurgy—A Review, in: D. Eylon, F.H. Froes (Eds.), *Titan. Net Shape Technol.*, The Metallurgical Society of AIME, Warrendale, PA, USA, 1984: pp. 1–20.
- [18] F.H. Froes, D. Eylon, Titanium powder metallurgy – a review in *PM Aerospace Materials*, *MPR Publ.* 1 (1984) 1–19.
- [19] F.H. Froes, H.B. Bomberger, D. Eylon, R.G. Rowe, Potential of Titanium Powder Metallurgy, in: R.J. Cunningham, M. Schwartz (Eds.), *Compet. Adv. Met. Process.*, Society for the Advancement of Material and Process Engineering, Covina, CA (US), 1987: pp. 240–254.
- [20] M. Ashraf Imam, F.H.S. Froes, Low cost titanium and developing applications, *JOM*. 62 (2010) 17–20. doi:10.1007/s11837-010-0069-8.
- [21] M. Qian, Cold compaction of titanium and its alloys for near-net-shape or perfor fabrication, *Int. J. Powder Metall.* 46 (2010) 29–44.
- [22] I.M. Robertson, G.B. Schaffer, Review of densification of titanium based powder systems in press and sinter processing, *Powder Metall.* 53 (2010) 146–162. doi:10.1179/174329009X434293.
- [23] O.M. Ivasishin, D.G. Savvakina, V.A. Duz, M.V. Matviychuk, V.S. Moxson, Extra low impurity content powder metallurgy titanium and titanium alloys, in: *Titan. 2012*, International Titanium Association (ITA), Hilton, Atlanta, 2012.
- [24] C.Z. Yu, M.I. Jones, Investigation of chloride impurities in hydrogenated–dehydrogenated Kroll processed titanium powders, *Powder Metall.* 56 (2013) 304–309. doi:10.1179/1743290113Y.0000000055.
- [25] Z. Fan, H.J. Niu, B. Cantor, A.P. Miodownik, T. Saito, Effect of Cl on microstructure and mechanical properties of in situ Ti/TiB MMCs produced by a blended elemental powder metallurgy method, *J. Microsc.* 185 (1997) 157–167. doi:10.1046/j.1365-2818.1997.d01-622.x.
- [26] M. Kumagai, K. Shibue, M.-S. Kim, M. Yonemitsu, Influence of chlorine on the oxidation behavior of TiAl–Mn intermetallic compound, *Intermetallics*. 4 (1996) 557–566. doi:10.1016/0966-9795(96)00043-X.

- [27] K. Majima, T. Hirata, K. Shouji, Effects of purity of titanium powder and porosity on static tensile properties of sintered titanium specimens, *J. Jpn. Inst. Met.* 51 (1987) 1194–1200.
- [28] S. Abkowitz, H. Fisher, Titanium alloy components manufacture from blended elemental powder and the qualification process, in: M. Qian, F.H. Froes (Eds.), *Titan. Powder Metall.*, Elsevier Ltd, 2014.
- [29] M. Yan, H.P. Tang, M. Qian, Scavenging of oxygen and chlorine from powder metallurgy (PM) titanium and titanium alloys, in: Q. M., F.H. Froes (Eds.), *Titan. Powder Metall.*, Elsevier, 2015: pp. 253–276. doi:10.1016/B978-0-12-800054-0.00015-0.
- [30] S.M. El-Soudani, Powder-based titanium alloys: properties and selection, in: M. Qian, F. Froes (Eds.), *Titan. Powder Metall.*, Elsevier, 2015: pp. 469–496. doi:10.1016/B978-0-12-800054-0.00025-3.
- [31] F.H. Froes, Enhanced Fatigue Behaviour in Blended Elemental PM Titanium Alloys, *Met. Powder Rep.* 42 (1987) 217–218.
- [32] P.J. Andersen, V.M. Svoiatytsky, F.H. Froes, Y. Mahajan, D. Eylon, Fracture behavior of blended elemental P/M titanium alloys, in: *Mod. Dev. Powder Metall.*, 1981: pp. 537–549.
- [33] Y.T. Lee, M. Peters, G. Wirth, Effects of thermomechanical treatment on microstructure and mechanical properties of blended elemental Ti-6Al-4V compacts, *Mater. Sci. Eng. A.* 102 (1988) 105–114. doi:10.1016/0025-5416(88)90538-1.
- [34] D. Eylon, R.G. Vogt, F.H. Froes, Property Improvement of Low Chlorine Titanium Alloy Blended Elemental Powder Compacts by Microstructure Modification.(Retroactive Coverage), *Prog. Powder Metall.* 42 (1986) 625–634.
- [35] E. Gregory, USA Patent, Fabrication of Niobium Superconductor Alloys, 1969.
- [36] J. Greenspan, F.J. Rizzitano, E. Scala, Metal Matrix Composites by Decomposition Sintering of Titanium Hydride, 1970. <http://oai.dtic.mil/oai/oai?verb=getRecord&metadataPrefix=html&identifier=AD0722258>.
- [37] K. Obara, Y. Nishino, S. Matsumoto, Process for producing a sintered article of a titanium alloy, (1976). <https://www.google.com/patents/US3950166>.
- [38] D.H. Savvakina, M.M. Humenyak, M. V Matviichuk, O.H. Molyar, Role of Hydrogen in the Process of Sintering of Titanium Powders, *Mater. Sci.* 47 (2012) 651–661. doi:10.1007/s11003-012-9440-y.
- [39] O.M. Ivasishin, D.G. Savvakina, M.M. Gumenyak, O.B. Bondarchuk, Role of

Surface Contamination in Titanium PM, *Key Eng. Mater.* 520 (2012) 121–132.

- [40] O.M. Ivasishin, V.M. Anokhin, A.N. Demidik, D.G. Savvakín, Cost-Effective Blended Elemental Powder Metallurgy of Titanium Alloys for Transportation Application, *Key Eng. Mater.* 188 (2000) 55–62. doi:10.4028/www.scientific.net/KEM.188.55.
- [41] O.M. Ivasishin, D.G. Savvakín, F.H. Froes, V.S. Mokson, K. Bondareva, Synthesis of the Ti-6 Al-4 V alloy having low residual porosity by powder metallurgy method, *Poroshkovaya Metall.* 7 (2002) 54–64.
- [42] O.M. Ivasishin, D.G. Savvakín, I.S. Bielov, V.S. Moxson, V.A. Duz, R. Davies, C. Lavender, BEPM Synthesis of Ti-6Al-4V Alloy Using Hydrogenated Titanium, in: *Eur. Congr. Exhib. Powder Metall. Eur. PM Conf. Proc., The European Powder Metallurgy Association*, 2005: pp. 115–120.
- [43] H.T. Wang, M. Lefler, Z.Z. Fang, T. Lei, S.M. Fang, J.M. Zhang, Q. Zhao, Titanium and titanium alloy via sintering of TiH<sub>2</sub>, in: *Key Eng. Mater., Trans Tech Publ*, 2010: pp. 157–163.
- [44] P. Sun, *Powder Metallurgy Titanium by the Hydrogen Sintering and Phase Transformation (HSPT) Process*, University of Utah, 2015.
- [45] P. Sun, Z.Z. Fang, M. Koopman, Y. Xia, J. Paramore, K.S.R. Chandran, Y. Ren, J. Lu, Phase Transformations and Formation of Ultra-Fine Microstructure During Hydrogen Sintering and Phase Transformation (HSPT) Processing of Ti-6Al-4V, *Metall. Mater. Trans. A.* 46 (2015) 5546–5560.
- [46] Z.Z. Fang, P. Sun, H. Wang, Hydrogen Sintering of Titanium to Produce High Density Fine Grain Titanium Alloys, *Adv. Eng. Mater.* 14 (2012) 383–387. doi:10.1002/adem.201100269.
- [47] P. Sun, Z.Z. Fang, M. Koopman, A Comparison of Hydrogen Sintering and Phase Transformation (HSPT) Processing with Vacuum Sintering of CP-Ti, *Adv. Eng. Mater.* 15 (2013) 1007–1013.
- [48] F. Cao, K.S. Ravi Chandran, P. Kumar, P. Sun, Z. Zak Fang, M. Koopman, New Powder Metallurgical Approach to Achieve High Fatigue Strength in Ti-6Al-4V Alloy, *Metall. Mater. Trans. A.* 47 (2016) 2335–2345. doi:10.1007/s11661-016-3409-7.
- [49] F. Cao, K.S. Ravi Chandran, Fatigue Performance of Powder Metallurgy (PM) Ti-6Al-4V Alloy: A Critical Analysis of Current Fatigue Data and Metallurgical Approaches for Improving Fatigue Strength, *JOM.* 68 (2016) 735–746. doi:10.1007/s11837-016-1821-5.
- [50] V. Moxson, O.N. Senkov, F.H. Froes, Innovations in titanium powder processing, *JOM.* 52 (2000) 24–26. doi:10.1007/s11837-000-0027-y.

- [51] J.C. Withers, Production of titanium powder by an electrolytic method and compaction of the powder, in: M. Qian, F.H. Froes (Eds.), *Titan. Powder Metall. Sci. Technol. Appl.*, Butterworth-Heinemann, 2015: pp. 33–49.
- [52] Y.F. Yang, S.D. Luo, G.B. Schaffer, M. Qian, Impurity scavenging, microstructural refinement and mechanical properties of powder metallurgy titanium and titanium alloys by a small addition of cerium silicide, *Mater. Sci. Eng. A*. 573 (2013) 166–174. doi:10.1016/j.msea.2013.02.042.
- [53] T. Fujita, A. Ogawa, C. Ouchi, H. Tajima, Microstructure and properties of titanium alloy produced in the newly developed blended elemental powder metallurgy process, *Mater. Sci. Eng. A*. 213 (1996) 148–153. doi:10.1016/0921-5093(96)10232-X.
- [54] O.M. Ivasishin, A.N. Demidik, D.G. Savvakín, Use of titanium hydride for the synthesis of titanium aluminides from powder materials, *Powder Metall. Met. Ceram.* 38 (1999) 482–487. doi:10.1007/BF02676065.
- [55] O.M. Ivasishin, D.G. Savvakín, F.H. (Sam) Froes, K.A. Bondareva, Synthesis of Alloy Ti — 6Al — 4V with Low Residual Porosity by a Powder Metallurgy Method, *Powder Metall. Met. Ceram.* 41 (2002) 382–390. doi:10.1023/A:1021117126537.
- [56] O.M. Ivasishin, D.G. Savvakín, F.H. Froes, V.S. Mokson, K.A. Bbondareva, Synthesis of the Ti-6 Al-4 V alloy having low residual porosity by powder metallurgy method, *Poroškovaâ Metall.* (2002) 54–64. <http://cat.inist.fr/?aModele=afficheN&cpsidt=15293540> (accessed February 3, 2016).
- [57] O.M. Ivasishin, D.G. Savvakín, V.S. Moxson, K. Bondareval, Titanium powder metallurgy for automotive components, *Mater. Technol.* 17 (2002) 20–25.
- [58] F. Cao, P. Kumar, M. Koopman, C. Lin, Z.Z. Fang, K.S.R. Chandran, Understanding competing fatigue mechanisms in powder metallurgy Ti–6Al–4V alloy: Role of crack initiation and duality of fatigue response, *Mater. Sci. Eng. A*. 630 (2015) 139–145. doi:10.1016/j.msea.2015.02.028.
- [59] P. Kumar, K.S. Ravi Chandran, F. Cao, M. Koopman, Z.Z. Fang, The Nature of Tensile Ductility as Controlled by Extreme-Sized Pores in Powder Metallurgy Ti-6Al-4V Alloy, *Metall. Mater. Trans. A*. (2016). doi:10.1007/s11661-016-3419-5.
- [60] J.D. Paramore, Z. Zak Fang, P. Sun, Hydrogen sintering of titanium and its alloys, in: *Titan. Powder Metall. Sci. Technol. Appl.*, 2015. doi:10.1016/B978-0-12-800054-0.00010-1.
- [61] J.D. Paramore, Z.Z. Fang, P. Sun, M. Koopman, K.S.R. Chandran, M. Dunstan, A powder metallurgy method for manufacturing Ti-6Al-4V with wrought-like

- microstructures and mechanical properties via hydrogen sintering and phase transformation (HSPT), *Scr. Mater.* 107 (2015) 103–106.
- [62] Y. Yan, G.L. Nash, P. Nash, Effect of density and pore morphology on fatigue properties of sintered Ti–6Al–4V, *Int. J. Fatigue*. 55 (2013) 81–91. doi:10.1016/j.ijfatigue.2013.05.015.
  - [63] Y. Kim, E.-P. Kim, Y.-B. Song, S.H. Lee, Y.-S. Kwon, Microstructure and mechanical properties of hot isostatically pressed Ti–6Al–4V alloy, *J. Alloys Compd.* 603 (2014) 207–212. doi:10.1016/j.jallcom.2014.03.022.
  - [64] D. Eylon, F.H. Froes, D.G. Heggie, P.A. Blenkinsop, R.W. Gardiner, Influence of thermomechanical processing on low cycle fatigue of prealloyed Ti-6Al-4V powder compacts, *Metall. Trans. A.* 14 (1983) 2497–2505.
  - [65] L. Levin, R.G. Vogt, D. Eylon, F.H. Froes, Fatigue Resistance Improvement of Ti–6 Al–4 V by Thermochemical Treatment, *Titanium--Science Technol.* 4 (1984) 2107–2114.
  - [66] I. Weiss, D. Eylon, M.W. Toaz, F.H. Froes, Effect of isothermal forging on microstructure and fatigue behavior of blended elemental Ti-6Al-4V powder compacts, *Metall. Trans. A.* 17 (1986) 549–559. doi:10.1007/BF02643962.
  - [67] P.R. Smith, C.M. Cooke, A. Patel, F.H. Froes, Evaluation of Ti-6Al-4V powder metallurgy plate, *Prog. Powder Met.* 38 (1983) 339–359.
  - [68] P.R. Smith, C.M. Cooke, F.H. Froes, Evaluation of Blended Elemental Ti-6Al-4V Plate in Three Microstructural Conditions, in: *Mater. Process. Contin. Innov.*, Society for the Advancement of Material and Process Engineering, Covina, CA, USA, 1983: pp. 406–421.
  - [69] M. Hagiwara, Y. Kaieda, Y. Kawabe, S. Miura, Fatigue Property Enhancement of .ALPHA.-.BETA. Titanium Alloys by Blended Elemental P/M Approach., *ISIJ Int.* 31 (1991) 922–930. doi:10.2355/isijinternational.31.922.
  - [70] V.S. Moxson, P. Sjoblom, M.J. Trzcinski, Ti–6 Al–4 V Properties Achieved via Extra Low Chlorine Titanium Powder, *Adv. Powder Metall. Part. Mater.* 6 (1992) 125–140.
  - [71] C. Haase, R. Lapovok, H.P. Ng, Y. Estrin, Production of Ti–6Al–4V billet through compaction of blended elemental powders by equal-channel angular pressing, *Mater. Sci. Eng. A.* 550 (2012) 263–272. doi:10.1016/j.msea.2012.04.068.
  - [72] G.I. Friedman, Titanium Powder Metallurgy., *Int. J. Powder Metall.* 6 (1970) 43–55.
  - [73] Y. Mahajan, D. Eylon, R. Bacon, F.H. Froes, Microstructure Property

- Correlation in Cold Pressed and Sintered Elemental Ti--6 Al--4 V Powder Compacts, in: F.H. Froes, J.E. Smugeresky (Eds.), Powder Metall. Titan. Alloy., The Metall. Soc. of AIME, Warrendale, PA, USA, 1980: pp. 189–202.
- [74] G. Wirth, K.-J. Grundhoff, W. Smarsly, Correlations between post-hip treatment, resulting microstructure and fatigue behaviour of prealloyed Ti 6 Al 4 V powder compacts., *Overcoming Mater. Boundaries*. 17 (1985) 125–134.
  - [75] A.A. Sheinker, G.R. Chanani, J.W. Bohlen, Evaluation and application of prealloyed titanium P/M parts for airframe structures, *Int. J. Powder Metall.* 23 (1987) 171–176.
  - [76] J.H. Moll, C.F. Yolton, Review and status of titanium materials produced from spherical pre-alloyed powder, in: *Int. Powder Metall. Conf.*, The Metall. Soc. of AIME, Orlando, FL, USA, 1988: pp. 107–120.
  - [77] L. Xu, R. Guo, C. Bai, J. Lei, R. Yang, Effect of Hot Isostatic Pressing Conditions and Cooling Rate on Microstructure and Properties of Ti–6Al–4V Alloy from Atomized Powder, *J. Mater. Sci. Technol.* 30 (2014) 1289–1295.
  - [78] R.E. Peebles, L.D. Parsons, Study of Production Methods of Aerospace Quality Titanium Alloy Powder, in: F.H. Froes, D. Eylon (Eds.), *Titan. Net Shape Technol.*, The Metall. Soc. of AIME, Warrendale, PA, USA, 1984: pp. 21–28.
  - [79] K. Zhang, J. Mei, N. Wain, X. Wu, Effect of Hot-Isostatic-Pressing Parameters on the Microstructure and Properties of Powder Ti-6Al-4V Hot-Isostatically-Pressed Samples, *Metall. Mater. Trans. A*. 41 (2010) 1033–1045. doi:10.1007/s11661-009-0149-y.
  - [80] D. Bozic, D. Sekulic, J. Stasic, V. Rajkovic, M.T. Jovanovic, The influence of microstructural characteristics and contaminants on the mechanical properties and fracture topography of low cost Ti6Al4V alloy, *Int. J. Mater. Res.* 99 (2008) 1268–1274.
  - [81] W.H. Kao, D. Eylon, C.F. Yolton, F.H. Froes, Effect of Temporary Alloying by Hydrogen(Hydrovac) on the Vacuum Hot Pressing and Microstructure of Titanium Alloy Powder Compacts, *Prog. Powder Met.* 37 (1981) 289–301.
  - [82] G. Abouelmagd, H.P. Büchkremer, E. El-Magd, D. Stöver, Mechanical properties of a TiAl6V4 alloy processed by powder metallurgy, *J. Mater. Process. Technol.* 37 (1993) 583–597.
  - [83] J.P. Herteman, D. Eylon, F.H. Froes, Mechanical properties of advanced titanium powder metallurgy compacts, *Powder Met. Int.* 17 (1985) 116–118.
  - [84] G. Welsch, R. Boyer, E.W. Collings, eds., *Materials properties handbook: titanium alloys*, ASM international, 1993.



- [85] D.J. Chronister, S.W. Scott, D.R. Stickle, D. Eylon, F.H. Froes, Induction skull melting of titanium and other reactive alloys, *JOM*. 38 (1986) 51–54.
- [86] D. Eylon, C.M. Pierce, Effect of microstructure on notch fatigue properties of Ti-6Al-4V, *Metall. Trans. A*. 7 (1976) 111–121.
- [87] R.G. Sherman, H.D. Kessler, Investigation of the heat treatability of the 6% aluminum-4% vanadium titanium based alloy, *Trans. ASM*. 48 (1956) 657–676.
- [88] G.R. Yoder, L.A. Cooley, T.W. Crooker, Observations on microstructurally sensitive fatigue crack growth in a Widmanstätten Ti-6Al-4V alloy, *Metall. Trans. A*. 8 (1977) 1737–1743.
- [89] H. Margolin, Y. Mahajan, Void formation, void growth and tensile fracture in Ti-6Al-4V, *Metall. Trans. A*. 9 (1978) 781–791.
- [90] K. Bose, N.C. Birla, D.B. Goel, No Title, *Trans. Indian Inst. Met.* 36 (1983) 181–188.
- [91] J.C. Williams, E.A. Starke, The role of thermomechanical processing in tailoring the properties of aluminum and titanium alloys, *Deform. Process. Struct.* (1984) 306–314.
- [92] D.P. DeLo, R.E. Dutton, S.L. Semiatin, H.R. Piehler, Modeling of hot isostatic pressing and hot triaxial compaction of Ti-6Al-4V powder, *Acta Mater.* 47 (1999) 3159–3167.
- [93] D.P. Delo, H.R. Piehler, Early stage consolidation mechanisms during hot isostatic pressing of Ti-6Al-4V powder compacts, *Acta Mater.* 47 (1999) 2841–2852.
- [94] D.B. Dawson, M.G. Ulitchny, Characterization of the Tensile Properties of Hot Isostatically Pressed Ti-6Al-4V-2Sn, in: F.H. Froes, J.E. Smugeresky (Eds.), *Powder Metall. Titan. Alloy., The Metallurgical Society of AIME*, 1980: pp. 115–126.
- [95] A. Gogia, D. Banerjee, N.C. Birla, Effect of thermomechanical history on the microstructure of  $\alpha + \beta$  titanium alloys, *Trans. Indian Inst. Met.* 36 (1983) 200–207.
- [96] I. Weiss, F.H. Froes, D. Eylon, G.E. Welsch, Modification of alpha morphology in Ti-6Al-4V by thermomechanical processing, *Metall. Trans. A*. 17 (1986) 1935–1947.
- [97] I. Weiss, G.E. Welsch, F.H. Froes, D. Eylon, Recovery, Recrystallization and Mechanical Properties in Ti-6Al-4V alloy, in: H.J. McQueen, J.-P. Bailon, J.I. Dickson, J.J. Jonas, M.G. Akben (Eds.), *Int. Conf. Strength Met. Alloy. (ICSMA 7)*, Pergamon Press, Montreal, Canada, 1985: p. 1073.

- [98] Y.R. Mahajan, D. Eylon, C. Kelto, Modification of Titanium Powder Metallurgy Alloy Microstructures by Strain Energizing and Rapid Omni-Directional Compaction, 1985.
- [99] D. Eylon, C.A. Kelto, A.F. Hayes, F.H. Froes, Low temperature compaction of titanium alloys by rapid omnidirectional compaction (ROC), Prog. Powder Metall. 43 (1987) 33–47.
- [100] F.H. Froes, D. Eylon, G. Wirth, K.J. Grundhoff, W. Smarsly, Fatigue properties of hot isostatically pressed Ti-6Al-4V powders, Prog. Powder Met. States). 38 (1983) 36–41.
- [101] D. Eylon, P.R. Smith, S.W. Schwenker, F.H. Froes, Status of titanium powder metallurgy, in: Ind. Appl. Titan. Zircon. Third Conf., ASTM International, Philadelphia, PA, USA, 1984: pp. 48–65.
- [102] O.M. Ivasishin, Cost-effective manufacturing of titanium parts with powder metallurgy approach, in: Mater. Forum, 2005: pp. 1–8.
- [103] A. Hadrboletz, B. Weiss, Fatigue behaviour of iron based sintered material: a review, Int. Mater. Rev. 42 (1997) 1–44. doi:10.1179/imr.1997.42.1.1.
- [104] N. Chawla, X. Deng, Microstructure and mechanical behavior of porous sintered steels, Mater. Sci. Eng. A. 390 (2005) 98–112. doi:10.1016/j.msea.2004.08.046.
- [105] R.J. Bourcier, D.A. Koss, R.E. Smelser, O. Richmond, The influence of porosity on the deformation and fracture of alloys, Acta Metall. 34 (1986) 2443–2453. doi:10.1016/0001-6160(86)90147-1.
- [106] L.H. Cope, The mechanical properties of nuclear cermets, Metall. Publ. August 1971-December 1977 as Met. Met. Form. 72 (1965) 165.
- [107] M.K. Surappa, E. Blank, J.C. Jaquet, Effect of macro-porosity on the strength and ductility of cast Al-7Si-0.3Mg alloy, Scr. Metall. 20 (1986) 1281–1286. doi:10.1016/0036-9748(86)90049-9.
- [108] P. Kumar, K.S. Ravi Chandran, A quantitative relationship to predict the effect of Extreme-sized pores on Tensile Ductility of Powder Metallurgy Ti-6Al-4V alloy, in: Titanium-2015, The Minerals, Metals and Materials Society, San Diego, CA, 2015.
- [109] G. Lutjering, J. Albrecht, O.M. Ivasishin, Influence of cooling rate and beta grain size on the tensile properties of ( $\alpha$ + $\beta$ ) Ti-alloys, in: Titanium'95., 1995: pp. 1163–1170.
- [110] G. Lütjering, Influence of processing on microstructure and mechanical properties of ( $\alpha$ + $\beta$ ) titanium alloys, Mater. Sci. Eng. A. 243 (1998) 32–45. doi:10.1016/S0921-5093(97)00778-8.

- [111] E.W. Collings, The physical metallurgy of titanium alloys, ASM International, Metals Park, Ohio, 1984.
- [112] M.J. Donachie, Titanium: A Tenchincal Guide, Second, ASM International, Materials Park, Ohio, 2000.
- [113] G. Lütjering, J.C. Williams, Titanium, Springer, 2003.
- [114] H.J. Rack, J.I. Qazi, Titanium alloys for biomedical applications, Mater. Sci. Eng. C. 26 (2006) 1269–1277.
- [115] J. Tiley, T. Searles, E. Lee, S. Kar, R. Banerjee, J.C. Russ, H.L. Fraser, Quantification of microstructural features in  $\alpha/\beta$  titanium alloys, Mater. Sci. Eng. A. 372 (2004) 191–198.
- [116] G. Terlinde, H.-J. Rathjen, K.-H. Schwalbe, Microstructure and fracture toughness of the aged,  $\beta$ -Ti Alloy Ti-10V-2Fe-M, Metall. Trans. A. 19 (1988) 1037–1049.
- [117] S. Kanamori, E. Abe, T. Tagawa, T. Miyata, Effects of constraint and grain size on ductility and toughness in Ti Alloys, in: 10th Int. Conf. Fract., Honolulu (USA), 2001.
- [118] O. Ivasishin, V. Moxson, Low-cost titanium hydride powder metallurgy, in: M. Qian, F.H. Froes (Eds.), Titan. Powder Metall. Sci. Technol. Appl., Elsevier Inc., Library of the Congress, New York, 2015: pp. 117–148.
- [119] V. Bhosle, E.G. Baburaj, M. Miranova, K. Salama, Dehydrogenation of nanocrystalline TiH<sub>2</sub> and consequent consolidation to form dense Ti, Metall. Mater. Trans. A. 34 (2003) 2793–2799. doi:10.1007/s11661-003-0180-3.
- [120] O.M. Ivasishin, D.G. Savvakina, V.S. Moxson, V.A. Duz, C. Lavender, Production of titanium components from hydrogenated titanium powder: optimization of parameters, in: M. Niinomi, S. Akiyama (Eds.), Ti-2007 Sci. Technol., Japan Institute of Metals, 2007: pp. 757–760.
- [121] E. Nyberg, M. Miller, K. Simmons, K.S. Weil, Microstructure and mechanical properties of titanium components fabricated by a new powder injection molding technique, Mater. Sci. Eng. C. 25 (2005) 336–342. doi:10.1016/j.msec.2005.04.006.
- [122] V. V. Joshi, C. Lavender, V. Moxon, V. Duz, E. Nyberg, K.S. Weil, Development of Ti-6Al-4V and Ti-1Al-8V-5Fe Alloys Using Low-Cost TiH<sub>2</sub> Powder Feedstock, J. Mater. Eng. Perform. 22 (2013) 995–1003. doi:10.1007/s11665-012-0386-x.
- [123] P. Kumar, K.S. Ravichandran, F. Cao, P. Sun, M. Koopman, Z.Z. Fang, Effects of Powder Processing and Sintering on Tensile Ductility of Pm Ti-6Al-4V Alloy

- Made by Hydrogen Sintering of Titanium Hydride Powders, in: Ti-2015 Sci. Technol., The Minerals, Metals and Materials Society, 2015: pp. 1355–1359.
- [124] W.R. Kerr, The effect of hydrogen as a temporary alloying element on the microstructure and tensile properties of Ti-6Al-4V, *Metall. Trans. A.* 16 (1985) 1077–1087.
  - [125] D.H. Kohn, P. Ducheyne, Microstructural refinement of  $\beta$ -sintered and Ti-6Al-4V porous-coated by temporary alloying with hydrogen, *J. Mater. Sci.* 26 (1991) 534–544.
  - [126] X.L. Han, Q. Wang, D.L. Sun, H.X. Zhang, First-principles study of the effect of hydrogen on the Ti self-diffusion characteristics in the alpha Ti-H system, *Scr. Mater.* 56 (2007) 77–80. doi:10.1016/j.scriptamat.2006.06.037.
  - [127] J.D. Paramore, *Titanium Powder Metallurgy*, Butterworth-Heinemann: Oxford, 2015.
  - [128] G. Shibo, Q. Xuanhui, H. Xinbo, Z. Ting, D. Bohua, Powder injection molding of Ti-6Al-4V alloy, *J. Mater. Process. Technol.* 173 (2006) 310–314. doi:10.1016/j.jmatprotec.2005.12.001.
  - [129] G.C. Obasi, O.M. Ferri, T. Ebel, R. Bormann, Influence of processing parameters on mechanical properties of Ti-6Al-4V alloy fabricated by MIM, *Mater. Sci. Eng. A.* 527 (2010) 3929–3935. doi:10.1016/j.msea.2010.02.070.
  - [130] K. Kimura, M. Masaki, M. Murayama, Y. Kako, Development of Manufacturing Technology and Its Application in Titanium, *Nippon Steel Tech. Rep.* (2002) 1–5. <http://www.nssmc.com/en/tech/report/nsc/pdf/8501.pdf>.
  - [131] J.D. Paramore, Relationship between processing, structure, and properties of titanium alloys produced by hydrogen sintering and phase transformation, University of Utah, 2015.

## **CHAPTER 3**

### **MATERIALS AND EXPERIMENTAL PROCEDURE**

### 3.1 Starting Powder Preparation

For this study, -325 mesh, -20/+60-mesh titanium hydride (CP-TiH<sub>2</sub>), and -325 mesh 60 wt.% Al - 40 wt.% V (60Al/40V) master alloy powder were used as starting material. These powders were received from Reading alloys, PA, USA. The coarse (-20/+60 mesh) powder was used to minimize the interstitial contamination in the initial powder. The -20/+60-mesh powder was jar milled using stainless steels ball ( 2.54 cm) as grinding media for 30 min. in Ar atmosphere. After milling, using an appropriate sieve, -325 mesh sized titanium hydride powder was produced. Also, -400-mesh 60Al-40V master alloy powder was produced by sieving as-received -325-mesh master alloy powder using a standard sieve.

The milled and as-received -325-mesh TiH<sub>2</sub> powder were blended with -400-mesh and -325-mesh size 60Al/40V master alloy in a suitable proportion to obtain the Ti-6Al-4V composition. Blending was achieved by mixing the powders in a homemade blending jar with lifters. The blending was carried out for a minimum of 24 hrs. to ensure complete homogenization of powders.

### 3.2 Powder Compaction

The blended powders were cold iso-static pressed (CIPed) to make green compacts in a cylinder, 13 mm in diameter and 90 mm in length. For CIPing, rubber bags were used as mold for the green compacts. Approximately 65 gm of blended powder was poured into the rubber mold using a funnel. After hand tapping for approximately 10 minutes (approximately 500 taps), bags were vacuumed to remove any entrapped air in the interstitials and then tightly sealed. The sealed bags were transferred to the cold isostatic

press manufactured by American Isostatic Presses, model CP 360 (AIP CP360). A pressure of 350 MPa was applied for 7 min. to prepare green compact.

### **3.3 Sintering**

All the sintering and dehydrogenation processes were conducted in a custom-built tube furnace. The tube furnace is equipped with a high vacuum system and capable of reaching a temperature of 1400°C. The atmosphere in the tube of the furnace was controlled using mass flow controllers, one for ultra-high purity hydrogen (H<sub>2</sub>) and one for ultra-high purity argon (Ar). The high vacuum levels were achieved using an Agilent AX-65 diffusion pump. A vacuum level of 10<sup>-5</sup> Pa can be achieved in the tube furnace. All the specimens were sintered in the shape of a cylindrical bar. The samples for mechanical testing were machined from the as-sintered bar.

#### **3.3.1 Hydrogen Sintering and Phase Transformation (HSPT) Processing**

The powder mixture composed of -325-mesh titanium hydride powders and -325-mesh 60Al/40V master alloy powder were compacted using the CIP. The compacted samples were transferred to the tube furnace and the furnace was flushed with pure Ar. The furnace was vacuumed to 10<sup>-5</sup> Pa and then the furnace was switched on to start heating. The compacted samples were heated to 1200°C at a rate of 10°C/min and sintered at that temperature for 4 hrs in a flowing Ar/H<sub>2</sub> mixture. The sintered TiH<sub>2</sub> compacts were then cooled at a rate of 5°C/min to 650°C. The samples were held at 650°C for 4 hrs to complete eutectoid transformation in the material, followed by cooling to room temperature. The samples were then dehydrogenated by holding at 750°C for 12

hrs in a vacuum. The temperature was controlled within  $\pm 1$ . The complete processing scheme is shown in Figure 1.

### 3.3.2 Thermal Cyclic Sintering

Thermal cyclic sintering was performed in the same approach as discussed above. The compacted samples were thermally cycled across the  $\alpha/\beta$  phase transition temperature of Ti-6Al-4V alloy (1010°C) with 10°C and 20°C thermal amplitude in high vacuum for a varying number of cycles. In the present study, the number of thermal cycles varied between 16, 32, 48, 96, 144, and 192 cycles. The heating rate and the cooling rate was 25°C/min during the thermal cyclic sintering.

### 3.3.3 Isothermal Vacuum Sintering

Similar experimental procedures were followed in preparing the green compact from the powder mixture of Ti-6Al-4V alloy composition. The compacted samples were heated at a rate of 25°C/min to 1010°C. The sintering was done at that temperature for varying set of time in high vacuum ( $10^{-5}$  Pa). In this investigation, five different temperatures such as 0.9 hrs, 1.3 hrs, 2.7 hrs, 5.4 hrs, and 10 hrs were considered.

## 3.4 Density and Chemical Analysis

The density of as-sintered Ti-6Al-4V alloy specimens was directly measured using Archimedes' principle as

$$\rho = W_{air} \times \rho_{water} / (W_{air} - W_{water})$$

Densities of the samples were also determined using a Micromeritics pycnometer,



model AccuPycII.

The average Al, V, and C composition of the dehydrogenated alloy were determined at Aston Metallurgical Laboratory, IL, USA. Oxygen, hydrogen, and nitrogen compositions were determined using a Leco TCH 600 analyzer.

### **3.5 Microstructure Analysis**

Microstructure analysis was performed on the samples after processing to identify the changes in the microstructure as a function of sintering temperature and time. The samples were first sectioned using a sectioning saw (Allied High Tech – TechCut 5). After sectioning, each specimen was hot mounted in a mounting resin using a hot press (Buhler). The samples were first ground with 320-grit SiC paper to remove the coarse scratches. The samples were then manually polished following a standard polishing procedure. Etching was done using Kroll's reagent to reveal the microstructure. Microstructural analysis is performed using an optical microscope (Olympus OLS3500) and SEM (FEI Nova NanoSEM, and Hitachi S4700 FESEM). The image analysis software imageJ was used to determine the porosity fraction in the microstructures.

### **3.6 Mechanical Testing and Fractography**

For mechanical testing, samples were sent out for machining into round tensile bars and fatigue bars. All the machining for tensile specimens was performed by Westmoreland Testing and Research (WMT&R), PA, USA, while samples for fatigue testing were machined at Chemistry machining shop at University of Utah, Salt Lake City, USA. The tensile bars are machined to ASTM E8 specifications as shown in Figure (3.2).

The fatigue bars have a 0.25” diameter by 0.5” length gauge with 0.75” diameter smooth ends (Figure 3.3). The fatigue samples were mirror polished before testing in order to nullify the surface effects. The samples were polished using 320-grit SiC paper followed by 400-, 600-, 800-, and 1200-grit SiC paper. The final polishing was done using 5  $\mu\text{m}$ , 1  $\mu\text{m}$  and 0.3  $\mu\text{m}$  alumina powder solution (in water). Both tensile tests and fatigue tests were performed using an MTS servo hydraulic Test System capable of up to 100 kN of force and 60 Hz cyclic loading. Control and data acquisition are accomplished using MTS TestSuite software. The static tensile tests are performed at a strain rate of  $2 \times 10^{-4}$  s $^{-1}$ . Fatigue tests were performed under load control with a cyclic frequency of 35 Hz (sine wave) at the stress ratio ( $\sigma_{\text{min}}/\sigma_{\text{max}}$ ) of 0.1 in laboratory atmosphere at room temperature.

The fracture surfaces from the mechanical tests were examined in a scanning electron microscope (SEM) to determine the nature of the crack/fracture initiation. The projected area of pore that had initiated fracture in each sample was determined by using the grid technique and with the aid of imageJ image analysis software.

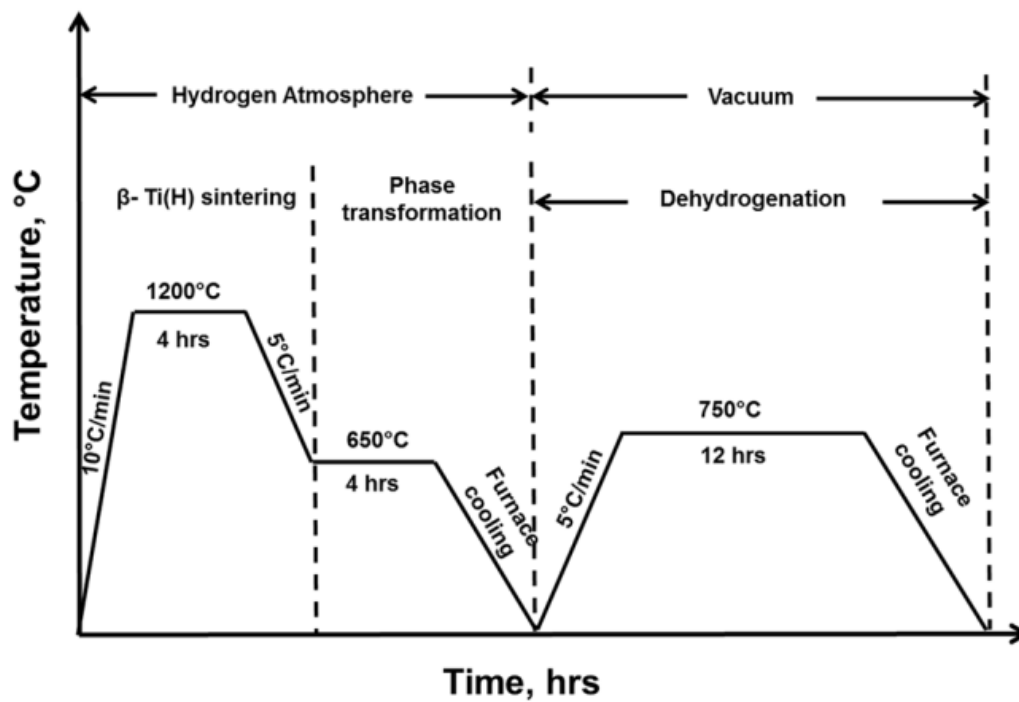


Figure 3.1 Schematic of temperature and time profile of the HSPT process used for making PM Ti-6Al-4V alloy

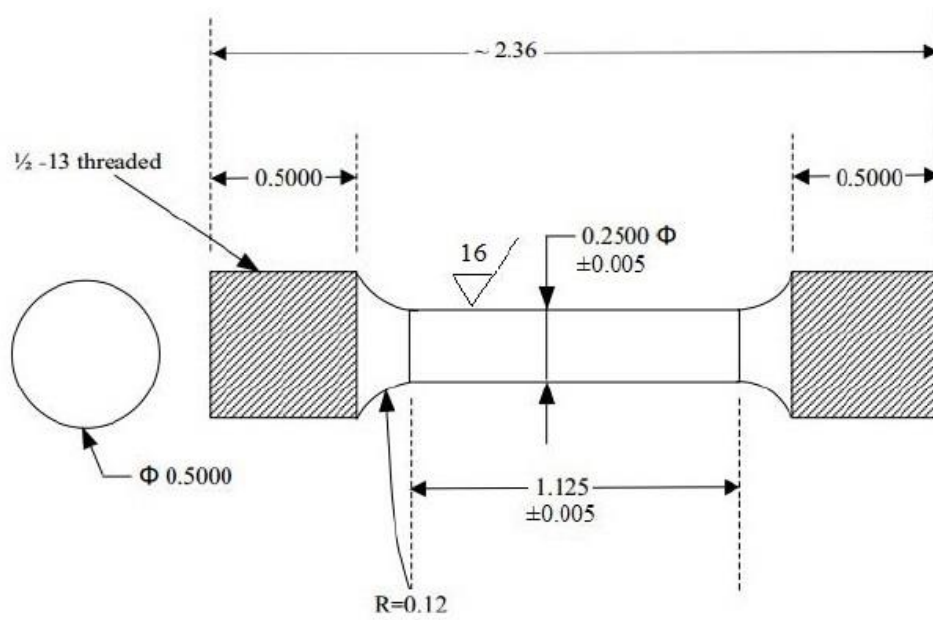


Figure 3.2 Drawing of tensile bar used for tensile test

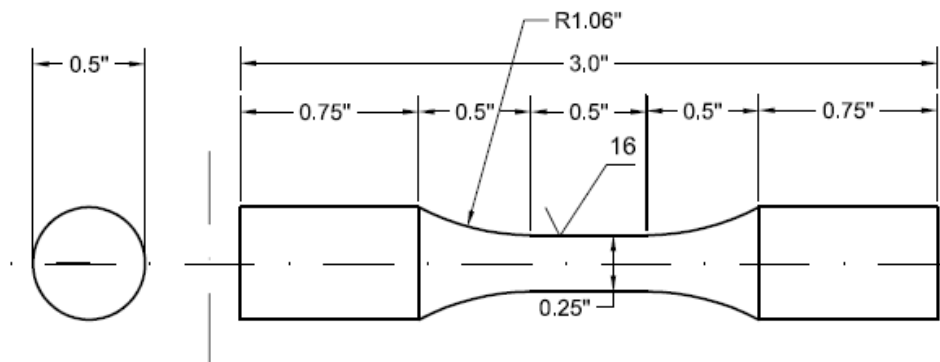


Figure 3.3 Drawing of fatigue bar used for fatigue test

## **CHAPTER 4**

### **EFFECTS OF POWDER PROCESSING AND SINTERING ON TENSILE DUCTILITY OF PM Ti-6Al-4V ALLOY MADE BY HYDROGEN SINTERING OF TITANIUM HYDRIDE POWDERS**

Published as :

P. Kumar, K.S. Ravi Chandran, F. Cao, P. Sun, M. Koopman, and Z. Zak Fang

Effects of powder processing and sintering on tensile ductility of PM Ti-6Al-4V alloy  
made by hydrogen sintering of titanium hydride powders

Proceeding of 13<sup>th</sup> world conference on titanium, 2016, pp. 1355-1359

Reproduced with permission from TMS (The Minerals, Metals & Materials)

## EFFECTS OF POWDER PROCESSING AND SINTERING ON TENSILE DUCTILITY OF PM Ti-6Al-4V ALLOY MADE BY HYDROGEN SINTERING OF TITANIUM HYDRIDE POWDERS

P. Kumar<sup>1</sup>, K.S. Ravi Chandran<sup>1</sup>, F. Cao<sup>1</sup>, P. Sun<sup>1</sup>, M. Koopman<sup>1</sup> and Z. Zak Fang<sup>1</sup>

<sup>1</sup>Department of Metallurgical Engineering, University of Utah, Salt Lake City, Utah, 84112, USA

Keywords: Ti-6Al-4V, Powder metallurgy, Titanium hydride, Hydrogen sintering

### Abstract

Powder metallurgical (PM) titanium alloys made by dehydrogenation of titanium hydride (TiH<sub>2</sub>) have drawn attention due to the lower cost and excellent mechanical properties. In this work, tensile properties of Ti-6Al-4V alloy fabricated by the hydrogen sintering and phase transformation (HSPT) process were investigated. The effects of powder processing and sintering on the tensile properties of Ti-6Al-4V have been studied. It is found that the increase in TiH<sub>2</sub> powder milling time reduces the ductility due to increased oxygen levels. An increase in sintering time enhances the ductility of the material, due to a reduction in pore size, without significantly changing the yield strength and the ultimate tensile strength (UTS).

### Introduction

Powder metallurgy (PM) offers a cost effective approach to produce titanium alloys in near net shape [1, 2]. Conventionally, two general processes have been followed to fabricate PM titanium alloys: Blended Elements (BE) and the Pre-Alloyed (PA) methods [3, 4]. Cost considerations, however, favors BE over PA method [5]. BE titanium alloy products are typically characterized by a significant amount of residual porosity. In general, porosity adversely affects the mechanical properties in PM titanium. Porosity acts as stress concentration sites and, at the same time, reduces the load bearing area, which leads to decrease in both the tensile strength and ductility of the material [6, 7]. Pores also have a greater effect in reducing the fatigue life of PM titanium [8]. In order to improve the mechanical properties, porosity needs to be reduced or eliminated. Fujita et al. [9] showed that a density level > 99% of theoretical density can be achieved by vacuum sintering of titanium sponge fines or hydride-dehydride (HDH) titanium powder. Liu et al. [10] have shown that addition of the rare earth element to PM Ti alloy increases the densification and reduce the porosity through enhanced particle bonding. Such steps to reduce the porosity, therefore, increase the processing cost and, in some instances, can change alloy chemistry significantly.

It is now well accepted that the effective densification and therefore improvement in mechanical properties of titanium alloys can be achieved through the use of TiH<sub>2</sub> powder [11]. Ivasishin et al. [12], in their study on PM Ti-6Al-4V alloy, showed that vacuum sintering of TiH<sub>2</sub> powder with Al-V master alloy powder increases the tensile strength and the ductility. The improvement in the tensile properties was attributed to the higher density levels of Ti-6Al-4V alloy sintered through this process. It was suggested that the continuously evolving hydrogen during sintering of TiH<sub>2</sub> cleaned the particle surface thereby increasing sinterability of titanium [13]. Although, the PM titanium alloys can be easily fabricated from TiH<sub>2</sub>, the microstructures resulting from the vacuum sintering process are relatively coarse. Large lamellar alpha colony microstructure has been observed in vacuum sintered Ti-6Al-4V based on TiH<sub>2</sub> [12]. This type of microstructure limits

tensile ductility, strength and the fatigue life of the titanium alloy [14]. Post-sintering mechanical working and/or heat treatment can be applied to refine the microstructure to improve the properties, especially the fatigue properties [14]. However, the additional steps complicate the processing and increase the process cost.

It is also known that the hydrogen as a temporary alloying element [15, 16] refines the microstructure of Ti alloys. Based on this, a process [17] has been developed to produce fully dense Ti-6Al-4V alloy with refined microstructure. This method is named as hydrogen sintering and phase transformation (HSPT) process. In this process, first, sintering of TiH<sub>2</sub> compact under controlled hydrogen atmosphere in  $\beta$ -phase region is performed and then the sintered compact is subjected to eutectoid transformation and dehydrogenation. This produces relatively fine  $\alpha$ + $\beta$  microstructure. Sun et al. [18] compared the tensile properties of vacuum sintered and HSPT processed CP-titanium. They showed that the tensile strength and the ductility of CP-Ti can be increased by ~ 100 MPa and ~ 4%, respectively, using the HSPT process. Significant increase in the tensile strength and the ductility have also been observed in HSPT processed Ti-6Al-4V [19]. These improvements in tensile properties are attributed to a very fine and uniform microstructure resulting from the precipitation of fine  $\alpha_2$  phases and the formation of ultra-fine ( $\alpha$  +  $\delta$ ) phases in the eutectoid transformation during cooling in hydrogen atmosphere [20].

It is known that the processing variables such as the starting powder size, as well as the sintering temperature and time have significant effect on the density and consequently on the tensile properties of PM titanium alloys. It is therefore of interest to study the effect of these parameter on the tensile properties of Ti-6Al-4V processed by HSPT.

The present investigation is aimed at investigating the effect of TiH<sub>2</sub> particle size and sintering time on the tensile properties of HSPT processed Ti-6Al-4V. Different combinations of powder size and sintering time have been attempted for fabricating the alloy and their effects on tensile properties have been investigated.

### Experimental Procedure

The present study was carried out using the as-received -20/+60 mesh TiH<sub>2</sub> and -400 mesh 60 wt.% Al - 40 wt.% V master alloy powder from Reading alloy, PA, USA. The TiH<sub>2</sub> powder was jar milled using stainless steel balls as grinding media for 30 min. in Ar atmosphere. Using appropriate sieves, -325, -500 and -635 mesh sized powders were produced by milling. Additional -325 mesh size TiH<sub>2</sub> powders were also obtained from the powders milled for 60 min. The milled TiH<sub>2</sub> powders were blended with -400 mesh Al-V master alloy in suitable proportions to obtain the Ti-6Al-4V composition. The blended powders were then cold isostatic pressed (CIPed) at 350 MPa into cylinders of 13 mm in diameter and 90 mm in length. The compacted cylinders were

then heated to 1200°C at a rate of 10°C/min in flowing H<sub>2</sub>/Ar (50/50) gas mixture for sintering. Two sintering times, 4 hrs and 8 hrs, were used in the present study. The sintered samples were then cooled to 650°C at a rate of 5°C/min and held at that temperature for 4 hrs in flowing H<sub>2</sub>/Ar mixture. This produces ultra-fine microstructure with  $\beta + \alpha_2 + \alpha + \delta$  phases, where  $\delta$  is the hydride phase. The samples were then subjected for dehydrogenation at 750°C for 12 hrs. Densities of the samples were determined using a Micromeritics pycnometer model AccuPycII. The average Al, V, and C composition of the dehydrogenated alloy were determined at Aston Metallurgical Laboratory, IL, USA. Oxygen, hydrogen, and nitrogen compositions were determined using Leco TCH 600 analyzer. Samples were mechanically polished followed by fine polishing with colloidal silica. Etching was done using Kroll's reagent to reveal the microstructure. The image analysis software imageJ was used to determine the pore fractions in the microstructure. Tensile samples were machined from the dehydrogenated Ti-6Al-4V bar following the ASTM E-8 standard. A strain rate of 0.002s<sup>-1</sup> was used to perform the tensile tests at room temperature. Displacements in the gauge section of the tensile specimen were recorded as a function of load using an extensometer. Fracture surfaces were examined in a Scanning Electron Microscope (SEM).

### Results and Discussion

The average chemical composition of HSPT Ti-6Al-4V alloys made in this work is given in table I.

Table I. Chemical composition of HSPT processed Ti-6Al-4V

Composition	Al	V	H	C	N	Ti
Wt. %	5.99	3.84	<0.001	<0.03	0.02	Balance

The effect of TiH<sub>2</sub> particle size on density and oxygen content is shown in Table II. It can be seen that the sintered density increases with a decrease in the TiH<sub>2</sub> particle size. This increase in density can be attributed to the increase in sintering kinetics [21] at small particle sizes. In addition, a larger particle size creates large interstitial pores during the cold compaction process which eventually leads to large and non-uniform pores in the sintered materials.

Table II. Effect of TiH<sub>2</sub> particle size on the density and oxygen content on HSPT processed Ti-6Al-4V

TiH <sub>2</sub> particle size, mesh size	Relative density, %	Oxygen, wt. %
-325 (<45μm)	97.78	0.23
-500 (<25μm)	99.15	0.45
-635 (<20μm)	99.33	0.42

Although, a finer particle size helps in increasing the density, it is more susceptible to oxygen contamination during milling due to increased surface area. Oxygen in Ti-6Al-4V is known to have detrimental effect on tensile properties which will be discussed later. It is clear that there is a trade-off between high density and the oxygen contamination using fine TiH<sub>2</sub> powder.

Figure 1 shows the optical microstructures of the HSPT processed Ti-6Al-4V alloy. The distribution of pores in the microstructure and the prior  $\beta$  grain structure can be observed. The high magnification micrograph shown in Fig 1(d) reveals the

transformed  $\beta$  structure. The microstructure can be characterized as a fine  $\alpha + \beta$  microstructure with grain boundary (GB  $\alpha$ ) phase

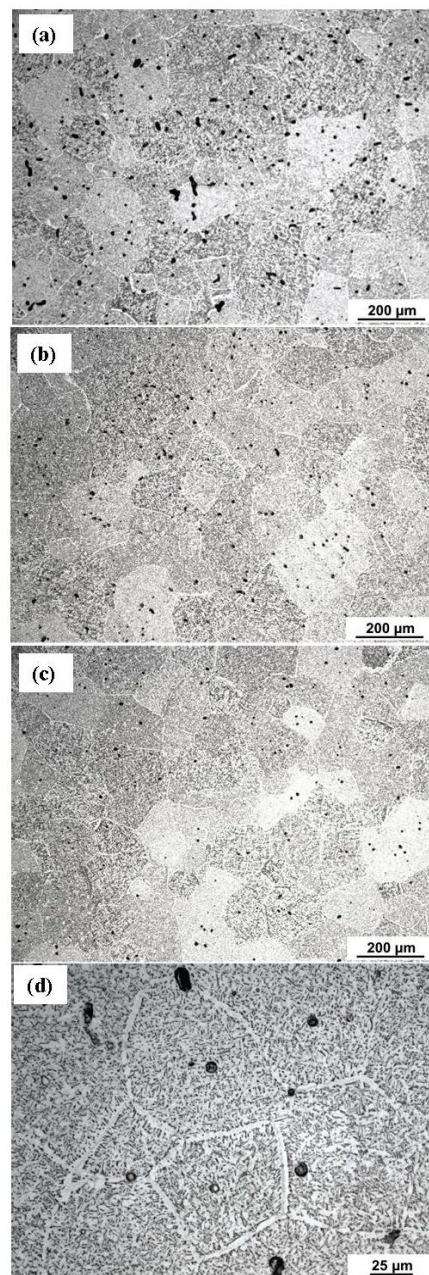


Figure 1. Optical microstructure of HSPT Ti-6Al-4V (a) -325 mesh sintered for 4 hrs (b) -500 mesh sintered for 4 hrs and (c) -635 mesh sintered for 4 hrs (d) same material as (a) at high mag.



with uniformly distributed pores. Fig. 1 (a), (b) and (c) illustrate the microstructures of the processed Ti-6Al-4V, using -325, -500 and -635 mesh TiH<sub>2</sub> powder sintered for 4 hrs, respectively. Elongated pores along with a few rounded were observed in the -325 material. The average volume fraction of pores is  $\sim 0.0013$ . Figure 1(b) indicates a significant decrease in porosity, as TiH<sub>2</sub> particle size was reduced to -500 mesh size. Isolated small round pores were observed in the microstructure. The average volume fraction of pores is  $\sim 0.00035$ . The volume fraction of pores further decreased to  $\sim 0.0002$  when a much finer -635 mesh TiH<sub>2</sub> was used. Therefore, it is clear that with the use of finer TiH<sub>2</sub> particles, high densification of HSPT PM Ti-6Al-4V alloy during sintering can be achieved.

Tensile stress-strain curves of the HSPT Ti-6Al-4V alloy samples fabricated using the three different TiH<sub>2</sub> particle size are shown in Fig. 2. It is to be noted that except for particle size difference, all the samples were processed identically (4 hrs of sintering). Table III summarizes the tensile properties of the samples. Yield strength (YS) increased from 961 MPa to 1173 MPa and the %elongation decreased from  $\sim 13\%$  to  $\sim 4\%$  as the initial TiH<sub>2</sub> particle size was reduced from -325 to -500 mesh. Also from Table II, the oxygen content increased to  $\sim 0.42$  wt.% for -500 mesh TiH<sub>2</sub> from a level  $\sim 0.23$  wt.% for -325 mesh. Therefore, the increase in the tensile strength and reduction in ductility of the sample can be attributed to the oxygen contamination. It is known that strength and ductility of Ti-6Al-4V are strongly dependent on the oxygen [22]. Oh et al. [23] showed that the dependence of tensile properties of Ti-6Al-4V alloy on oxygen is related to the lattice staining by oxygen. Lattice strain acts as a barrier for the dislocation motion, therefore increased hardening and reduced ductility of Ti-6Al-4V can be explained on this basis.

The study also evaluated the effect of sintering time, for a given initial TiH<sub>2</sub> powder size distribution, on the tensile stress-strain behavior. Figure 3 shows the microstructure of HSPT processed Ti-6Al-4V based on -325 mesh TiH<sub>2</sub> powder and 8 hrs sintering. A reduction in the amount of elongated pores was observed as compared to the material made of -325 mesh powder sintered for 4 hrs (Fig.1a). The average volume fractions of porosity were  $\sim 0.0013$  and  $\sim 0.0010$  in -325 samples, sintered for 4 hrs and 8 hrs respectively. This clearly indicates that there is not significant change in porosity even after doubling the sintering time. Therefore, it can be said that sintering of Ti-6Al-4V is nearly complete around 4 hrs of sintering time. This is also supported by the fact that the only a slight increase in density has been observed ( $\sim 97.78\%$  for 4 hrs sintered specimen versus  $\sim 98.16\%$  for 8 hrs sintered specimen).

The stress-strain curves for HSPT Ti-6Al-4V alloy sintered for 4 hrs and 8 hrs are shown in Fig 4. It can be clearly seen that elongation increased slightly from  $\sim 14\%$  to  $\sim 15\%$  as the sintering time increased from 4 hrs to 8 hrs. There is no measurable change in YS and UTS with the increase in the sintering time. The slight increase in elongation in 8 hrs sintered sample can be attributed to the reduction in the elongated pores in the sample. This is consistent with the fact [7] that pores act as strain concentration sites and leads to the reduction in overall elongation of the sample. Fracture surface analysis (Fig 5.) also indicated that localized deformation occurs around the pores. It can be seen that such pores are slightly large in volume fraction in 4 hrs sintered sample compared to that in 8 hrs sintered. Therefore

Table III. Tensile properties of HSPT Ti-6Al-4V samples

TiH <sub>2</sub> particle size, mesh size	$\sigma_{YS}$ , MPa	$\sigma_{UTS}$ , MPa	% El.
-325 ( $<45\mu\text{m}$ )	961	1027	13.76
-500 ( $<25\mu\text{m}$ )	1173	1214	4.20
-635 ( $<20\mu\text{m}$ )	1148	1187	2.26

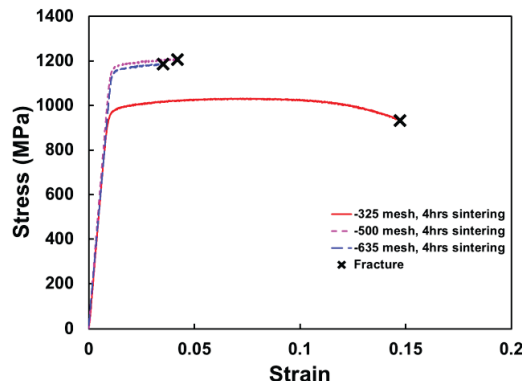


Figure 2. Stress and Strain curves of HSPT processed Ti-6Al-4V

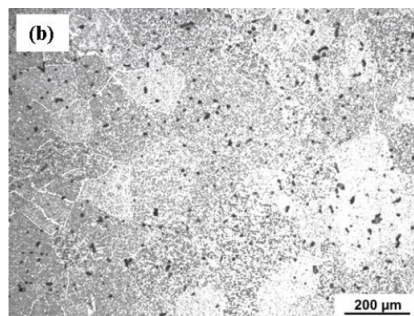


Figure 3. Optical microstructure of HSPT Ti-6Al-4V based on -325 mesh TiH<sub>2</sub> sintered for 8 hrs

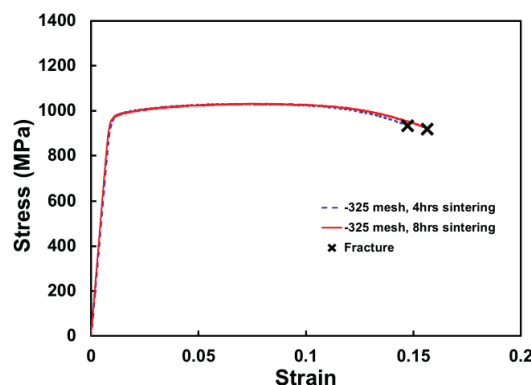


Figure 4. Stress and Strain curves of HSPT processed Ti-6Al-4V 4 hrs sintered sample compared to that in 8 hrs sintered.



the ductility of HSPT Ti-6Al-4V can be increased by reducing the overall volume fraction of pores using long sintering times.

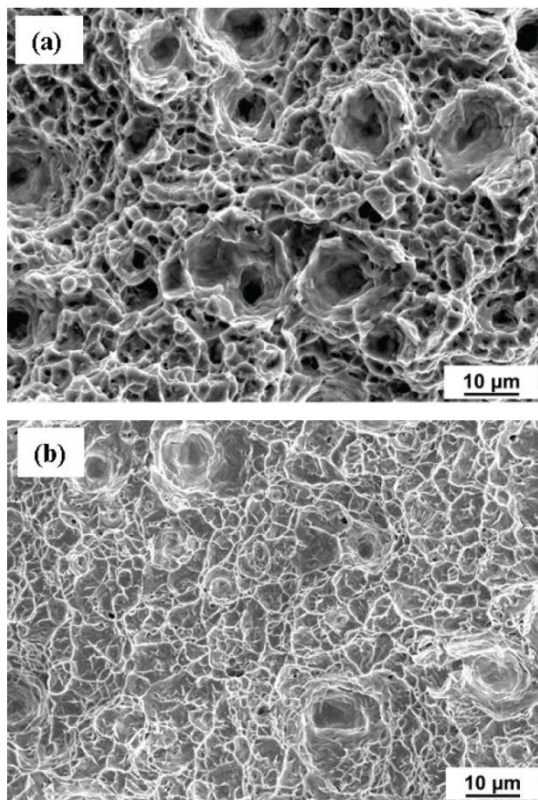


Figure 5. SEM fractograph of (a) 4 hrs (b) 8 hrs sintered HSPT Ti-6Al-4V based on -325 mesh size Ti-6Al-4V.

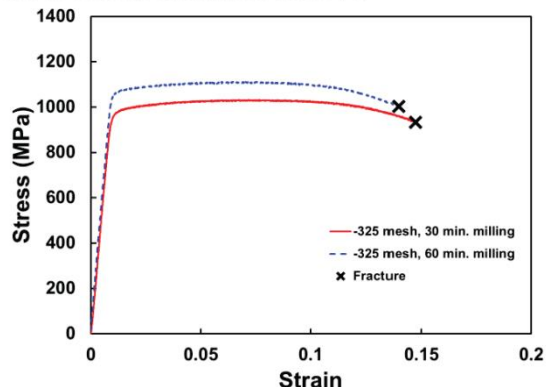


Figure 6. Stress and Strain curves of HSPT processed Ti-6Al-4V

During this work, it has also been observed that milling time also affects the tensile properties of HSPT Ti-6Al-4V. Figure 6 shows the stress-strain curve of HSPT Ti-6Al-4V alloy sintered using -

325 TiH<sub>2</sub> powder obtained by milling -20/+60 mesh TiH<sub>2</sub> powder for 30 min. and 60 min. A significant change in the stress-strain response can be observed in the Fig. 6. The YS and UTS increased by ~100 MPa while elongation decreased from ~14% to ~12% when the milling time increased from 30 min. to 60 min. Oxygen content increased to ~0.28 wt.% for 60 min. milling from ~0.23 wt.% for 30 min. milling. A longer milling causes a reduction in TiH<sub>2</sub> particle size. Even though both sample used -325 TiH<sub>2</sub> from 30 min. and 60 min. milled powder, a larger fraction of fine powder will be found in 60 min. milled TiH<sub>2</sub> powder than that was milled for 30 min. Smaller particle having large surface area are more prone to oxygen contamination. Therefore, the increased tensile strength and reduced ductility in 60 min. milled sample possibly arises from the oxygen contamination during milling.

### Conclusion

This study examined the effect of powder processing including the powder size, milling time and sintering time on tensile properties PM Ti-6Al-4V. The analysis of the result led to the following conclusions.

1. Hydrogen sintering and phase transformation (HSPT) process based on TiH<sub>2</sub> is a viable technique to produce Ti-6Al-4V having tensile properties that are close to that of the wrought Ti-6Al-4V. In particular, the strength levels are either equivalent or higher than that is typically found in wrought alloys.
2. Alloys with relatively higher densities, approaching that of the wrought alloy can be achieved by using a finer starting powder of TiH<sub>2</sub>. The largest effect on the final density is due to the initial powder size distribution used for the preparation of the alloys.
3. At smaller particle sizes, oxygen contamination during powder processing, although leads to increased tensile strength, reduces ductility severely in PM Ti-6Al-4V. Therefore, there is optimal milling time for powder size reduction that would produce acceptable levels of strength and ductility.
4. For a given powder size, an increase in sintering time from 4 hrs to 8 hrs reduces the residual porosity slightly, which leads to a slight increase in the ductility of PM Ti-6Al-4V. This suggests sintering for durations longer than 4 hrs do not increase the ductility appreciably.

### Acknowledgments

The authors duly acknowledge financial grant from the U.S. Department of Energy, Innovative Manufacturing Initiative (DEEE0005761), through the Advanced Manufacturing and the Office of Energy Efficiency and Renewable Energy. We also thank to James Paramore for assistance with respect to assembling the hydrogen sintering furnace.

### Reference

1. F. H. Froes and D. Eylon, "Powder -Metallurgy Of Titanium Alloys", International Materials Reviews, 35 (1990), 162-182.

2. F.H. Froes, S.J. Mashl, V.S. Moxson, J.C. Hebeisen and V A Duz, "The Technologies of Titanium Powder Metallurgy" *Journal of Metals*, 56 (2004), 46-48.
3. F.H. Froes, D. Eylon, G. E. Eichelmann and H. M. Burte, "Developments in Titanium Powder Metallurgy", *Journal of Metals*, 32 (1980), 47-54.
4. V.S. Moxson, O.N. Senkov and F.H. Froes, "Innovation in Titanium Powder Processing", *Journal of Metals*, 2000, 24-26.
5. V.S. Moxson, P. Sjoblom and M.J. Trzcinsk, "Production and Application of Low Cost Titanium powder Product", *International Journal of Powder Metallurgy*, 34 (1998), 45-53.
6. A.M. Gokhale, and G. R. patel, "Origins of variability in the fracture-related mechanical properties of a tilt-pour-permanent-mold cast Al-alloy" *Scripta Materialia*, 52 (2005), 237-241.
7. R.J. Bourcier, D.A.Koss, R.E. Smelser and O. Richmond, "The influence of porosity on the deformation and fracture of alloys", *Acta Metallurgica*, 34(1986), 2443-2453.
8. Y. Yan, G.L. Nash and P. Nash, "Effect of density and pore morphology on Fatigue properties of sintered Ti-6Al-4V" *International Journal of Fatigue*, 55 (2013), 81-91.
9. T. Fujita, A. Ogawa, C. Ouchi and H. Tajima, "Microstructure and properties of titanium alloy produced in newly developed blended elemental powder metallurgy process", *Material Science & Engineering A* 213 (1996), 148-153.
10. Y. Liu, L.F. Chen, H.P. Tang, C.T. Liu, B. Liu and B.Y.Huang, "Design of powder metallurgy titanium alloys and composites *Material Science & Engineering, A* 418 (2006), 25-35.
11. V. V. Joshi, C. Lavender, V. Moxon, V. Duz, E. Nyberg and K.S. Weil, "Development of Ti-6Al-4V and Ti-1Al-8V-5Fe alloys using Low-cost TiH<sub>2</sub> Powder Feedstock", *Journal of Materials Engineering and Performance*, 22 (2013), 995-1003.
12. O.M. Ivasishin, D.G. Savvakina, F.Froes, V.C. Mokson and K.A. Bondareva, "Synthesis of Alloy Ti-6Al-4V with low residual Porosity by a powder metallurgy method", *Powder Metallurgy and Metal Ceramics*, 41 (2002), 382-390.
13. O.M. Ivasishin, D.G. Savvakina, M.M. Gumenyak and O.B. Bondarchuk, "Role of Surface Contamination in titanium PM", *Key Engineering Materials*, 520(2012), 121-132.
14. M. Hagiwara, Y. Kaieda, Y. Kawabe, S. Miura, "Fatigue Property Enhancement of Elemental P/M Approach" *Iron and Steel Institute of Japan International*, 31 (1991), 922-930.
15. W.R. Kerr, "The Effect of Hydrogen as a Temporary Alloying Element on the Microstructure and Tensile Properties of Ti-6Al-4V", *Metallurgical Transaction, A* 16 (1985), 1077-1087.
16. F.H. Froes, O.N. Senkov and J.I. Qazi, "Hydrogen as a temporary alloying element in titanium alloys: thermohydrogen processing", *International Materials Reviews*, 49 (2004), 227.
17. Z. Z Fang, P. Sun, H. Wang, "Hydrogen Sintering of Titanium to produce High Density Fine Grain Titanium Alloys", *Advanced Engineering Materials*, 14 (2012), 1-5.
18. P. Sun, Z.Z. Fang, M. Koopman, "Comparison of Hydrogen sintering and Phase Transformation (HSPT) processing with Vacuum Sintering of CP- Ti" *Advanced Engineering Materials*, 15 (2013), 1007-1013.
19. J.D. Paramore, Z.Z. Fang and P. Sun, "Hydrogen sintering of titanium and its alloys", *Titanium Powder Metallurgy*, ed. M. Qian and F.H. Froes, 163-182.
20. P. Sun, Z. Z. Fang, M. Koopman, Yang Xia, J. Paramore, K. S. Ravi Chandran, Y. Ren and J. Lu, "Phase Transformations and Formation of Ultra-fine Microstructure during Hydrogen Sintering and Phase Transformation (HSPT) Processing of Ti-6Al-4V, unpublished.
21. P.S. Kisliy et al., "Effect of particle size of powders on the sintering kinetics of titanium boride", *Physics of Sintering*. 4(2) (1972), 107-118.
22. Y Itoh, T Uematsu, K. Sato and H. Miura, " Effect of Oxygen Content and Relative density on Tensile Properties of Injection Molded Ti-6Al-4V alloy", *Journal of Japan Society Powder Metallurgy* 56 (2008), 259-263.
23. J.-M. Oh, B.-G. Lee, S.-W. Cho, S.-W. Lee, G.-S. Choi, and J.-W. Lim, "Oxygen Effects on the Mechanical Properties and Lattice Strain of Ti and Ti-6Al-4V", *Metals and Materials International*, 17 (2011), 733-736.

## **CHAPTER 5**

### **THE NATURE OF TENSILE DUCTILITY AS CONTROLLED BY EXTREME-SIZED PORES IN POWDER METALLURGY Ti-6Al-4V ALLOY**

Published as:

P. Kumar, K.S. Ravi Chandran, , F. Cao, M. Koopman and Z. Zak Fang

The Nature of Tensile Ductility as Controlled by Extreme-sized Pores in Powder

Metallurgy Ti-6Al-4V alloy

Metallurgical and Materials Transitions A, 2016, volume 47, issue 5, pp 2150-2161.

Reproduced by permission of Springer.

# The Nature of Tensile Ductility as Controlled by Extreme-Sized Pores in Powder Metallurgy Ti-6Al-4V Alloy



P. KUMAR, K.S. RAVI CHANDRAN, F. CAO, M. KOOPMAN, and Z. ZAK FANG

Tensile properties of Ti-6Al-4V titanium alloy, sintered by a new process (sintering, phase transformation, and dehydrogenation of titanium hydride compacts, termed HSPT process), were investigated to determine how the sintering pores influence the tensile strength and ductility. It was found that the ductility in the sintered alloy is severely affected by the size of the largest pore, referred here as extreme-sized pore, even when the average volume fraction of porosity is nearly constant between a large number of samples. It is shown that the rapid decrease in ductility, with an increase in the extreme pore size, is caused by strain localization around the extreme-sized pore and early crack initiation. This crack initiation leads to fracture of the plane containing the pore thereby limiting the extent of uniform plastic strain that can be attained before fracture. Interestingly, the strength properties are, however, found to be independent of the size of the extreme-sized pore. The results are explained on the basis of stress concentration and strain localization around the extreme-sized pores. The work also reveals that if the extreme-sized pores are eliminated, PM Ti-6Al-4V alloy with high strength (~1100 MPa) and good ductility (~12 pct), which is easily comparable to a wrought Ti-6Al-4V alloy, can be achieved even at oxygen levels up to 0.4 wt pct.

DOI: 10.1007/s11661-016-3419-5

© The Minerals, Metals & Materials Society and ASM International 2016

## I. INTRODUCTION

THE prospect of achieving high density, strength, and toughness while at the same time facilitating near-net shape manufacturing has largely drawn focus on powder metallurgical (PM) titanium alloy processing research and development.<sup>[1,2]</sup> Research in the past<sup>[1–5]</sup> focused on PM titanium alloys made by two kinds of processes: the blended element (BE) powder process and the pre-alloyed (PA) powder process. It is now common<sup>[3,4]</sup> that densities approaching the theoretical density can be achieved by proper control of powder and the processing parameters. Tensile ductility of PM titanium alloys is very sensitive to porosity but there is not much quantitative work in this area. Caceres<sup>[5]</sup> in the study on Al-Si-Mg alloy, has shown that small amounts of residual pores can lead to crack initiation and reduce the tensile ductility. It is necessary to eliminate large pores and produce nearly fully dense products consistently if PM-processed materials are to compete reliably with wrought materials. Major efforts have been made in the past to improve the tensile properties of BE titanium alloys. Liu *et al.*<sup>[6]</sup> showed that the addition of rare earth elements enhances the

particle bonding during sintering, resulting in reduced porosity and leading to an improvement in ductility. Secondary processing, such as hot forging and heat treatment, also improves mechanical properties of BE titanium alloys, largely due to pore closure and refined microstructure.<sup>[6,7]</sup> However, additional processing steps beyond PM sintering increase the complication in processing and cost of the alloy, thus weakening the prospect for commercial success.

In recent years, vacuum sintering and dehydrogenation of TiH<sub>2</sub> powder has emerged as an attractive technique to produce titanium alloys with a relatively low amount of porosity. Studies<sup>[8–10]</sup> have shown that improved sinterability, low porosity, and better mechanical properties can be achieved by this approach. The reduced porosity level in the sintered product has been attributed partly to the hydrogen cleaning of the particle surfaces, during egress, which apparently leads to better sintering.<sup>[11]</sup> However, the achievable tensile properties of titanium alloys are limited by the coarse microstructure obtained in vacuum sintering of TiH<sub>2</sub>.

It is known from the literature that phase transformation of hydrogenated titanium alloys refines and modifies the microstructure of both wrought<sup>[12,13]</sup> and sintered PM titanium alloys<sup>[14–16]</sup> leading to improved mechanical properties. This process was either referred as “thermo-hydrogen processing (THP)” or the “Hydrovac” process at that time. A method<sup>[17]</sup> has been recently proposed to produce fully densified PM titanium alloy with a refined  $\alpha + \beta$  microstructure by sintering and dehydrogenation of titanium hydride powders. This recent process, named “hydrogen

P. KUMAR and F. CAO, Ph.D. Candidates, K.S. RAVI CHANDRAN and Z. ZAK FANG, Professors, and M. KOOPMAN, Research Professor, are with the Department of Metallurgical Engineering, University of Utah, Salt Lake City, UT 84112. Contact e-mail: ravi.chandran@utah.edu

Manuscript submitted July 23, 2015.

Article published online March 4, 2016

sintering and phase transformation (HSPT) process, first uses a hydrogen atmosphere to sinter the cold-pressed  $\text{TiH}_2$  powder compact in the beta phase region. The sintered material is then eutectoid-transformed to achieve a fine scale microstructure. Subsequently, the compact is dehydrogenated, leading to a fine transformed  $\alpha + \beta$  microstructure.

Although the bulk density of titanium alloys sintered from  $\text{TiH}_2$  is generally high (>98 pct), there are some residual pores that are randomly distributed in the sintered material. Several studies have shown that porosity has a remarkable effect on tensile ductility of metallic materials.<sup>[6,18–23]</sup> For example, Shore *et al.*<sup>[24]</sup> have shown that the tensile ductility in Al welds decreases from 15 to 10 pct when the porosity increases from 0 to 5 pct. On the other hand, Surappa *et al.*<sup>[25]</sup> have shown that the tensile strength and the ductility are affected by the size of pores on the fracture surface and not by the volume fraction of pores. Regardless, the large reduction in ductility at relatively low porosity levels is a serious problem and has not been clearly explained in any material.

In the present work, we have systematically studied how the residual porosity at low volume fraction affects the tensile properties of HSPT-processed PM Ti-6Al-4V alloy. The pore size distribution and pore morphology have been quantified through extensive quantitative microscopy. The primary objective was to establish how the tensile strength and ductility of the HSPT-sintered Ti-6Al-4V alloy are affected by the sizes of extreme-sized pores. The results are very interesting in that, even though each sample had nearly similar volume fraction of porosity, a strong correlation has been found to exist between extreme pore size and tensile ductility. A mechanistic explanation is presented as to how the extreme-sized pores strongly affect the tensile ductility,

while not having any discernible impact on yield or tensile strength.

## II. EXPERIMENTAL PROCEDURE

PM Ti-6Al-4V alloy samples with a fine scale  $\alpha + \beta$  microstructure were made by PM through a series of steps of the HSPT process:<sup>[17,26–28]</sup> pressureless sintering, eutectoid transformation, and dehydrogenation. A schematic of the processing steps is presented in Figure 1. First,  $\text{TiH}_2$  powder (–325 mesh) was blended with the required proportion of (–325 mesh) Al-V master alloy powder to yield the nominal Ti-6Al-4V alloy composition. The blended powders were then cold isostatically pressed (CIPed) at a pressure of 350 MPa into cylinders of 13 mm in diameter and 90 mm in length. The pressed samples were then heated to 1473 K (1200 °C) at a rate of 10 K/min followed by sintering at that temperature for 4 hours in a flowing Ar/ $\text{H}_2$  mixture. The sintered  $\text{TiH}_2$  compacts were then cooled at a rate of 5 K/min to 923 K (650 °C) this temperature is below the eutectoid transformation temperature [1123 K (850 °C)] of the (Ti-6Al-4V)-H system. The samples were subsequently held at 923 K (650 °C) for 4 hours to complete eutectoid transformation in the material followed by cooling to room temperature. The samples were then dehydrogenated by holding at 1023 K (750 °C) for 12 hours in vacuum.

Chemical compositions of the samples were determined following ASTM E1447 and E1409 at Aston Metallurgical Laboratory, IL, USA. Oxygen, nitrogen, and hydrogen levels were determined using a Leco TCH 600 analyzer. The phases in the microstructure were identified using X-ray diffraction (XRD) in a Philips X'pert diffractometer. Standard metallographic preparation procedures were followed to prepare samples for microscopy. Tensile samples were made following the ASTM E8 standard. The gage sections of the samples were 31.75 mm in length and 6.35 mm in diameter. The tensile tests were performed with a strain rate of  $0.0002 \text{ s}^{-1}$  at room temperature. The deformation of the gage section was recorded using an Epsilon model 3542-0100-050-ST extensometer. Yield and tensile strength values as well as pct elongation were determined from the stress-strain curves. The values of the strain hardening exponent ( $n$ ) were determined by fitting the true stress-true strain data to the Ludwick equation ( $\sigma = K\varepsilon_p^n$ , where  $\varepsilon_p$  is plastic strain,  $K$  and  $n$  are the hardening parameters). Fracture surfaces were examined in a scanning electron microscope (SEM) to determine the nature of the crack/fracture initiation. The pores, from which tensile fracture initiated, were irregular in shape hence, the projected areas of these pores were determined by using the grid technique and with the aid of imageJ image analysis software.

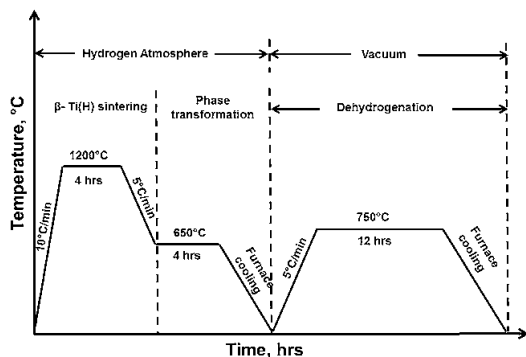


Fig. 1—Schematic of temperature and time profile of the HSPT process used for making PM Ti-6Al-4V alloy.<sup>[17]</sup>

Table I. Chemical Composition of HSPT-Processed Ti-6Al-4V

Composition	Al	V	O	H	C	N	Ti
Wt pct	6.09	4.15	0.43	0.001	<0.03	0.01	balance



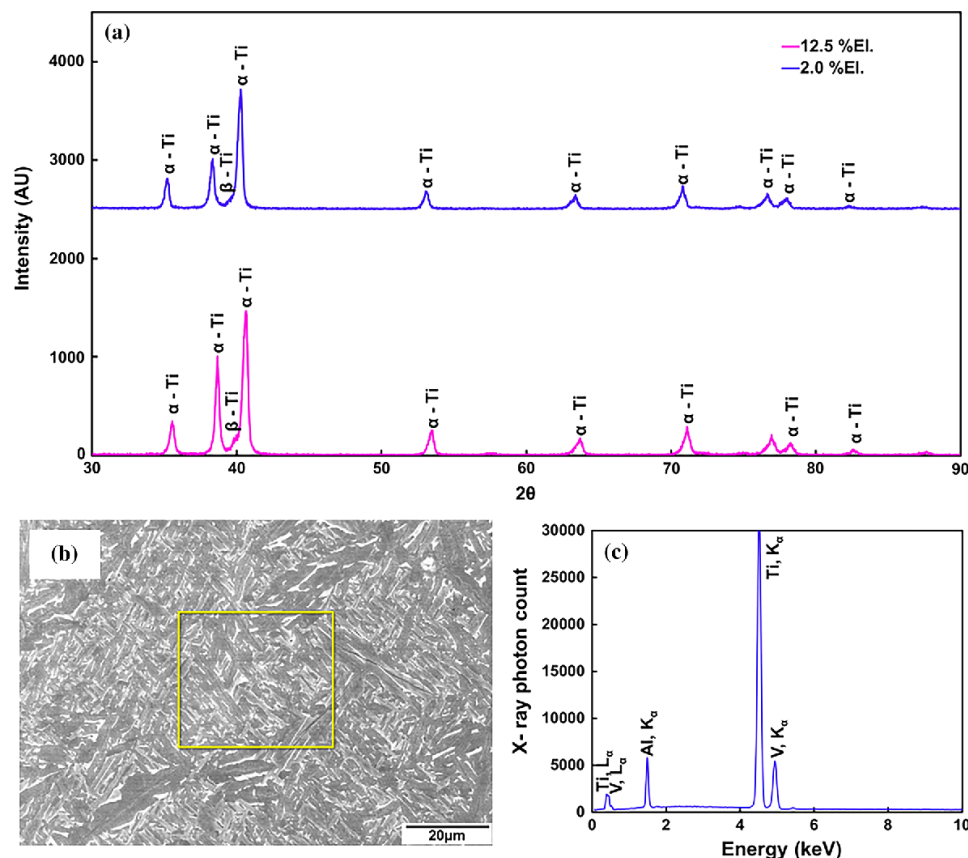


Fig. 2—(a) X-ray diffraction patterns of a low-ductility sample (~2 pct elongation) and a high-ductility (~12.5 pct elongation) sample, (b) SEM micrograph, and (c) the corresponding EDS pattern (Color figure online).

Hereafter, the term “pore size” refers to the diameter (d) of a circular area that is equal to the area of the irregularly shaped pore. This was calculated as 
$$= \sqrt{\text{pore area} \times \frac{4}{\pi}}$$

### III. RESULTS

#### A. Microstructure

The measured densities of the samples after dehydrogenation were found to be in the range of 99.02 to 99.5 pct of the theoretical density. This is equivalent to a porosity of 0.6 to 1.2 pct by volume. The chemical composition of the dehydrogenated samples is given in Table I. The alloy has a slightly elevated oxygen level (~0.43 wt pct) due to the higher level of oxygen in the titanium hydride source powder.

The XRD patterns of the two random samples (one is of low ductility and the other is of high ductility) of the Ti-6Al-4V alloy fabricated in this work are shown in Figure 2(a). The XRD patterns confirm the presence of only α and β phases and no residual TiH<sub>2</sub> in the

microstructure. The similarity of XRD patterns, between the two samples, suggests that the difference in ductility arises from factors other than the phases present in the microstructure. In addition, the EDS analysis of the typical microstructure region (as shown Figures 2(b) and (c)) confirmed that the average composition of the alloy in all the samples was within ASTM alloy specification and that there was no significant difference in chemical/phase composition between the low-ductility and high-ductility samples. Figures 3(a) and (b) show the microstructure after sintering and dehydrogenation. Prior-beta (β) grains and the distribution of pores in the microstructure are seen in Figure 3(a), whereas (b) reveals the transformed α + β structure. The microstructure of the sintered alloy can thus be characterized as a fine-Widmanstätten α + β structure with grain boundary alpha (GB-α) phase. The average prior-beta grain size was found to be ~102 μm. The α phase dimensions were ~2 μm in thickness and ~5 μm in length. Most of the pores in the microstructure were isolated and randomly distributed within prior-β grains and appeared to be relatively small in size (~10 μm or less). The distribution of pore sizes in the

microstructure, as determined by image analysis, is shown as frequency and cumulative distributions in Figures 3(c) and (d), respectively. These distributions are based on measurements over an area of  $31.67 \text{ mm}^2$ . The distribution in Figure 3(c) indicates that the majority of pores are very small; approximately 40 pct of pores are of size  $<5 \mu\text{m}$  and nearly all the pores are  $<20 \mu\text{m}$ . However, a few extreme-sized pores, some as large as  $50 \mu\text{m}$ , were present in the microstructure. In fact, the cumulative distribution (Figure 3(d)) confirms that about 99.8 pct of pores are below  $\sim 20 \mu\text{m}$ . This indicates that extreme-sized pores, with sizes  $> 20 \mu\text{m}$  are very few in number. Quantitative image analysis revealed that the average volume fraction of pores varied in the range of 0.0035 to 0.0094, which roughly agrees with that estimate from density (volume fraction range 0.0064 to 0.012).

### B. Tensile Properties

Figure 4(a) shows the tensile true stress-true strain curves for all the samples (22) tested. The crosses at the end of the curves mark the fracture point. The tensile properties are summarized in Table II. Since all the

samples were processed identically, similar chemical composition and microstructure can be assumed to exist in all the samples. It is interesting to note that the yield and tensile strength, and fracture stress levels are nearly the same (Figures 4(b) and (c)), but there is a large variability in tensile elongation (Figure 4(d)). Figures 4(b) through (d) are plotted in terms of the largest pore size in the fracture plane. In all samples, SEM examination revealed that fracture initiated from a single large pore that was present in the test volume. Generally, it can be expected that each sample will have a largest pore of a unique size in its volume, based on statistical distribution. Thus, the variability in the elongation can be attributed to statistics of occurrence of the largest pore in the sample. In Figure 4(d), the data have been divided into three groups (labeled A, B, and C). Most of the data closely follow the trend of an exponential decrease of pct elongation with respect to the extreme pore size (Group A). However, some data, identified as groups B and C, have different levels of ductility although they seem to follow a similar trend as that of group A. While the group C in the figure (Figure 4(d)) shows the most severe ductility loss, group B indicates the less severe case of ductility with respect to the extreme-sized pore. A

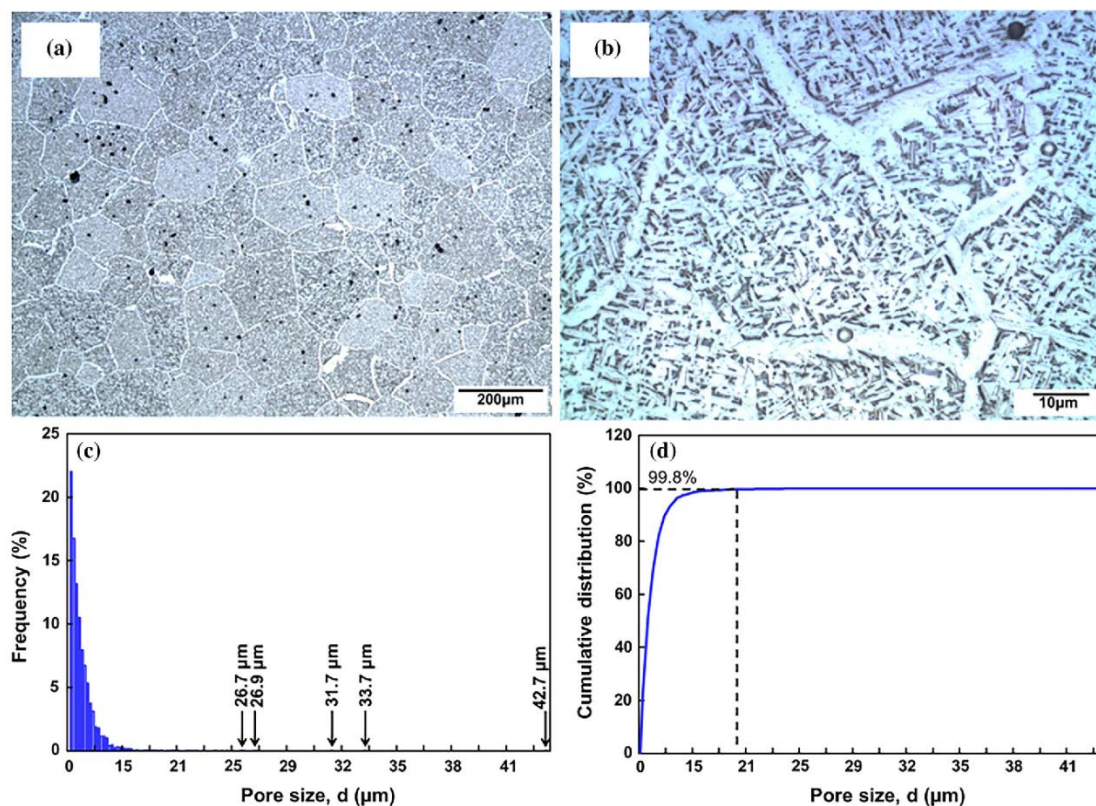


Fig. 3—(a) Optical microstructure showing prior-beta grains (b) structure of matrix and GB- $\alpha$  (c) frequency of occurrence of pore, and (d) cumulative pore distribution of HSPT-processed Ti-6Al-4V. The arrows in (c) indicate the sizes of a few individual extreme-sized pores (Color figure online).

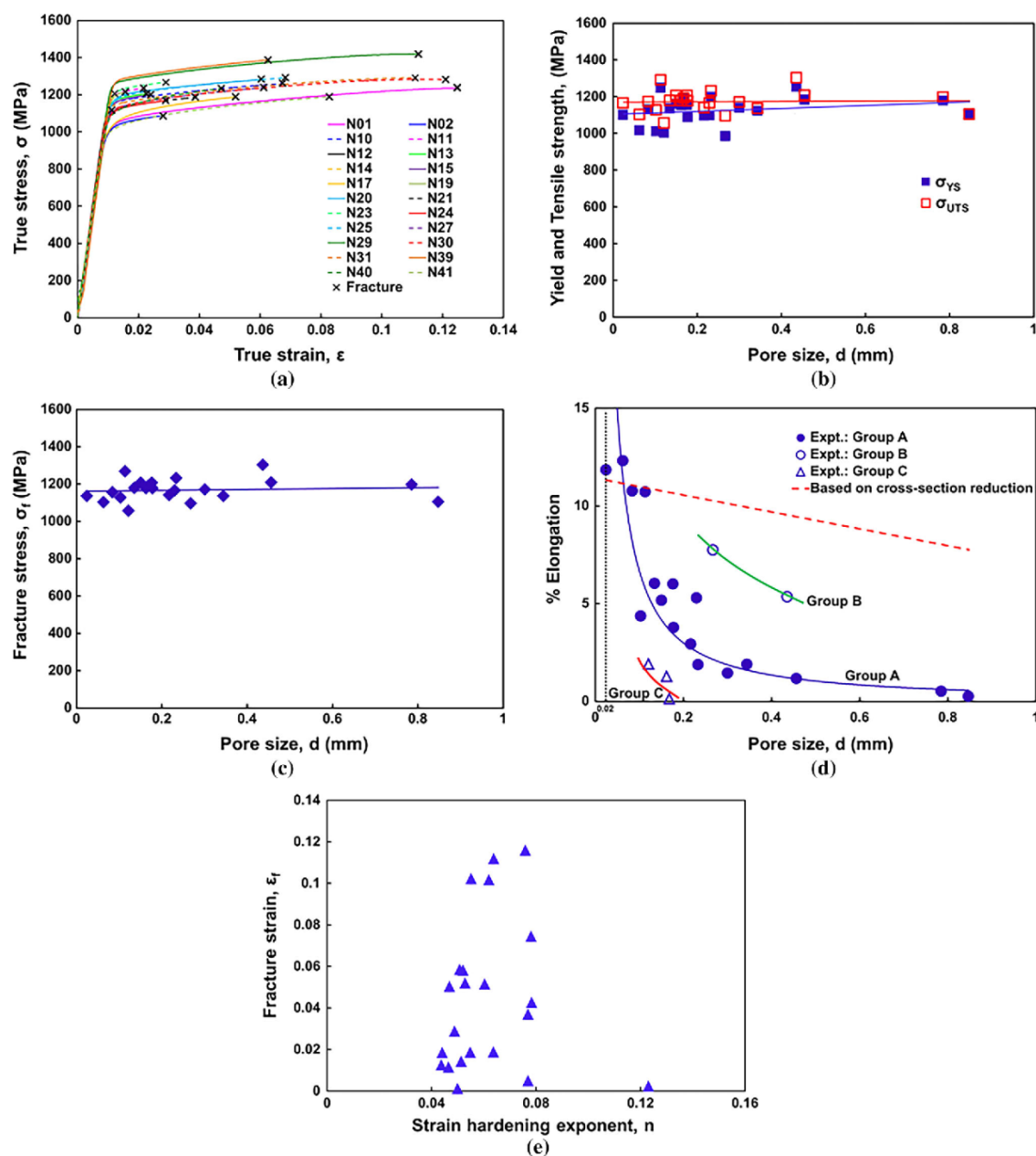


Fig. 4—(a) True stress and true strain curves; (b) through (d) show the variation of yield, ultimate and fracture stress, as well as pct elongation as a function of size of the largest pore from which failure occurred; (e) demonstrates the lack of a correlation between fracture strain and strain hardening (Color figure online).

calculation of the expected decrease in elongation due to reduction in cross section caused by extreme-sized pores was performed, without considering the stress concentration effect. To calculate the elongations, the increased levels of stresses due to reduction in cross section by the presence of extreme-sized pores were calculated. The corresponding elongations at these

stress levels were determined through the examination of an essentially pore-free sample's stress-strain curve (sample N30, Table II). This trend is shown in Figure 4(d) as the dashed line. Figure 4(e) shows that strain hardening exponent 'n' does not correlate with the measured fracture strain. This result supports the idea that the variation in elongation in the present



Table II. Tensile Properties of HSPT-Processed Ti-6Al-4V Samples

Specimen No.	Extreme Pore Size, $d$ (mm)*	Yield Strength, $\sigma_{YS}$ (MPa)	Tensile Strength, $\sigma_{UTS}$ (MPa)	Elongation Pct El	Strain Hardening Exponent, $n$
N01	0.063	1016	1102	12.30	0.076
N02	0.121	1002	1055	1.90	0.064
N10	0.135	1135	1178	6.02	0.050
N11	0.456	1182	1208	1.15	0.046
N12	0.847	1101	1103	0.24	0.123
N13	0.163	1151	1177	1.26	0.044
N14	0.169	1191	1191	0.11	0.050
N15	0.301	1138	1170	1.44	0.051
N17	0.103	1010	1127	4.35	0.078
N19	0.785	1178	1195	0.5	0.077
N20	0.150	1160	1206	5.16	0.047
N21	0.217	1094	1140	2.92	0.049
N23	0.233	1197	1230	1.86	0.044
N24	0.344	1121	1134	1.88	0.055
N25	0.177	1153	1205	5.99	0.052
N27	0.230	1097	1164	5.28	0.060
N29	0.113	1247	1290	10.71	0.062
N30	0.024	1100	1164	11.84	0.064
N31	0.084	1129	1173	10.76	0.055
N39	0.436	1252	1302	5.33	0.053
N40	0.178	1087	1175	3.77	0.077
N41	0.268	984	1094	7.73	0.078

\*  $d = \sqrt{\text{pore area}(4/\pi)}$ .

material is due to extreme-sized pores only and not due to any microstructural or strain hardening characteristics.

#### IV. DISCUSSION

The effect of microstructure on fracture of material is often interpreted in terms of the strength and ductility of a material at the crack tip. For a pore-free material, fracture toughness is correlated to the fracture stress and fracture strain of the region at the crack tip, through the relationship<sup>[29]</sup>:

$$K_{Ic} = \sqrt{\frac{2CE\varepsilon_c\sigma_y n}{1 - \nu^2}}, \quad [1]$$

where  $C$  is a constant,  $E$  is the elastic modulus,  $\nu$  is the Poisson's ratio,  $\varepsilon_c$  is the fracture strain,  $\sigma_y$  is the yield stress, and  $n$  is the strain hardening exponent. Usually, an increase in strength in metallic materials causes a large reduction in fracture toughness. This is because the adverse effect of a decrease in ductility on fracture toughness is more than the positive effect due to strengthening. Hence, the reduction in the fracture toughness with an increase in strength for various materials, as reported in the literature<sup>[29]</sup> is ultimately connected to the fracture strain at the tip of the crack. In PM alloys, fracture toughness measurements indicate<sup>[30,31]</sup> that with an increase in porosity, both fracture toughness and tensile strength decrease because there is less material to support the stress at higher porosity levels. If we follow this correlation, one would have to

conclude that in porous materials, fracture toughness increases with an increase in tensile strength, which is contrary to the trend in wrought materials.

The development of such a fracture-toughness-based explanation for the present trend in tensile ductility is difficult for various reasons. First, to establish any correlation between fracture toughness and tensile properties, one would have to have test results with varying porosity levels. This is not the case in the present material, because the average volume fraction of porosity in all the samples is nearly the same and does not vary significantly between the samples. Secondly, all tensile fractures in the present samples occurred from a single extreme-sized pore. The material next to the pore in all the samples has nearly equivalent intrinsic fracture properties. If the fracture toughness measurements were made on the present material, they would probably show only a slight variation from each other, because the variation of bulk porosity is small. Hence, analysis of the present data based on fracture toughness is not possible and not relevant to the present investigation. The large variation in ductility between microstructurally identical samples (Table II) can be explained only on the basis of the sizes of the extreme-sized pores.

##### A. Effect of Porosity on Strength

From Figure 4(b), it is evident that yield strength (YS) and the tensile strength (TS) levels are not affected by the presence of extreme-sized pores. In addition, the fracture stress is also largely independent of the pore size (Figure 4(c)). These trends are surprising, because the pores in these samples, either considered in terms of

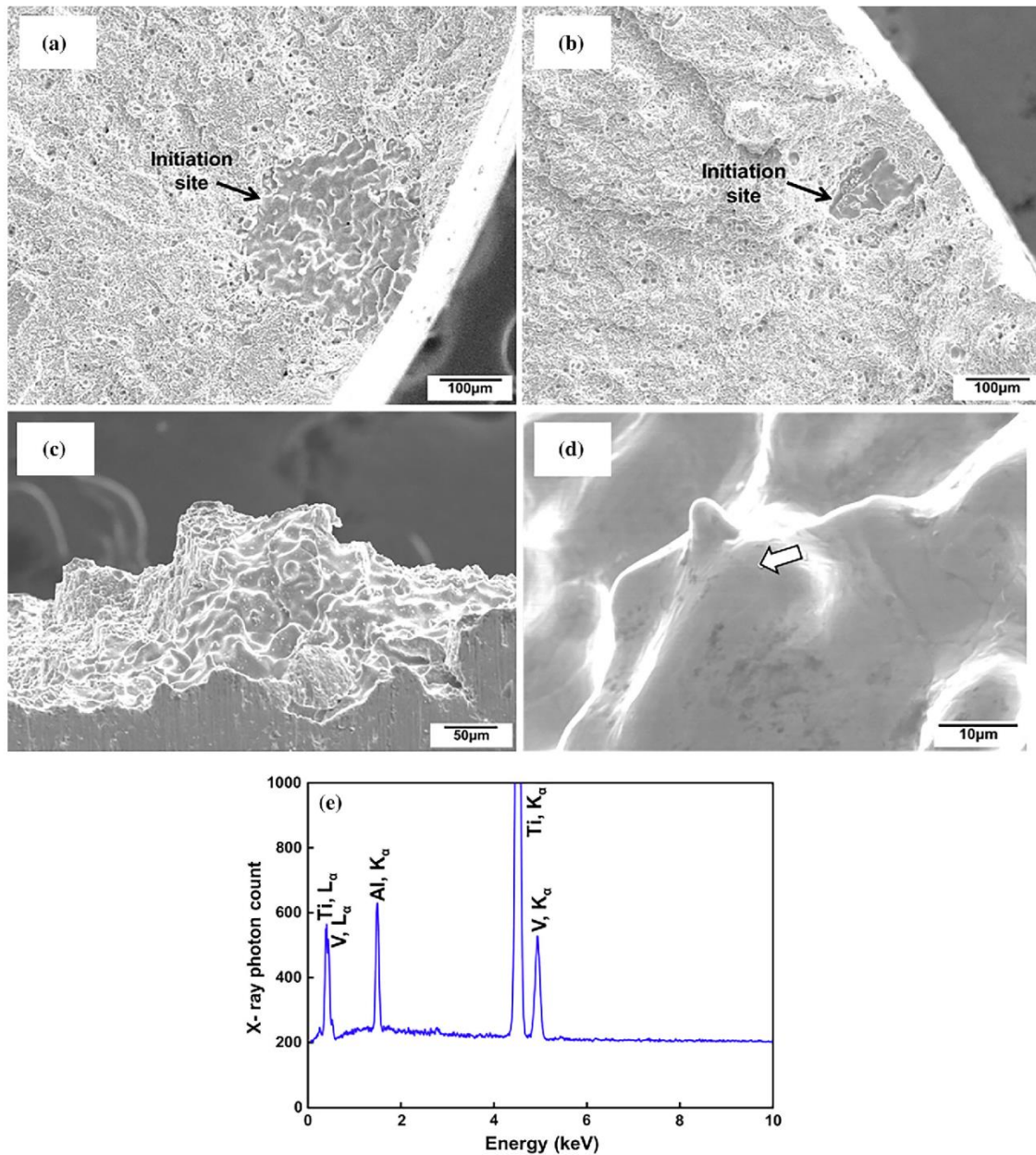


Fig. 5—SEM fractograph of (a) ~1.5 pct elongation sample and (b) ~12 pct elongation sample in group A; (c) showing the cross-sectional view of group A pore, (d) surface of group A pore indicating the point of EDS analysis, and (e) the corresponding EDS pattern.

volume fraction or extreme size, do not seem to affect strength. Several studies,<sup>[19–22]</sup> however, have reported that an increase in porosity reduces the yield or ultimate tensile strength and the ductility at the same time. These decreases in strength levels and ductility were attributed to the loss of load bearing area due to the occupancy of pores in the volume of the materials. Consider the two

extreme porosity samples of the present study from Table II, that is, the sample N30 having 0.35 pct porosity and the sample N14 having porosity 0.94 pct by volume. The YSs were 1100 and 1191 MPa, and the TS values are 1164 and 1191 MPa for N30 and N14, respectively. It is clear that a factor of three increase in the volume fraction of porosity did not change the YS or TS. This is also

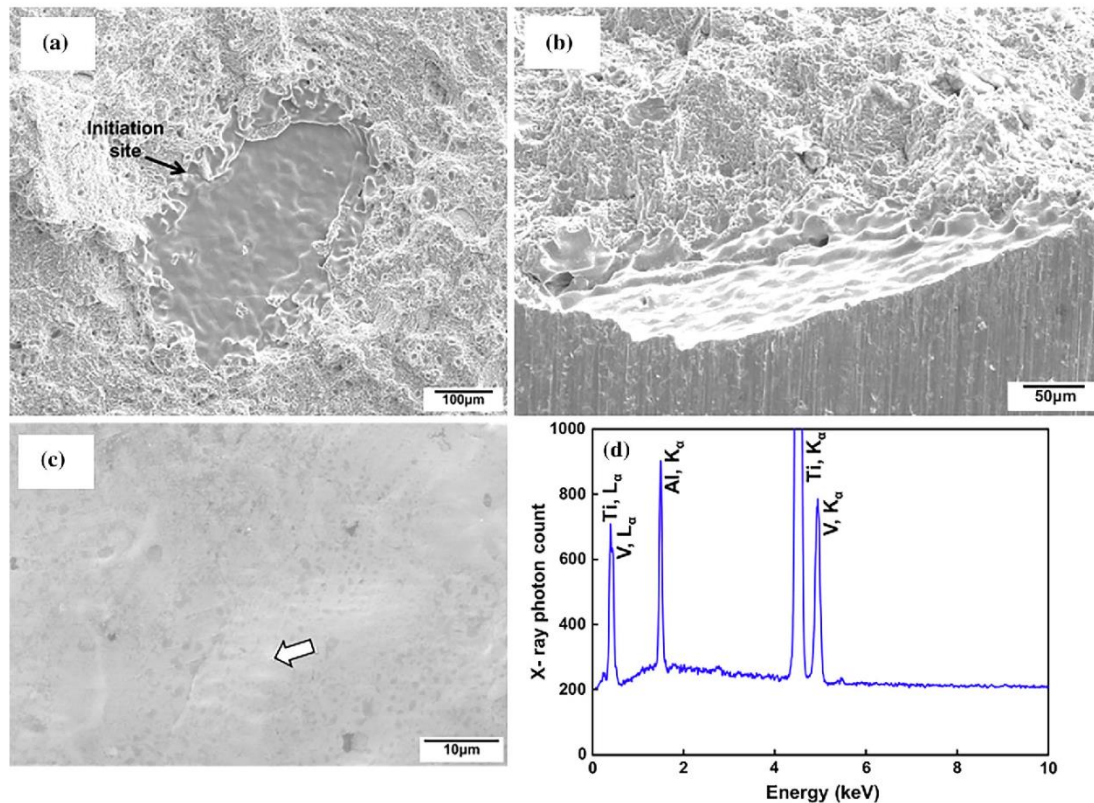


Fig. 6—(a) SEM fractograph of group B pore, (b) high angle view after sectioning through group B pore, (c) surface of group B pore indicating the point of EDS analysis, and (d) the corresponding EDS pattern.

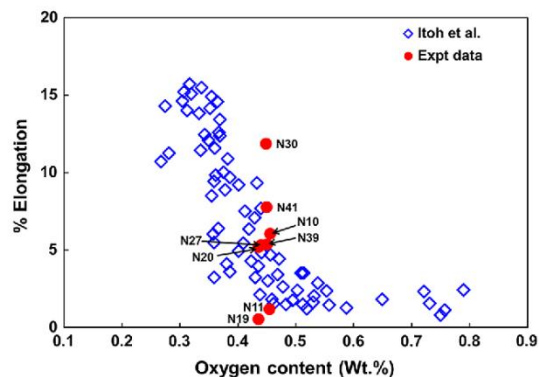


Fig. 7—Effect of oxygen content on the ductility of PM Ti-6Al-4V alloy.<sup>[35]</sup>

supported by the work of Yan *et al.*,<sup>[32]</sup> which showed that an increase in the porosity from 1 to 5 pct in PM Ti-6Al-4V alloy does not significantly change the tensile strength properties. Mugica *et al.*<sup>[33]</sup> in their study of an Al alloy, however, have shown that the degradation of tensile strength properties is directly related to volume fraction

of porosity on the fracture surface, which is usually higher than the global volume fraction. In the present study, although the size of the extreme-sized pore varies from sample to sample, the average pore volume fraction at any cross section remained nearly the same. In addition, the extreme-sized pores are not large enough to affect the tensile strength. For the sample N12 with the largest extreme-sized pore (~0.85 mm), the corresponding pore volume fraction due to this pore was 0.0179 (bulk volume fraction: 0.0066). The smallest extreme-sized pore (~0.02 mm) in the sample corresponded to a pore volume fraction of 0.000010 (bulk volume fraction: 0.0035). Both of these samples showed nearly the same YS of ~1100 MPa. Thus, it can be argued that in the present material even the extreme-sized pores when considered alone do not affect the strength of the material. Therefore, it is clear that porosity, either in the form of their volume fraction in the bulk or their individual extreme-sized nature, does not significantly affect the strength levels of the present material.

#### B. Effect of Porosity on Tensile Ductility

The tensile ductility is plotted as pct elongation against the size of extreme-sized pores from each



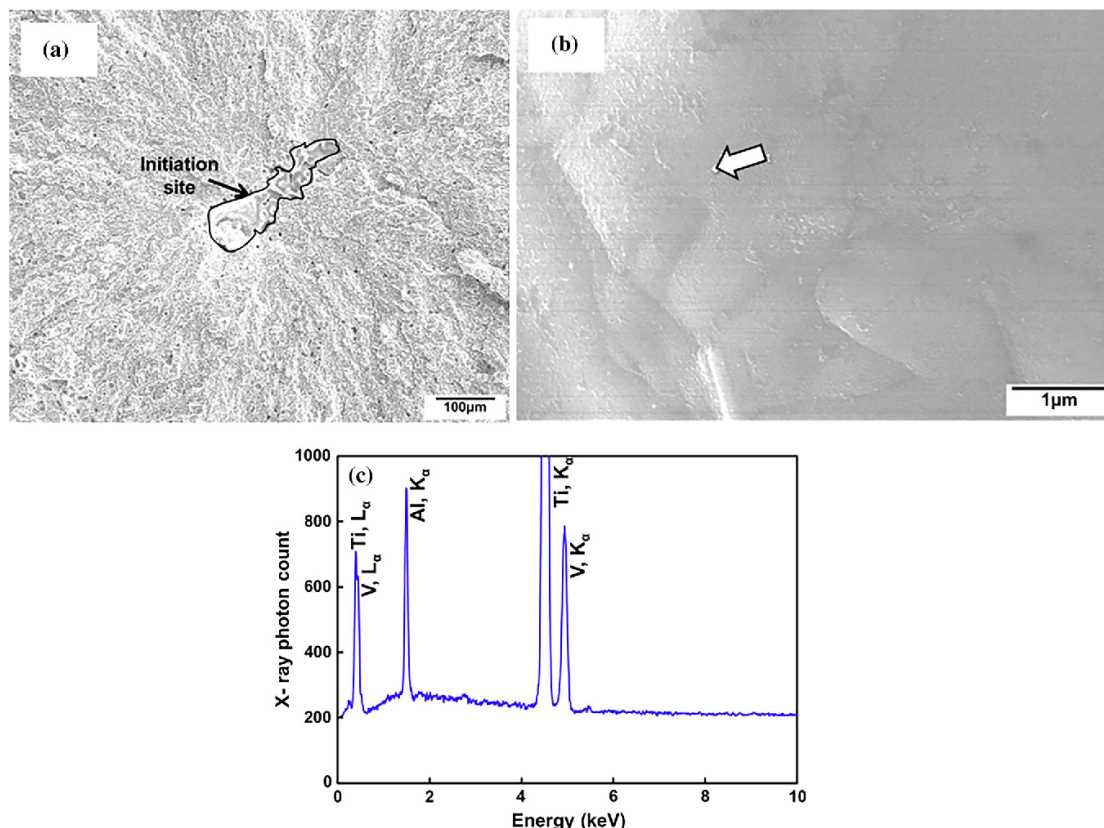


Fig. 8—(a) SEM fractograph of group C pore, (b) surface of group C pore indicating the point of EDS analysis, and (c) the corresponding EDS pattern.

fracture surface (Figure 4(d)). The tensile ductility decreased from 12.3 to 0.24 pct as the extreme pore size increases from 0.063 to 0.847 mm (Table II). It is evident that the reduction in cross section due to pores (dashed line) is not adequate to explain the ductility trend of any sample group in Figure 4(d). In Figure 4(d), the data have been divided into three groups (labeled A, B, and C), which are based on morphological differences of extreme pores as described below.

Figures 5(a) and (b) present the fractographs showing the morphology of fracture initiation in group A specimens. Multiple rounded asperities were found within the internal surface of the extreme-sized pores. These types of asperities were probably formed during particle agglomeration and fusion, and reflect incomplete sintering of particles. Some titanium hydride particles may have formed a large “cave” during the CIPing process, resulting in incomplete densification leading to the formation of a large pore.<sup>[34]</sup> This explanation is also supported by the EDS (Figures 5(d) and (e)) analysis and fractography of pore surfaces (Figure 5(c)). The EDS result indicates that these pores have the same chemical composition as that of the

Ti-6Al-4V matrix. Therefore, chemical segregation or inclusions are not the likely causes for ductility loss. All of the fracture-initiating pores in group A are this type and they are responsible for the observed exponential decrease in ductility. However, significantly different morphologies of extreme-sized pores and different ductility trends with pore size were observed for the samples in ‘B’ and ‘C’ groups. This is discussed in the following.

In group B, extreme pores with a single flat facet were found on the tensile fracture surfaces (Figures 6(a) and (b)). It is believed that some kind of particle layering occurred during the powder filling and compaction process, which remained even after sintering. These layers probably did not bond during sintering leading to the flat facet morphology of the pore. During the tensile loading, these layers probably de-bonded early due to weakness between the layers and thus led to fracture initiation from the pore. The EDS result confirms that the chemical composition of the pore is same as that of the matrix (Figures 6(c) and (d)). However, the presence of this type of extreme-sized pore seems to affect the tensile ductility less severely than the pores in the samples of group A pores. For example, for a given pore

size of ~0.45 mm, the group B specimen shows a ductility of ~5 pct compared to ~1 pct for sample from group A.

The large discrepancy in ductility at a given pore size between samples in group A and B could be explained on the basis of a peculiar variation in ductility with the bulk oxygen content in these materials. The effect of oxygen content on ductility of PM titanium alloys was investigated by Itoh *et al.*<sup>[35]</sup> In their study on the injection molded Ti-6Al-4V alloy, prepared using a powder mixture of Ti + TiH<sub>2</sub> + Al-40V, the tensile ductility was found to be strongly affected by the oxygen content. Itoh's data are reproduced in Figure 7. At around 0.4 wt pct oxygen, a large variation in tensile ductility, up to a factor of about 5, was observed. The average oxygen content of the present PM Ti-6Al-4V titanium alloys is ~0.43 wt pct. The oxygen levels of selected samples of the present study were determined and are plotted along with Itoh's data in Figure 7. It can be seen that there is a similarity between the two sets of data, that is, a large variation in tensile ductility is seen at around 0.4 wt pct oxygen. A large variation in ductility around 0.4 pct oxygen may be explained on the basis of small changes in oxygen level around the extreme-sized pore, affecting the level of fracture strain needed for crack initiation. However, it is difficult to determine the small changes in oxygen level in regions around the extreme-sized pores. Our previous work<sup>[36]</sup> has shown that the extreme-sized pores do not form when the oxygen content is <0.3 wt pct. An Oxygen content of ~0.4 wt pct or more will likely affect the sintering kinetics greatly, leading to formation of extreme pores in the samples. The local oxygen content in the vicinity of the crack initiating pore in the group B samples could be slightly lower than the average oxygen content of ~0.43 wt pct. In addition, because oxygen is partially removed during dehydrogenation, the extent of this removal around the pore could vary depending on the type of pore. Such variations can cause changes in local fracture strain causing a large variation in the tensile ductility as in Figure 4(d). It is quite likely that the large variation in tensile ductility in Itoh's data is actually caused by the extreme-sized pores, but such an analysis was not performed in that study. Besides the above discussion, it is not possible to speculate any further about the ductility behavior of samples in group B, relative to that in group A.

In group C, profoundly elongated extreme-sized pores were observed on the tensile fracture surfaces (Figure 8(a)). EDS analysis (Figures 8(b) and (c)) again indicated that the composition of the interior of the pores is similar to that of the matrix. This confirms that there was no inclusion or impurity in these pores. The aspect ratios in the fracture planes of group C pores ranged from ~3 to 7.5, whereas pores from group A and group B varied from ~1 to ~1.8 and ~1.2 to ~1.5, respectively. The aspect ratio is defined here as the ratio of largest dimension of the exposed pore to the shortest dimension. The local stress concentration along the pore front will vary depending on the pore aspect ratio. The stress intensity factor ( $K$ ) and how it varies with aspect ratio is a useful way to describe the stress distribution

around a non-circular flaw. The Irwin's equation<sup>[37]</sup> for the variation of stress intensity factor ( $K$ ) along the front of an elliptical crack is

$$K = \frac{\sigma\sqrt{\pi a}}{\phi} \left( \sin^2 \phi + \frac{a^2}{c^2} \cos^2 \phi \right)^{\frac{1}{4}}, \quad [2]$$

where  $K$  is the stress intensity factor,  $\sigma$  is applied tensile stress normal to the crack plane,  $\phi$  is the elliptical integral, and  $2a$  and  $2c$  are the minor and the major axis dimensions, respectively. The parameter  $\phi$  is the angle between the line to any point on elliptical crack front and the major axis of the flaw.

For a circular pore of size 300  $\mu\text{m}$ , that is  $2a = 2c = 300 \mu\text{m}$ , the calculated  $K$  is  $\sim 0.02\sigma \text{ MPa}\sqrt{\text{m}}$  and is the same at any point along the circular front of the pore. However for a pore of the same size,  $c = 300 \mu\text{m}$ , but with the aspect ratio of 3, ( $\frac{c}{a} = 3$ ), the  $K$  value is not the same along the front of the pore. The stress intensity factors at the points of the major axis and the minor axis are  $\sim 0.016\sigma$  and  $\sim 0.027\sigma \text{ MPa}\sqrt{\text{m}}$ , respectively. Extending the crack analogy to the elongated pores in the present work, the stress concentration in the pore vicinity along the shorter dimension of the pore is much higher than that along the longer dimension. This non-uniform stress concentration will also lead to a non-uniform strain distribution around the pore. The strain at the pore front, specifically at the shorter dimension of an elongated pore can reach to the level of fracture strain even when the total macroscopic strain is very small. Hence, for a given pore size, an elongated pore (high aspect ratio) can lead to earlier fracture initiation than a circular pore, and therefore can lead to a much lower uniform strain in the gage section before fracture, relative to a circular pore of the same size. Thus, the lowest levels of ductility were observed for the group C samples.

It is apparent from the above discussion that cracks initiated from extreme-sized pores, and grew across the specimens, leading to final fractures. Irrespective of the type of extreme-sized pore, the ductility of the sample decreased exponentially with increasing pore size. This indicates that fine pores present in the volume of the samples do not significantly affect the ductility of the sample. Due to stress concentration, the stress in the vicinity of the extreme-sized pore can reach the fracture stress even when the macroscopic stress (in a pore-free region) is much lower.<sup>[19,38–40]</sup> The strain distributions, therefore, are non-uniform during the tensile loading of samples, and the plane containing the pore can reach the level of fracture strain much earlier than the bulk material. Hence, the fracture begins in the pore vicinity and propagates toward the surface, thus reducing the extent of plastic deformation of the uniform section and the overall elongation. Similarly, ductility reduction in Al alloys due to the presence of large pores has also been reported in the literature,<sup>[5,25,41]</sup> but has never been attributed to the extreme-sized pores in these materials.

### C. Mechanism of Pore Size Effect on Ductility

Most previous investigations<sup>[19,20,24]</sup> that examined the effect of pores on the ductility of cast, PM, or

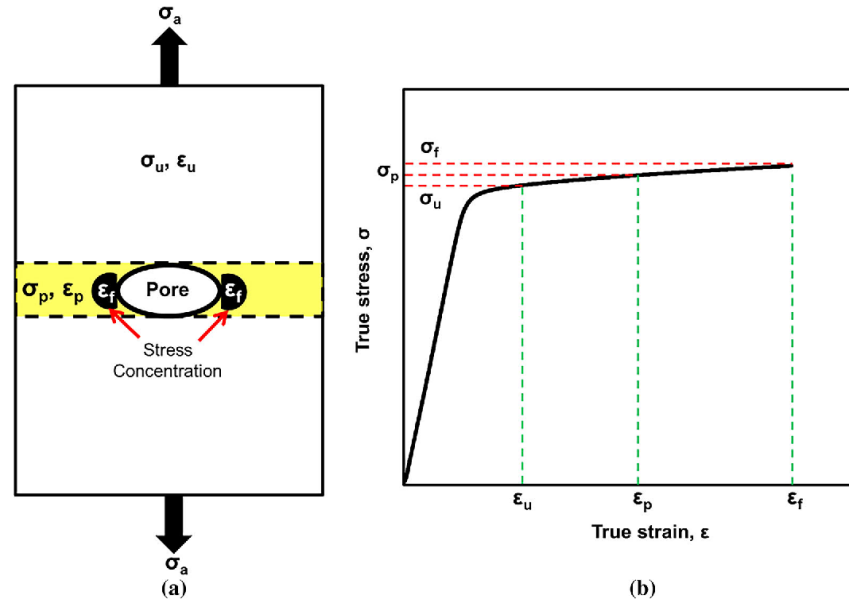


Fig. 9—Schematic diagram of (a) strain distribution in a sample containing a large pore under tensile loading and (b) the corresponding true stress-true strain curve.

wrought materials have emphasized the significance of bulk volume fraction of pores in the material, but not the extreme-sized pores. In this section, we develop a mechanistic explanation for the effect of extreme-sized pores on tensile ductility.

As discussed in the earlier sections, it was apparent that the fracture always initiated from an extreme-sized pore in the samples of the present material. The mechanism of ductility reduction due to extreme size pores can be explained with the aid of Figure 9. Consider that the pore-free volume of the specimen has a cross-sectional area  $A_u$  and an effective cross-section area of the plane containing the pore is  $A_p$ . When a specimen is under tensile stress  $\sigma_a$ , the level of uniform stress and strain in the pore-free section are  $\sigma_u$  and  $\epsilon_u$ , respectively, while the corresponding quantities  $\sigma_p$  and  $\epsilon_p$  are the average stress and strain in the plane containing the pore. In the vicinity of a pore, the concentrated strain is defined as  $\epsilon_f$ . It is evident that the stress levels in the three regions (the pore-free section, the plane containing the pore, and the region next to the pore) would be different at any time during the loading of the sample. As an example, if we assume a stress concentration factor of 3 in the pore vicinity and the stress in this region is  $\sigma_f$ , the average stress in the plane containing the pore,  $\sigma_p$ , should be

$$\sigma_p = \frac{\sigma_f}{3}. \quad [3]$$

The corresponding stress in the uniform region  $\sigma_u$  is given by

$$\sigma_u = \frac{\sigma_f}{3} \left( \frac{A_p}{A_u} \right). \quad [4]$$

Equations [3] and [4] indicate that the stresses in the three different regions considered above will be evidently different. The corresponding strains will be also significantly different, as illustrated schematically in the stress-strain curve (Figure 9(b)). The differences between the strain levels in the three regions will be strongly affected by the strain hardening characteristic of the matrix. For the present material, where the true stress-true strain curves are nearly horizontal (Figure 4(a)), the difference between the local and the uniform macroscopic strains can be very large. A very small increase in stress after yielding can thus cause a large increase in strain near the pore, even with a small stress concentration factor, even though the plastic strain in the uniform section is very small. Thus, the material in the pore vicinity will be traveling along the stress-strain curve far ahead of the uniform strain and can reach the fracture strain much earlier than in the uniform section. Hence, fracture is initiated prematurely around the pore region when the fracture strain is reached in that area, before the pore-free section has a chance to be plastically deformed to a maximum extent. The larger the extreme-sized pore, the earlier will be the fracture initiation during deformation, thus severely limiting the extent of plastic deformation of the gage section. Thus, the exponential decrease in ductility as a function of extreme pore size can be explained.

## V. CONCLUSION

This study has examined how extreme-sized pores control the tensile properties of HSPT-processed PM Ti-6Al-4V alloy. The specific conclusions are as follows:

1. Extreme-sized pores lead to a rapid decrease in tensile ductility of the PM Ti-6Al-4V alloy. Three distinct trends of decreasing ductility with increases in the extreme pore size were seen and were classified on the basis of the type of extreme-sized pores found in the material.
2. A surprising finding is that neither the volume fraction of pore nor the extreme-sized nature of the pore affects the tensile strength properties in the material. The strength properties remained nearly constant in all specimens.
3. Fracture always initiated from an extreme-sized pore in the material with the remaining smaller pores did not play any significant role in affecting the tensile properties.
4. The shape of pore and the oxygen concentration of about 0.4 wt pct play a unique role in severely degrading the ductility. The former effect is attributed to the increased stress concentration in an elongated pore. The latter is yet to be investigated in more detail.
5. A mechanistic explanation, based on stress concentration around the pore and how that limits the uniform elongation of the material, is provided to explain the ductility trend observed. This revealed that the ductility variation as a function of pore size could also be a function of the strain hardening exponent. However, no systematic effect on ductility, due to a variation in the strain hardening exponent at a given pore size could be discerned.

## ACKNOWLEDGMENTS

The authors duly acknowledge a financial grant from the U.S. Department of Energy, Innovative Manufacturing Initiative (DEEE0005761), through the Advanced Manufacturing Office and the Office of Energy Efficiency and Renewable Energy. The initial raw powders were supplied by Ametek Specialty Metal Products, PA. We also thank James Paramore and Pei Sun for their help in the experimental work.

## REFERENCES

1. F.H. Froes, S.J. Mashl, V.S. Moxson, J.C. Hebeisen, and V.A. Duz: *JOM*, 2004, vol. 56, pp. 46–48.
2. F.H. Froes and C. Suryanarayana: *Rev. Part. Mater.*, 1933, vol. 1, pp. 233–75.
3. F.H. Froes and D. Eylon: *Int. Mater. Rev.*, 1990, vol. 35, pp. 162–82.
4. V.A.R. Henriques, C.A.A. Cairo, and J.C. Bressian: *Mater. Res.*, 2005, vol. 8, pp. 443–46.
5. C.H. Caceres: *Scripta Metall. Mater.*, 1995, vol. 32, pp. 1851–56.
6. Y. Liu, L.F. Chen, H.P. Tang, C.T. Liu, B. Liu, and B.Y. Huang: *Mat. Sci. Eng. A*, 2006, vol. 418A, pp. 25–35.
7. M. Hagiwara, Y. Kaieda, Y. Kawabe, and S. Miura: *ISIJ Int.*, 1991, vol. 31, pp. 922–30.
8. O.M. Ivasishin, D.G. Savvakina, F. Froes, V.C. Mokson, and K.A. Bondareva: *Powder Metall. Met. Ceram.*, 2002, vol. 41, pp. 382–90.
9. A. Carman, L.C. Zhang, O.M. Ivasishin, D.G. Savvakina, M.V. Matviychuk, and E.V. Pareloma: *Mater. Sci. Eng. A*, 2011, vol. 528, pp. 1686–93.
10. O.M. Ivasishin and D.G. Savvakina: *Key Eng. Mat.*, 2010, vol. 436, pp. 113–21.
11. O.M. Ivasishin, D.G. Savvakina, M.M. Gumenyak, and O.B. Bondarchuk: *Key Eng. Mat.*, 2012, vol. 520, pp. 121–32.
12. W.R. Kerr: *Metall. Trans. A*, 1985, vol. 16A, pp. 1077–87.
13. D.H. Kohn and P. Ducheyne: *J. Mater. Sci.*, 1991, vol. 26, pp. 534–44.
14. W.R. Kerr, P.R. Smith, M.E. Rosenblum, F.J. Gurney, Y.R. Mahajan, and L.R. Bidwell: *Titanium'80, Science and Technology, Proceedings of the 4th International Conference on Titanium*, Metall. Soc. AIME, Kyoto, Japan, 1980, pp. 2477–86.
15. W.H. Kao, D. Eylon, C.F. Yoltan, and F.H. Froes: *Powder Metall.*, 1981, vol. 37, pp. 289–301.
16. F.H. Froes, O.N. Senkov, and J.I. Qazi: *Int. Mater. Rev.*, 2004, vol. 49, pp. 227–45.
17. Z.Z. Fang, P. Sun, and H. Wang: *Adv. Eng. Mat.*, 2012, vol. 14, pp. 383–87.
18. B. Hariprasad, T.H. Courtney, and J.K. Lee: *Metall. Trans. A*, 1988, vol. 19A, pp. 517–26.
19. R.J. Bourcier, D.A. Koss, R.E. Smelser, and O. Richmond: *Acta Metall.*, 1986, vol. 34, pp. 2443–53.
20. A.M. Gokhale and G.R. Patel: *Scripta Mater.*, 2005, vol. 52, pp. 237–41.
21. D. Bozic, D. Sekulic, J. Stasic, V. Rajkovic, and M.T. Jovanovic: *Int. J. Mater. Res.*, 2008, vol. 99, pp. 1268–74.
22. H. Wang, Z.Z. Fang, and P. Sun: *Int. J. Powder Metall.*, 2010, vol. 46, pp. 45–57.
23. H. Mae, X. Teng, Y. Bai, and T. Wierzbicki: *J. Sol. Mech. Mater. Eng.*, 2008, vol. 2, pp. 924–42.
24. R.J. Shore and R.B. McCauley: *Weld Research supplement, 51st Annual Meeting*, Cleveland, OH, June 8–12, 1970, pp. 311s–21s.
25. M.K. Surappa, E. Blank, and J.C. Jaquet: *Scripta Met.*, 1986, vol. 20, pp. 1281–86.
26. P. Sun, Z.Z. Fang, and M. Koopman: *Adv. Eng. Mater.*, 2013, vol. 15, pp. 1007–13.
27. J.D. Paramore, Z.Z. Fang, P. Sun, M. Koopman, M. Dunstan, and M. Koopman: *Scripta Mater.*, 2015, vol. 107, pp. 103–06.
28. P. Sun, Z.Z. Fang, M. Koopman, Y. Xia, J. Paramour, K.S. Ravi Chandran, Y. Ran, and J. Lu: *Metall. Mater. Trans. A*, 2015, vol. 46A, pp. 5546–60.
29. K.S. Ravi Chandran and A.K. Vasudeven: *Fatigue and Fracture*, ASM International, Materials Park, 1996, pp. 381–92.
30. S.H. Teoh, R. Thampuran, W.K.H. Seah, and J.C.H. Goh: *Biomaterials*, 1993, vol. 14, pp. 407–12.
31. N.R. Moody, W.M. Garrison, Jr., J.E. Smugeresky, and J.E. Costa: *Metall. Trans. A*, 1993, vol. 24A, pp. 161–74.
32. Y. Yan, G.L. Nash, and P. Nash: *Int. J. Fatigue*, 2013, vol. 55, pp. 81–91.
33. G.W. Mugica, D.O. Tovio, J.C. Cuyas, and A.C. Gonzalez: *Mater. Res.*, 2004, vol. 7, pp. 221–29.
34. F. Cao, P. Kumar, M. Koopman, C. Lin, Z.Z. Fang, and K.S. Ravi Chandran: *Mater. Sci. Eng. A*, 2015, vol. 630A, pp. 139–45.
35. Y. Itoh, T. Uematsu, K. Sato, and H. Miura: *J. Jpn. Soc. Powder Powder Metall.*, 2009, vol. 56, pp. 259–63.
36. P. Kumar, K.S. Ravi Chandran, F. Cao, P. Sun, M. Koopman, and Z. Zak Fang: *Titanium-2015, Science and Technology, 13th world Conference on Titanium*, TMS, San Diego, CA, August 16–20, 2015.
37. G.R. Irvin: *J. Appl. Mech.*, 1962, vol. 29, pp. 651–54.
38. N. Chawla and X. Deng: *Mater. Sci. Eng. A*, 2005, vol. 390, pp. 98–112.
39. S.J. Polasik, J.J. Williams, and N. Chawla: *Metall. Mater. Trans. A*, 2002, vol. 33A, pp. 73–81.
40. A. Hardrboletz and B. Weiss: *Int. Mater. Rev.*, 1997, vol. 42, pp. 1–44.
41. C.H. Caceres and B.I. Selling: *Mater. Sci. Eng. A*, 1996, vol. 220, pp. 109–16.

## **CHAPTER 6**

### **A CONSTITUTIVE EQUATION TO PREDICT THE PORE SIZE EFFECT ON TENSILE DUCTILITY OF LOW POROSITY MATERIALS**

(Manuscript in preparation)



## 6.1 Introduction

The wide application of materials containing residual porosity, such as cast components and powder metallurgy (PM) components, is hindered by a large scatter in their fracture properties. Components made using similar processing conditions often show varying tensile properties due to the presence of random pores. Studies [1–6] have shown that the presence of porosity significantly reduces the tensile ductility in metallic materials. A decrease in tensile ductility of aluminum (Al) welds from 15% to 10% was observed when volume fraction porosity increased from 0% to 5% [7]. Chawla et al. [8] studied the effect of volume fraction of pores on the tensile properties of sintered steel. They showed that the tensile ductility decreased from ~ 7% to ~ 2% as the porosity volume fraction increased from ~ 3% to ~ 10%. Bourcier et al. [3] reported a decrease of 50% in tensile ductility of PM Ti-6Al-4V, when the porosity increased from 2% to 4%. It is clear that porosity, even at small volume fractions, has a strong detrimental effect on tensile ductility. The reduction in ductility was attributed to the strain concentration around the pores. Over the years, various relationships have been developed to quantitatively correlate the ductility to the volume fraction of porosity [3,9,10]. Caceres [11] assumed strain concentration due to pores, and presented a simple model to predict ductility in the presence of defect:

$$\sigma_i(1-f)^{A_{oe}-\varepsilon_i} = \sigma_h A_{oe}-\varepsilon_h \quad (6.1)$$

where  $\sigma_i, \varepsilon_i$  and  $\sigma_h, \varepsilon_h$  are the true stresses and the true strains in the pore region and in the pore-free region of the specimen, respectively. The tensile ductility was numerically determined by solving Equation (6.1). However, in addition to the difficulty with

numerical calculations, the model underestimated the tensile ductility, when compared with the experimentally observed ductility values of cast Al alloy containing small volume fractions of porosity [12]. Gokhale et al. [9] correlated the tensile ductility to the area fraction of porosity found on the fracture surface in cast Al alloys, as given in the following equation (6.2):

$$e = e_0(1-f)^n \quad (6.2)$$

where  $e$  is the percentage tensile elongation,  $e_0$  is the percentage elongation of defect-free cast alloy of similar microstructure and  $n$  is an empirical constant. The authors explained the ductility reduction due to porosity on the basis of volume fraction. However, studies showed that in low volume fraction porosity, it is the size of the largest pore in the test volume that controls the ductility of materials. For example, Surappa et al. [13] carried out a study on the effect of low volume fraction porosity (<0.40%) on the ductility of an Al alloy. They found that the tensile ductility increased with an increase in the volume fraction of porosity. It was pointed out that this could be due to the nonuniform distribution of pores in the test bar. They showed that the reduction in tensile ductility could be related to the projected area of macropores on the fracture surface. The tensile ductility rapidly decreased from ~ 15% to ~ 2% when the projected area increased from ~ 1 mm<sup>2</sup> to ~ 7 mm<sup>2</sup>. Microcracks that were observed near the macropores indicated that stress concentration around the pore led to the crack initiation and fracture. Similar findings are reported for PM Ti-6Al-4V alloy by Kumar et al. [14,15]. Therefore, it appears that ductility is affected by the size of macropores on the fracture plane rather than the volume fraction of pores. Porosity present in small fractions can, therefore, make

the tensile behavior of materials unpredictable. In general, the large reductions in ductility at low porosity levels, observed in many metallic materials, are a serious problem and remain to be clearly explained.

In the literature, investigations that carefully examined the effect of pore size on tensile ductility are very rare [13–16]. Nilsson et al. [17] developed a probabilistic fracture model to correlate the size of defect with ductility. Teng et al. [18] studied the effect of pore size on tensile ductility in Al alloy and established a linear relationship between fracture strain and pore size. However, most of studies showed that the tensile ductility does not vary linearly with pore size. A better model is, therefore, warranted to explain the tensile ductility behavior of PM Ti-6Al-4V with pore size.

In the present work, an analytical model is developed to predict the influence of size of the largest pore in the test volume on tensile ductility, based on assumption that the pore-containing area yields first, causing strain concentration and early crack initiation. The model is evaluated here using the experimental data from the literature for cast and PM materials. The practical significance of this study is that with an analytical relationship one would be able to predict the ductility of high-density cast and PM materials if the size of the largest pore can be measured using nondestructive methods such as ultrasonic, x-ray tomography etc.

## **6.2 Mechanism of Fracture Due to Presence of a Large Pore**

The presence of porosity in a tensile sample reduces the load-bearing area. Therefore, it can be said that a region containing pores will yield first, leading to strain concentration when uniform macroscopic load is applied. The rate of strain concentration will depend

on the strain hardening characteristics of the materials as described in section 6.4.

It is apparent from the studies that tensile fracture initiates from a large pore in the samples. A large pore locally creates stress concentration, which results in incipient neck. The plastic instability due to this neck and fracture of the sample can be described with Figure 6.2. In Figure 6.2, a schematic diagram of gage section of a tensile specimen is showing the three different regions, the pore-free volume, the pore-containing region, and the region next to the pore. With reference to Figure 6.2, the cross-section of the pore-free volume of the specimen has a cross-sectional area  $A_u$ , and the cross-section area of the plane containing the pore is  $A_p$ . Under applied tensile stress  $\sigma_a$ , the average uniform stress and strain in the pore-free section are  $\sigma_u$  and  $\epsilon_u$ , respectively, and, quantities  $\sigma_p$  and  $\epsilon_p$  are the average stress and strain in the pore containing plane. The strain in the vicinity of the pore is defined as  $\epsilon_f$ . During loading, the stress levels in the three regions of the gage section of the sample would be different. For example, if we assume a stress concentration factor  $K$  (always  $>1$ ) in the pore vicinity, the average stress in this region,  $\sigma_f$ , should be

$$\sigma_f = K\sigma_p \quad (6.3)$$

The corresponding stress in the uniform region  $\sigma_u$ , is given as follows:

$$\sigma_u = \frac{\sigma_f}{K} \left( \frac{A_p}{A_u} \right) \quad (6.4)$$

The above equations (6.3, 6.4) indicate that the stresses in the three different regions considered will be evidently different. The corresponding strains will also be different and the differences between the strain levels in the three regions will be decided by the

strain-hardening characteristic of the materials. Considering the Surrapa et al. [13] study, for which the true stress-true strain curve of the material is nearly horizontal. The difference between the strain next to the pore and the uniform macroscopic strains can be very large. A very small increase in stress due to stress concentration factor can cause a large increase in strain near the pore even though the strain in the uniform section is very small. Therefore, the material in the pore vicinity can reach the fracture strain much earlier than in the uniform section. Hence, fracture is initiated prematurely around the pore region when the fracture strain is reached in that area, even before the pore-free region reaches to the maximum plastic deformation. The larger the extreme-sized pore, the earlier will be the fracture initiation during deformation, thus severely limiting the uniform strain of materials.

### 6.3 Analytical Model

It is considered that a material with small pores deforms uniformly and reaches to maximum uniform strain during tensile loading. However, the extent of uniform strain is limited in a material containing an extreme-sized pore due to strain concentration in the extreme-sized pore region.

The true-stress versus true-strain behavior of metals can be described by the Voce relationship (Eq. 6.5):

$$\left( \frac{\sigma - \sigma_y}{\sigma_\infty - \sigma_y} \right) = 1 - \exp \{ - C \varepsilon^n \} \quad (6.5)$$

where  $\sigma$  is the true stress at any uniform strain  $\varepsilon$  and  $\sigma_y$  and  $\sigma_\infty$  are the yield stress and the saturation stress corresponding to the ultimate strain, respectively. The parameters  $C$  and

n characterize the strain-hardening characteristics of the material.

### 6.3.1 Case I: Material Containing Uniformly Distributed Small Pores

Deformation behavior in this case (Figure 6.1a) can be given as

$$1 - \left( \frac{\sigma_{u_0} - \sigma_y}{\sigma_\infty - \sigma_y} \right) = \exp \left\{ -C \varepsilon_{u_0}^n \right\} \quad (6.6)$$

where  $\sigma_{u_0}$  and  $\varepsilon_{u_0}$  corresponds to uniform stress and strain, respectively, in the specimen.

In this case, each pore in the material is equally responsible for the fracture of the material. The fracture of the material occurs through the fracture of the ligaments between the pores. The ligaments will fracture when the local strain reaches the fracture strain. By Re-arranging equation (6.6), fracture strain  $\varepsilon_f$  can related to the stress in fracture plane ( $\sigma_{p_0}$ ) as follows:

$$\sigma_{p_0} = \sigma_\infty - (\sigma_\infty - \sigma_y) \exp \left\{ -C \varepsilon_f^n \right\} \quad (6.7)$$

where  $\sigma_{p_0}$  is stress in the fracture plane.

The stress next to pore ( $\sigma_{f_0}^*$ ) will be given as follows:

$$\sigma_{f_0}^* = K_\sigma \sigma_{u_0} \quad (6.8)$$

where,  $K_\sigma$  is stress concentration factor due to the pore, which is related to the theoretical elastic concentration factor  $K_t$ , which is described in section 6.4.

Now, in this case uniform section ( $\sigma_{u_0}$ ) is related to  $\sigma_{p_0}$  as follows:

$$\sigma_{u_0} = \sigma_{p_0} \quad (6.9)$$

From equation (6.7), (6.8) and (6.9)

$$\sigma_{f_0}^* = K_\sigma \left[ \sigma_\infty - (\sigma_\infty - \sigma_y) \exp \left\{ -C \varepsilon_f^n \right\} \right] \quad (6.10)$$

### 6.3.2 Case II: Material Containing Extreme Size Pore

Deformation behavior in region away from the plane containing pore can be written as follows (Figure 6.1b):

$$1 - \left( \frac{\sigma_u - \sigma_y}{\sigma_\infty - \sigma_y} \right) = \exp \left\{ -C \varepsilon_u^n \right\} \quad (6.11)$$

where  $\sigma_u$  and  $\varepsilon_u$  correspond to stress and strain, respectively, in the region away from the plane of the extreme-sized pore.

In this case, local fracture initiation and necking will occur around the extreme-sized pore. The fracture strain, therefore, can be related to the stress on the pore-containing plane as follows:

$$\sigma_p = \sigma_\infty - (\sigma_\infty - \sigma_y) \exp \left\{ -C \varepsilon_f^n \right\} \quad (6.12)$$

where  $\sigma_p$  is stress in the plane containing the extreme-sized pore.

The stress at the tip of the extreme-sized pore ( $\sigma_f^*$ ) can be written as follows:

$$\sigma_f^* = K_\sigma \sigma_u \quad (6.13)$$

where,  $K_\sigma$  is stress concentration factor due to the extreme-pore.

Here,  $\sigma_p$  is related to stress in the region away from pore ( $\sigma_u$ ) as follows:

$$\sigma_u = (1 - A_f) \sigma_p \quad (6.14)$$

where  $A_f$  is area fraction of extreme-sized pore.

From equation (6.12), (6.13) and (6.14)

$$\sigma_f^* = (1 - A_f) K_\sigma \left[ \sigma_\infty - (\sigma_\infty - \sigma_y) \exp \left\{ -C \varepsilon_f^n \right\} \right] \quad (6.15)$$

Now, uniform strain due to presence of extreme-sized pore can be obtained by dividing equation (6.6) by equation (6.11),

$$\varepsilon_u = \left( \varepsilon_{u_0}^n - \frac{1}{C} \ln \left[ \frac{\sigma_\infty - \sigma_u}{\sigma_\infty - \sigma_{u_0}} \right] \right)^{1/n} \quad (6.16)$$

### 6.3.3 Fracture Conditions

When the uniform strain of a specimen with infinitesimally small pores is equal to fracture strain, i.e.,

$$\varepsilon_{u_0} = \varepsilon_f \quad (6.17)$$

and the uniform stress is equal to the local fracture stress in both conditions, i.e.,



$$\sigma_{u_0} = \sigma_{f_0}^* \quad (6.18)$$

$$\sigma_u = \sigma_f^* \quad (6.19)$$

substituting fracture conditions in Eq. (6.16) leads to

$$\varepsilon_u = \left( \varepsilon_f^n - \frac{1}{C} \ln \left[ \frac{\sigma_\infty - (1 - A_p) K_\sigma \left\{ \sigma_\infty - (\sigma_\infty - \sigma_y) \exp \{ - C \varepsilon_f^n \} \right\}}{\sigma_\infty - K_\sigma \left\{ \sigma_\infty - (\sigma_\infty - \sigma_y) \exp \{ - C \varepsilon_f^n \} \right\}} \right] \right)^{1/n} \quad (6.20)$$

It can be seen that the relationship is developed in terms of the strain-hardening characteristics of the material and that when the extreme-sized is zero, the fracture strain of material is recovered.

#### 6.4 Stress Concentration Factor

Beyond the elastic limit, the effective stress and strain concentration factor can be given by Neuber's rule [19]. According to Neuber, the effective stress and strain concentration factor is related as follows:

$$K_t = (K_\sigma K_\varepsilon)^{\frac{1}{2}} \quad (6.21)$$

where the theoretical elastic concentration factor ( $K_t$ ) depends on the geometry and dimension of the notch.

From the definition, the effective stress concentration factor,  $K_\sigma = \frac{\sigma_{\max}}{\sigma_{nom}}$ , and the

effective strain concentration factor,  $K_\varepsilon = \frac{\varepsilon_{\max}}{\varepsilon_{nom}}$ , where  $\sigma_{\max}$  and  $\sigma_{nom}$  are stresses at

notch and nominal stress respectively,  $\varepsilon_{\max}$  and  $\varepsilon_{nom}$  are strain at notch and nominal strain respectively.

The stress concentration factor,  $K_{\sigma}$ , can be determined by solving Eq. (6.21) and the appropriate stress-strain relation. Papirno [20] developed the analytical solution to determine the effective stress concentration factor in terms of strain-hardening exponent,  $n$ , and the elastic concentration factor,  $K_t$ . When notch deforms plastically, the stress concentration factor ( $K_{\sigma}$ ) is given as follows [20]:

$$K_{\sigma} = K_t^{2-2n} \quad (6.22)$$

where  $n$  is the hardening parameter, which can be found from the stress-strain curve of the material. A range of  $K_t$  values based on the geometry and dimensions of the notch is reported in the literature.

## 6.5 Comparison with Experimental Data

The predictions of the tensile ductility behavior with the size of the crack-initiating extreme-sized pore from Equation (6.20) are evaluated against the experimental data from the literature for cast aluminum alloys and powder metallurgy (PM) Ti-6Al-4V alloy in Figure 6.2(b-d). In making this assessment, only tensile ductility data are considered where authors have specifically reported the fracture initiates from a large pore. The predicted tensile ductility with the size of the crack-initiating large pore in the figures was generated using the parameters given in Table 1. The hardening parameters ( $n$  and  $C$  in Eq. (6.20)) given in Table 1 were obtained by fitting the experimental stress-strain curve using the voce hardening relationship (Eq.(6.5)). It was assumed the

extreme-sized pores were in an ellipsoidal shape. The  $K_t$  values for ellipsoidal cavities under tensile loading are calculated and reported in the literature [21]. Kubicki [22] studied the stress concentration of pores in sintered-materials and concluded that the  $K_t$  values for most of the pores vary in the range of 2-5. The experimental data from the literature were fit by varying  $K_t$  values between 2-5.

For tensile behavior were obtained by varying the  $K_t$  values. It is found that, in the work of Surrappa et al. [13], the elastic concentration factor due to the extreme-sized pore varies from 2.05-2.85. In Teng et al. [18],  $K_t$  varies between 3.10-3.77, while in the work of Kumar et al. [15],  $K_t$  ranged from 2.85 to 3.03.

Figure 6.2(a) shows the true stress-true strain curve of three different materials: cast Al-7Si-0.3Mg alloy [13], aluminum low pressure die casting [18], and PM Ti-6Al-4V alloy [15], published in the literature. These experimental stress-strain curves were quite accurately reproduced using the Voce relationship using the  $n$  and  $C$  values given in Table 6.1.

Figure 6.2(b)-(d) presents the comparison of the experimental data for cast aluminum alloys from Surappa et al. and Teng et al., and for the PM Ti-6Al-4V alloy from Kumar et al. along with the prediction from Eq. (6.20). It can be seen that the present equation provides an excellent description between the upper and lower bound of the variation in ductility, with the size of the crack-initiating large pore in porous materials. Hence, it is clear that there is a unique relationship between the size of the pore and the tensile ductility exists. The present study established a power function between the tensile ductility and the size of the crack-initiation pore, contrary to a linear function suggested in previous studies [16,18].

Thus, in a porous material, the uniform strain will be limited by fracture initiation at the large pore and the necking of the section containing that pore. Therefore, the macroscopic uniform tensile fracture strain of a porous material corresponds to the deformation condition that is limited by the local fracture initiation and necking around a large pore. Eq. (6.20) suggests that the dependence of tensile ductility on pore size can be represented by the materials' hardening parameters and the stress concentration factor.

### **6.6 Effect of Strain Hardening on the Prediction of Tensile Ductility**

As discussed in Section 6.2, it has been shown that the level of tensile ductility achieved when a large pore is present is strongly dictated by the strain-hardening characteristics of the materials. The mathematical expressions are generally used to describe the strain-hardening characteristics of metallic materials. These expressions relate true stress ( $\sigma$ ) and true strain ( $\epsilon$ ) using certain parameters. These relations are known as strain-hardening laws. Among various relations, voce equation has attracted more attention due to its sound interpretation of stress-strain curve [23,24]. The voce relationship is given as Eq. (6.5). The parameters  $n$  and  $C$  in the equation are empirical constants, which describe the strain hardening behavior and the shape of the stress-strain curve. The value of ' $n$ ' in Eq. (6.5) is usually lying between 0 and 1. The stress-strain curve predicted using the voce relationship for cast aluminum alloys from the work of Surrapa et al. with various  $n$  values is shown in Figure 6.3(a). The higher the value of  $n$ , the more pronounced is the strain-hardening characteristic of the materials. For cast aluminum alloy [13], the characteristic strain-hardening behavior is predicted with  $n=0.4$  in the voce equation.

Now, three different regions of stresses were identified in the present model. The stress next to the pore is higher, followed by the stress in the plane containing the pore and the uniform section of the samples. The corresponding strains will depend on the strain-hardening characteristics of the sample. As shown in Figure 6.3(a), with decreasing 'n' values, the stress-strain curve flattens, i.e., lower strain hardening of the materials with decreasing 'n'. Thus, materials with lower strain-hardening characteristics can cause a large strain concentration near the pore compared to the strain in the uniform section. Figure 6.3(b) shows the predicted variation in tensile ductility of cast aluminum alloys [13] with the pore size for various strain-hardening characteristics (n values). It is evident that the effect of pore size diminishes with increasing strain hardening in the materials. For example, a significant reduction in elongation from ~ 16% to ~ 1% can be observed for  $n=0.3$ , while for  $n=0.5$  a reduction from ~ 16% to ~ 13% can be seen when the pore size increases from 0 to 2 mm. A large strain concentration can occur in the material next to the pore, even at a low stress-concentration factor, in the low strain hardening materials. Thus, a large difference in the strain in the pore vicinity and the uniform section can be observed. Material in the pore vicinity can reach to fracture strain even when the strain in the uniform section is very low, leading to a localized fracture initiation in the pore vicinity and limiting the overall elongation of the materials. Therefore, it can be argued that the decrease in ductility due to the presence of the large pore is sensitive to the strain-hardening characteristics of the materials.

## **6.7 Conclusion**

A universal function relating the tensile ductility of the material to the pore size has been established for a wide spectrum of materials. A simple power function that relates these two variables has been found to express this relationship fairly accurately. It was found that the ductility in the presence of the pore is highly sensitive to the strain-hardening characteristics of materials. Higher strain hardening rates of materials manifest a moderate effect on tensile ductility due to the presence of extreme-sized pores.

Table 6.1. Parameters used for the prediction of pore size effect on the tensile ductility of cast and PM alloys

Reference data	Hardening parameter		$\sigma_Y$ (MPa)	Fracture strain, $\varepsilon_f$	Elastic concentration factor, $K_t$		
	n	C			Upper bound	Fitting data	Lower bound
Surappa et al. [13]	0.42	0.26	210	0.160	2.05	2.50	2.85
Teng et al. [18]	0.43	0.29	170	0.166	3.45	3.60	3.77
Kumar et al. [15]	0.61	0.45	1016	0.130	2.85	2.98	3.03

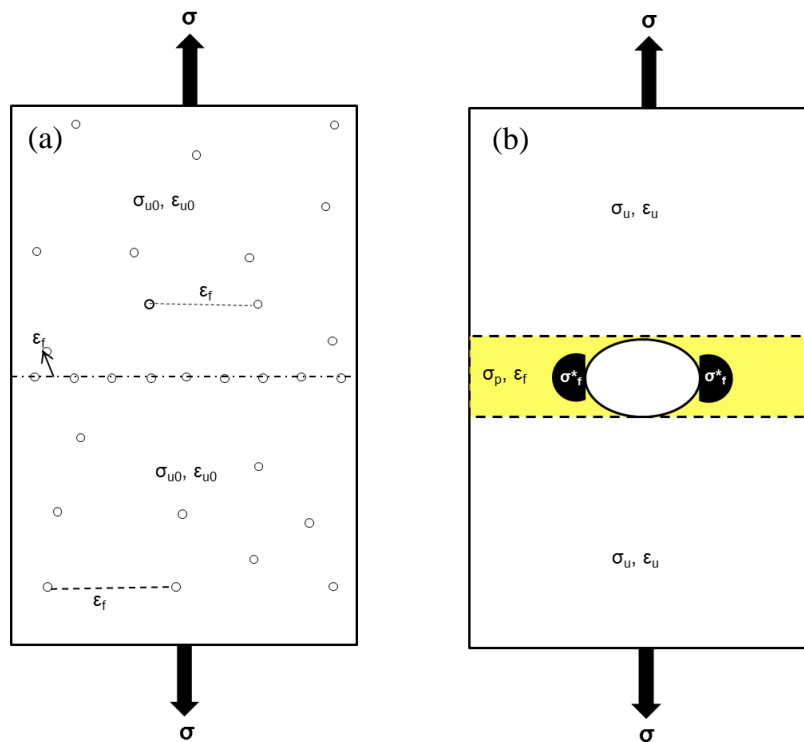


Figure 6.1 Schematic diagram of strain distribution in (a) sample containing uniformly distributed small pores, and (b) a sample containing a large pore, under tensile loading



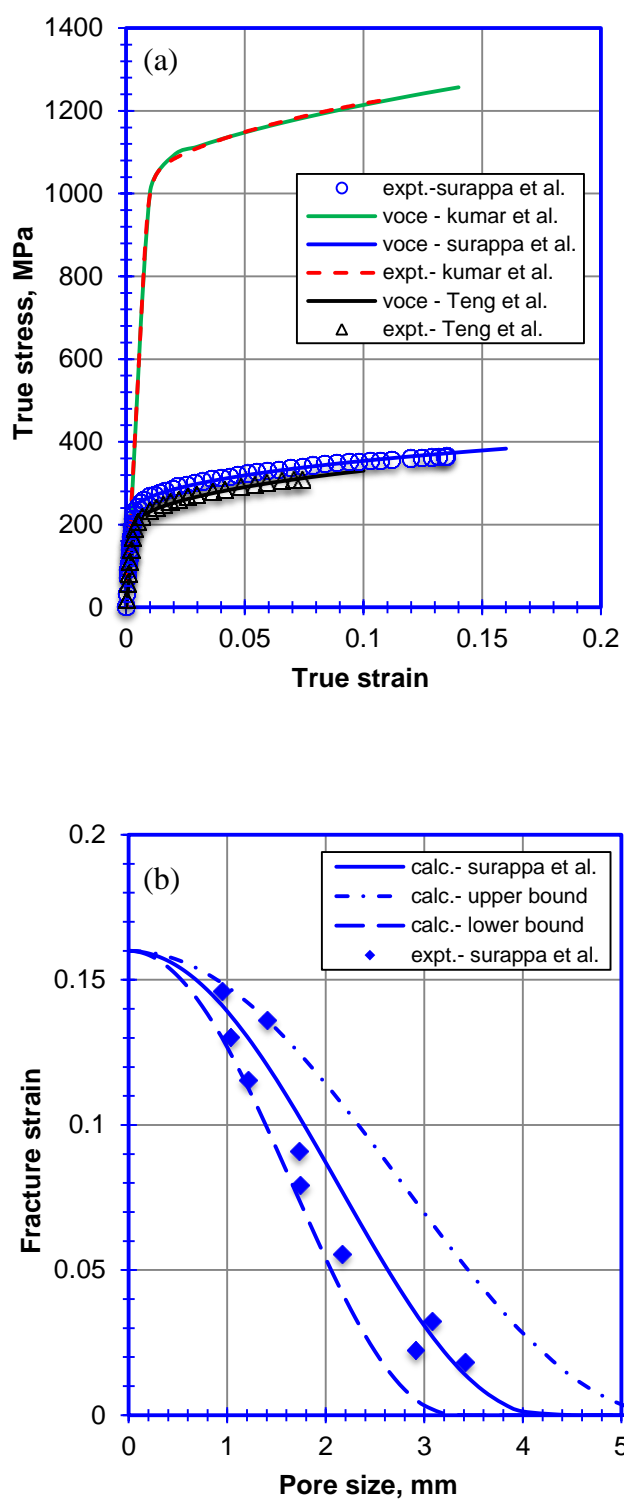


Figure 6.2 Prediction of experimental data (a) shows true stress and true strain curve produced using Voce relation (Eq.3), The predicted strain with the experimental data of (b) cast Al-7Si-0.3Mg alloy [13] (c) low pressure die cast [18] aluminum (d) PM Ti-6Al-4V alloy [15]

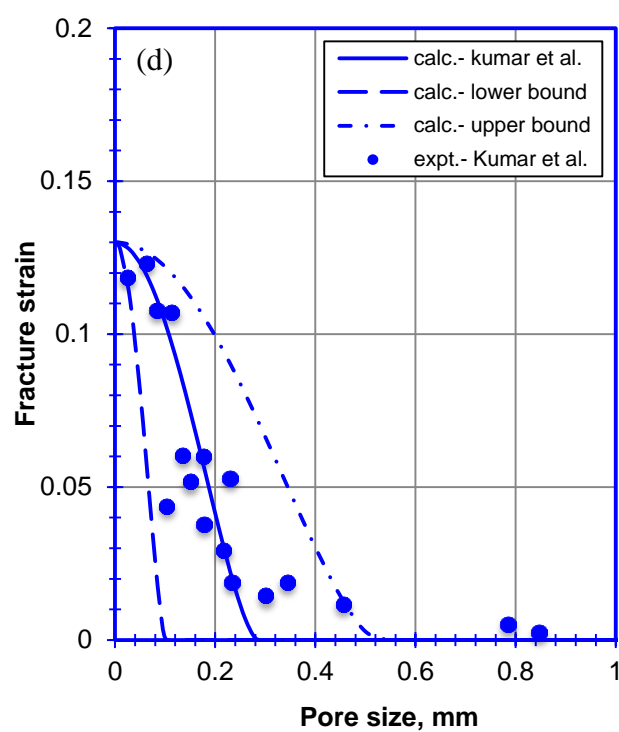
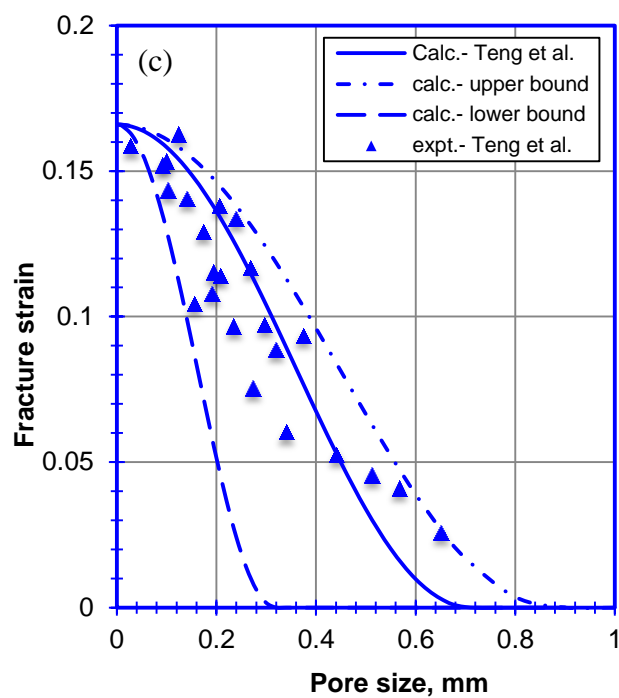


Figure 6.2 Continued

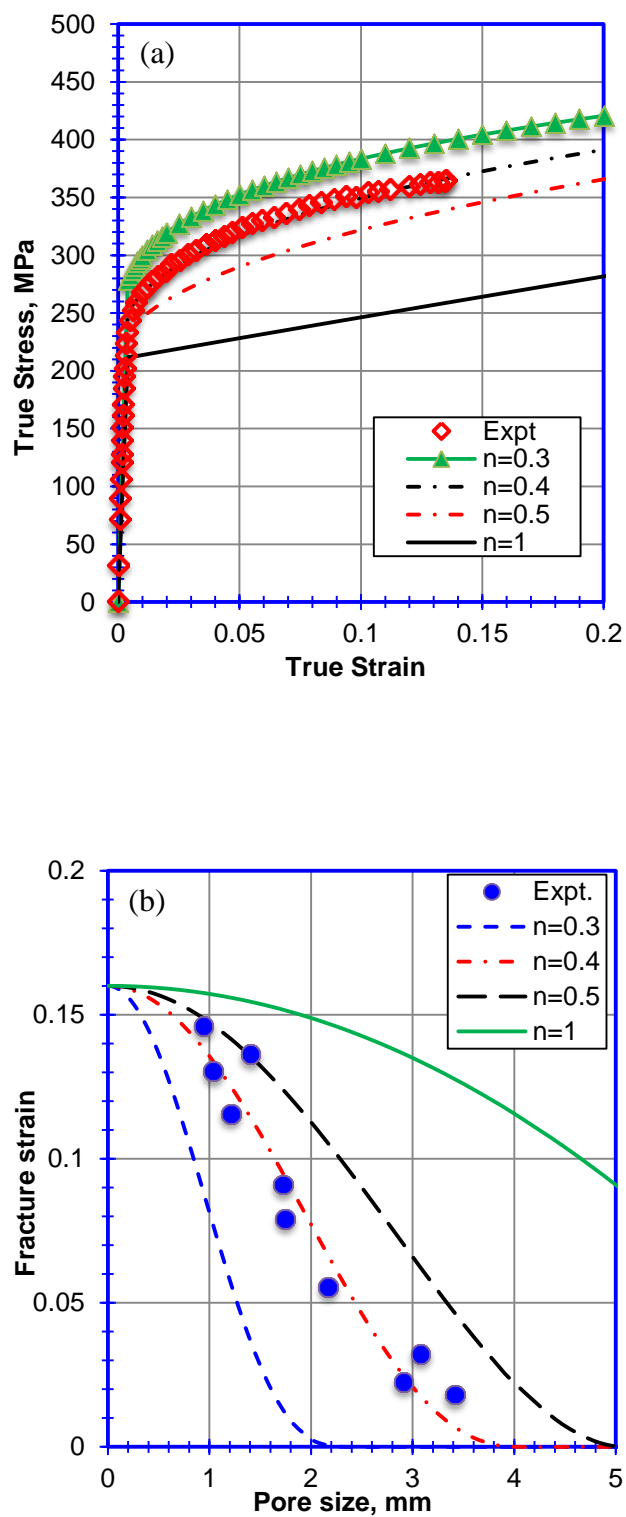


Figure 6.3 Shows (a) Empirical stress-strain curve obtained using voce relation (b) Predicted tensile behavior with the pore size for different values of  $n$ , along with experimental data for cast Al-7Si-0.3Mg alloy [13]

## 6.8 References

- [1] S.G. Lee, G.R. Patel, A.M. Gokhale, A. Sreeranganathan, M.F. Horstemeyer, Variability in the tensile ductility of high-pressure die-cast AM50 Mg-alloy, *Scr. Mater.* 53 (2005) 851–856.
- [2] S.G. Lee, G.R. Patel, A.M. Gokhale, A. Sreeranganathan, M.F. Horstemeyer, Quantitative fractographic analysis of variability in the tensile ductility of high-pressure die-cast AE44 Mg-alloy, *Mater. Sci. Eng. A.* 427 (2006) 255–262.
- [3] R.J. Bourcier, D.A. Koss, R.E. Smelser, O. Richmond, The influence of porosity on the deformation and fracture of alloys, *Acta Metall.* 34 (1986) 2443–2453. doi:10.1016/0001-6160(86)90147-1.
- [4] A.M. Samuel, F.H. Samuel, A metallographic study of porosity and fracture behavior in relation to the tensile properties in 319.2 end chill castings, *Metall. Mater. Trans. A.* 26 (1995) 2359–2372. doi:10.1007/BF02671250.
- [5] B. Hariprashad, T.H. Courtney, J.K. Lee, Porosity and tensile ductility in Al-Zn alloys, *Metall. Trans. A.* 19 (1988) 517–526. doi:10.1007/BF02649266.
- [6] G.W. Mugica, D.O. Tovio, J.C. Cuyas, A.C. González, Effect of porosity on the tensile properties of low ductility aluminum alloys, *Mater. Res.* 7 (2004) 221–229. doi:10.1590/S1516-14392004000200002.
- [7] R.J. Shore, R.B. McCauley, Effects of Porosity on High Strength Aluminum 7039, 1970.
- [8] N. Chawla, X. Deng, Microstructure and mechanical behavior of porous sintered steels, *Mater. Sci. Eng. A.* 390 (2005) 98–112. doi:10.1016/j.msea.2004.08.046.
- [9] A.M. Gokhale, G.R. Patel, Origins of variability in the fracture-related mechanical properties of a tilt-pour-permanent-mold cast Al-alloy, *Scr. Mater.* 52 (2005) 237–241. doi:10.1016/j.scriptamat.2004.09.011.
- [10] R. Becker, The effect of porosity distribution on ductile failure, *J. Mech. Phys. Solids.* 35 (1987) 577–599.
- [11] C.H. Cáceres, On the effect of macroporosity on the tensile properties of the Al-7%Si-0.4%Mg casting alloy, *Scr. Metall. Mater.* 32 (1995) 1851–1856. doi:10.1016/0956-716X(95)00031-P.
- [12] C.H. Cáceres, B.I. Selling, Casting defects and the tensile properties of an AlSiMg alloy, *Mater. Sci. Eng. A.* 220 (1996) 109–116. doi:10.1016/S0921-5093(96)10433-0.
- [13] M.K. Surappa, E. Blank, J.C. Jaquet, Effect of macro-porosity on the strength and ductility of cast Al-7Si-0.3Mg alloy, *Scr. Metall.* 20 (1986) 1281–1286.

doi:10.1016/0036-9748(86)90049-9.

- [14] P. Kumar, K.S. Ravi Chandran, A quantitative relationship to predict the effect of Extreme-sized pores on Tensile Ductility of Powder Metallurgy Ti-6Al-4V alloy, in: Titanium-2015, The Minerals, Metals and Materials Society, San Diego, CA, 2015.
- [15] P. Kumar, K.S. Ravi Chandran, F. Cao, M. Koopman, Z.Z. Fang, The Nature of Tensile Ductility as Controlled by Extreme-Sized Pores in Powder Metallurgy Ti-6Al-4V Alloy, *Metall. Mater. Trans. A.* (2016). doi:10.1007/s11661-016-3419-5.
- [16] H. Mae, X. Teng, Y. Bai, T. Wierzbicki, Relationships between Material Ductility and Characteristic Size of Porosity Correlated before/after Testing of a Cast Aluminum Alloy, *J. Solid Mech. Mater. Eng.* 2 (2008) 924–942. doi:10.1299/jmmp.2.924.
- [17] K.-F. Nilsson, D. Blagoeva, P. Moretto, An experimental and numerical analysis to correlate variation in ductility to defects and microstructure in ductile cast iron components, *Eng. Fract. Mech.* 73 (2006) 1133–1157.
- [18] X. Teng, H. Mae, Y. Bai, T. Wierzbicki, Pore size and fracture ductility of aluminum low pressure die casting, *Eng. Fract. Mech.* 76 (2009) 983–996. doi:10.1016/j.engfracmech.2009.01.001.
- [19] H. Neuber, Theory of stress concentration for shear-strained prismatical bodies with arbitrary nonlinear stress-strain law, *J. Appl. Mech.* 28 (1961) 544–550.
- [20] R. Papirno, Plastic concentration factors in flat notched specimen of AISI 4340 steel, 1970.
- [21] T.J. Griffiths, R. Davies, M.B. Bassett, Analytical Study of Effects of Pore Geometry on Tensile Strength of Porous Materials, *Powder Metall.* 22 (1979) 119–123. doi:10.1179/pom.1979.22.3.119.
- [22] B. Kubicki, Stress Concentration at Pores in Sintered Materials, *Powder Metall.* 38 (1995) 295–298. doi:10.1179/pom.1995.38.4.295.
- [23] G. Sainath, B.K. Choudhary, J. Christopher, E. Isaac Samuel, M.D. Mathew, Applicability of Voce equation for tensile flow and work hardening behaviour of P92 ferritic steel, *Int. J. Press. Vessel. Pip.* 132–133 (2015) 1–9. doi:10.1016/j.ijpvp.2015.05.004.
- [24] H.J. Kleemola, M.A. Nieminen, On the strain-hardening parameters of metals, *Metall. Trans.* 5 (1974) 1863–1866. doi:10.1007/BF02644152.

## **CHAPTER 7**

### **ACCELERATED SINTERING OF POWDER METALLURGY**

#### **TI-6AL-4V ALLOY BY REPEATED PHASE**

#### **TRANSFORMATION INDUCED BY**

#### **THERMAL CYCLING**

(Manuscript in preparation)

## 7.1 Introduction

Despite an excellent combination of structural properties [1,2], the use of titanium is restricted to high-end engineering applications such as aerospace, medical, and chemical due to cost limitations. Powder metallurgy (PM) is one of the processes that are generally used to make titanium components in net-net shape configuration in order to reduce the total cost [3–5]. Presence of residual porosity in the PM alloy, however, significantly reduces the mechanical properties of the alloy compared to the traditional wrought component.

It is now well accepted that use of  $\text{TiH}_2$  can increase the densification processes, leading to enhanced density of the titanium alloy [6–8]. Densities more than 98% theoretical density have been reported for Ti-6Al-4V alloy made using  $\text{TiH}_2$ . Joshi et al. [9], however, reported a much lower theoretical density of ~ 96% of PM Ti-6Al-4V alloy by vacuum sintering of blended  $\text{TiH}_2$ + Al-V master alloy in the  $\beta$ -phase region. Densification close to theoretical density (>99%) was achieved by mechanical deformation using hot rolling. Hence, to achieve full densification of the titanium alloy, additional processing methods such as thermo-mechanical processing are required and have been used in previous work [10–12]. Thermomechanical processing beyond the sintering step can lead to processing complexity and high cost.

During sintering, the densification of metallic powder at elevated temperature is controlled by time-dependent deformation mechanisms such as diffusion of individual powder in contact [13]. Because of the sluggish diffusion, sintering kinetics during isothermal sintering is limited. Thus, any other deformation mechanism operating in the metals can be utilized for powder densification, in principle.

It has been shown that a significant increase in densification rate in metal powders can be achieved by cyclic phase transformation [13–18]. For example, Kohara [19] reported substantial improvement in sintering kinetics in iron powder under repetitive phase transformation through  $\alpha$ - $\gamma$  phase under compressive load. Schuh et al. [14] carried out experiments on sintering behavior of CP Ti powder under both isothermal and cyclic phase transformation thermal conditions. The densification during cyclic sintering across the  $\beta$  transus temperature occurred more rapidly than in the isothermal process, despite the average temperature in cyclic condition being 60°C lower than the isothermal condition. Similar phenomena of enhanced densification rate for pre-alloyed (PA) Ti-6Al-4V alloy powder due to phase-transformation-induced plasticity are reported [17]. The enhanced densification process during cyclic sintering was attributed to the irreversible strain produced due to the phase transformation. Leriche et al. [20] calculated the contribution from phase transformation-mismatch plasticity during the first and second cycles in densification process of Ti-6Al-4V alloy powder and reported that it was higher than the contribution from the diffusional mechanism. All the above studies indicating the improved densification kinetics by cyclic sintering across allotropic transformation temperature used external pressure during sintering. In general, using pressure-assisted sintering is a limiting factor in the production of PM components.

The studies on the effect of repeated allotropic transformation on densification during pressure-less sintering of metal powder are limited in the literature [21–23]. Few studies have reported an enhanced sintering kinetics due to repeated allotropic change during sintering [22]. However, a study carried out by Powell [23] indicates no improvement in properties due to cyclic phase transformation in iron and titanium. Thus, experimental



results reported in the literature are not consistent and not explored in detail. Sarma et al. [24] reported that diffusion kinetics can be enhanced using thermal cyclic treatment across the phase transformation in titanium. It is also noticed that transition metals such as titanium, zirconium, and hafnium show anomalous diffusion behavior, i.e., elevated diffusion rates close to the transition temperature relative to the normal Arrhenius-type behavior [25]. The “anomalous diffusion” behavior near phase transition is believed to have a positive effect on densification behavior in these metals when sintering at the transition temperature.

In the present study, we have explored the possibilities of increased densification behavior of PM Ti-6Al-4V alloy by a systematic study of effect of thermal cyclic sintering. We have demonstrated that continuous phase reversals due to thermal cycling help in closing the pores during sintering of PM Ti-6Al-4V alloy. Isothermal sintering of PM Ti-6Al-4V alloy close to phase transformation temperature shows better densification behavior. The microstructure and tensile and fatigue properties of PM Ti-6Al-4V alloy sintered by thermal cycling are examined and compared with that isothermally sintered at phase transition temperature (1010°C).

## **7.2 Experimental Procedure**

TiH<sub>2</sub> powders (-325 mesh) were blended with a proportion of 60Al/40V master alloy (-400 mesh) to yield a composition of Ti-6Al-4V alloy. The blended powders were consolidated into billets of cylindrical shape 90 mm in length and 13 mm in diameter using cold-isostatic pressing (CIP) at a pressure of 350 MPa. The resulting billets were vacuum sintered following both cyclic variation in temperature and at constant

temperature (isothermal). In the cyclic sintering experiment, two sets of experiments were devised. The limit temperatures of one experiment were 1000 and 1020°C (condition 1), while the other sets' limits were 990 and 1030°C (condition 2). In both the cyclic conditions, the mean temperature was 1010°C, which is the phase transition temperature of the present alloy. Thus, the lower and upper temperatures for both thermal cycling conditions were in the ( $\alpha+\beta$ ) and  $\beta$  phase field, respectively. Thermal cycles up to 192 cycles were performed for sintering the PM Ti-6Al-4V alloy. It takes about 1.7 and 3.4 minutes to complete one cycle for condition 1 and condition 2, respectively. In the isothermal sintering experiment, the temperature of the billets was raised to the phase transition temperature of the Ti-6Al-4V alloy (1010°C) at a rate of 25°C/min from room temperature and maintained constant for various time lengths (decided based on the time taken during thermal cycles during cycling sintering) and cooled to room temperature at a rate of 25°C/min. Throughout the sintering experiments, the samples were in a high vacuum of  $10^{-5}$  torr. The complete processing steps for both thermal cyclic sintering and isothermal sintering are shown in Figure 7.1.

Chemical compositions of the samples were determined at Aston Metallurgical Laboratory, IL, USA following ASTM E1447 and E1409. Densities of as-sintered samples were measured using a Micromeritics pycnometer model AccuPycII. As-sintered samples were sectioned and mounted. Mounted samples were polished following standard metallographic procedure for microstructure analysis. Polished samples were etched using Kroll's agent to reveal the microstructure. An optical microscope was used for microstructure analysis. Tensile samples were machined from as-sintered cylindrical billet following the ASTM E8 standard (gage length: 31.75 mm and gage diameter: 6.35

mm). Tensile tests were performed at ambient temperature and pressure with a strain rate of  $0.0002 \text{ s}^{-1}$ . The displacement in the gage section with a function of load was recorded using an extensometer. Values of yield and tensile strength as well as percent elongations were determined from the stress-strain curves. For fatigue tests, the samples were machined in cylindrical shape with a total length of 76.2 mm and a gage length of 12.7 mm. The diameter of the gage section was 6.35 mm. The gage sections were mirror polished using silicon carbide, followed by 1- $\mu\text{m}$  alumina suspension to mitigate surface effects. The tests were performed under load control and tension-tension condition with a cyclic frequency of 35 Hz (sine wave) at the stress ratio ( $\sigma_{\min}/\sigma_{\max}$ ) of 0.1 in laboratory atmosphere at the room temperature. The fatigue fracture surfaces were examined in scanning electron microscope (SEM) to determine the characteristics of fatigue failure

### 7.3 Results and Discussion

#### 7.3.1 Thermal Cycling and Isothermal Densification

The chemical composition of the dehydrogenated samples after 5.4 hours of sintering is given in Table 7.1. All samples processed with different sintering conditions showed complete dehydrogenation, and hydrogen level was  $< 15\text{ppm}$ . Since in all samples were made using an identical powder blend, similar chemical composition can be assumed to exist in all the samples. The average sintered density values of the alloy obtained by both cyclic condition and isothermal condition are given in Table 7.2.

The densification behavior of both thermal cycling and isothermal sintering condition are compared in Figure 7.2. Time in thermal cyclic condition refers to the total time samples were exposed for cyclic treatment, while in isothermal condition it indicates hold

time. The density of the alloy increased while the densification rate decreases steadily with time in all sintering conditions. Also, it can be observed that the densification behavior is similar when sintering up to 3 hours, which results in achieving ~ 96% relative density. Sintering beyond 3 hours (above ~96% relative density), the densification curve diverges. Sintering close to the phase transition temperature ( $1010^{\circ}\text{C}$ ) both in cyclic condition ( $1000\text{-}1020^{\circ}\text{C}$ ) and isothermal sintering leads to increased densification rate compared to the cyclic sintering away from the transition temperature ( $990\text{-}1030^{\circ}\text{C}$ ), despite the same average temperature.

Figure 7.3 shows a schematic diagram indicating the progress of sintering in the samples. Initial compacted samples consist of mixture of hydrogenated titanium powder and Al-V master alloy. Hydrogen in Ti-6Al-4V alloy reduces phase transition temperature to about  $850^{\circ}\text{C}$  [26,27]. Therefore, initial sintering in all sintering conditions occurs in Ti ( $\beta$ ) phase region, which is exclusively controlled by the diffusion processes. With time, hydrogen depletes due to continuous egress of hydrogen from the samples during sintering, as shown in Figure 7.3. Reduction in hydrogen shifts the transition temperature up close to the phase transition temperature ( $1010^{\circ}\text{C}$ ) of Ti-6Al-4V alloy. However, the transition temperature in the samples is controlled by the dissolution of Al-V master alloy powder in the titanium matrix. Nevertheless, the increase in transition temperature should follow from the surface to the center (Figure 7.3). Hydrogen-depleted Ti-6Al-4V regions in the samples go through the repeated phase transition while the hydrogen-rich regions are still sintering in the  $\beta$  phase region. It was found that complete hydrogen removal take place in ~ 2 hrs. Microstructure homogenization completes in ~ 3 hrs of sintering in all sintering conditions considered (since the average sintering

temperature is the same in all conditions), which will be discussed in detail in the microstructure section. Therefore, most of the sintering happens in  $\beta$  phase during initial sintering, thus same sintering mechanisms should follow in all conditions. The similar densification behavior in all the sintering conditions confirms that the same densification mechanism occurred during the initial  $\sim 3$  hours of sintering.

Deviation in the densification behavior was observed after  $\sim 3$  hrs of sintering. For example, at a given sintering time of  $\sim 5.5$  hrs, the density observed in the case of 990-1030°C cyclic sintering was  $\sim 97\%$ , while the cyclic sintering in “condition 1” (1000-1020°C) and isothermal sintering yield  $\sim 97.5\%$  and  $\sim 98\%$  densities, respectively. This indicates that additional densification mechanisms are also operative during sintering beyond 3 hrs or after  $\sim 96\%$  densification.

Note that in the present study, PM Ti-6Al-4V alloy undergoes continuous phase reversals ( $\alpha+\beta \leftrightarrow \beta$ ) during sintering. Studies showed that phase transformation lead to volume change in the allotropic materials [17,28,29]. A specific volume change of 0.17% due to allotropic phase transformation ( $\alpha \rightarrow \beta$ ) in titanium is reported [30]. However, associated volume change in the titanium alloy due to allotropic phase transformation is one order of magnitude less than the ferrous alloys. Szkliniarz et al. [30] showed that change in volume due to phase transformation in Ti-6Al-4V alloy is heating-rate-dependent. In their study, the specific volume changes were 0.77%, 0.83%, 0.65% and 0.31% for 0.1 K/s, 1 K/s, 10 K/s and 100 K/s, respectively. The volume change decreased with increased heating rate. This can be related to the unique phase transformation behavior ( $\alpha+\beta \leftrightarrow \beta$ ) of Ti-6Al-4V alloy. The  $\alpha+\beta \rightarrow \beta$  transformation generally develops through increase of  $\beta$  phase volume as a result of migration of  $\alpha/\beta$  interface. At higher

heating rates, insufficient time limits the phase transformation process, thereby reducing associated volume change. Nevertheless, the phase transformations cause a volume change in Ti-6Al-4V alloy.

The volume change causes generation of internal strain, which can enhance the densification behavior of the materials [14,15,17,31]. Here, we saw an increase in density for the samples cyclic sintered for more than 3 hrs with the thermal cycle conditions. As conditions changed from 2 to 1, improvement in density was observed. This can be attributed to the increased number of phase transformation cycles in “condition 1”, which is twice the number of such cycles in “condition 2” for a given cyclic sintering time. However, an increase in the density due to an increased number of phase transformation cycles is not significant in the present PM Ti-6Al-4V alloy. Ye et al. [17] calculated the effective volume change due to phase reversals during the thermal (960-1020°C) cycle and reported a value of 0.41% ( $\Delta V/V=0.41\%$ ) in Ti-6Al-4V alloy. If we assume similar internal strain generated during both cycles conditions in the present study, strain increased even after doubling the number of cycles will not be significant and not enough to completely close all pores. However, the generation of strain can lead to an increase in dislocation density, which can act as a short path for diffusion, hence increased diffusion rate. Sarma et al. [24] showed the phase reversals increase the diffusion rate by studying the boron diffusion in CP-Ti. The increased diffusion rate was attributed to a short diffusion path ( $\alpha/\beta$  interfaces) created due to phase reversals. Thus, it can be argued that the increased diffusion rate due to phase reversal cause the observable increase in the density of cyclic sintered (condition 1) PM Ti-6Al-4V alloy.

Surprisingly, highest density is observed for the isothermal sintering at phase

transition temperature. It is known that titanium shows unique diffusion behavior. An upward diffusion curvature in diffusion data as the transition temperature is approached was shown earlier [32]. This is illustrated schematically in Figure 7.4. It can be seen that titanium shows Arrhenius-type diffusion behavior at high temperatures, but as the temperature approaches to a  $\beta \rightarrow \alpha$  transition temperature, it shows increased diffusion coefficient. This deviation in diffusion curve at the  $\beta \rightarrow \alpha$  transition temperature has been called anomalous diffusion behavior. The enhanced diffusivity near the transition temperature can be useful in increasing the sintering kinetics of titanium.

During the thermal cycling across the phase transition temperature, the compact was in the anomalous diffusion region for a relatively shorter period of time as compared to isothermal sintering. For example, consider cycling sintering of a sample for 96 cycles following condition 2, the total sintering time was 5.4 hrs. During thermal cycling, the sample was below the phase transition temperature for about half the sintering time (2.7 hrs). When compared to 5.4 hrs of isothermal sintering, where the sample was in the anomalous diffusion region for 5.4 hrs, the cyclic sintered sample was exposed to anomalous diffusion region for 2.7 hrs. Thus, the increased density in the isothermal condition compared to the cyclic conditions can be attributed to increased sintering kinetics due to high diffusivity in an anomalous diffusion region.

### 7.3.2 Microstructure

The optical micrographs of samples isothermally sintered in vacuum at 1010°C for various hold times are shown in Figure 7.5. The sample sintered for 0.9 hours and 1.3 hours shows master alloy particles surrounded with the titanium matrix (Figure 7.5a and

b), which indicates an incomplete dissolution of master alloy powder. With an increase in time, more of the master alloy powder dissolves in the matrix, and complete dissolution occurs around 2.7 hours of sintering, leading to a homogenous microstructure. The microstructure of the samples consists of the lamellar  $\alpha+\beta$  structure with uniform distribution of porosity. The porosity in the microstructure consists of both elongated pores and fine, rounded pores. More elongated pores and few fine, rounded pores were observed in the microstructure of the 2.7-hours-sintered sample. A significant reduction of elongated pores was observed when the sintering time was increased to 5.4 hours. Very few elongated pores were observed in the 5.4-hours-sintered sample. Almost all the pores were small in size and rounded in shape, and uniformly distributed in the microstructure (Figure 7.4c). When compared, there is not a significant change in porosity even after increasing the sintering time to 10 hours. This clearly indicates that sintering of Ti-6Al-4V alloy is nearly complete around 5.4 hours sintering at 1010°C. This is also supported by the fact that only a slight increase in density has been observed (Figure 7.2).

The microstructures of the samples sintered through three different conditions for ~ 5.4 hours are compared in Figure 7.6. All the samples showed similar microstructural characteristics, i.e., lamellar structure but porosity distribution varied in the microstructures. Uniformly distributed fine pores with few bigger pores were observed in the samples sintered isothermally and in cyclic sintering condition 1 (Figure 7.6(a&b)). When compared, a greater number of big pores was observed in the sample sintered following condition 2 (Figure 7.6c). The distribution of pore sizes determined by image analysis is shown as a frequency distribution in Figure 7.7. The distribution of pores



indicates that a majority of pores are very small in all sintering conditions, but a large number of relatively larger pores was observed for “condition 2” compared to “condition 1” and isothermal sintering (Figure 7.7). Pore size up to 30  $\mu\text{m}$  for condition 2 can be observed while condition 1 and isothermal shows a maximum pore size of 19  $\mu\text{m}$  and 17 $\mu\text{m}$  for condition 1 and isothermal sintering, respectively. Image analysis studies indicate that the average size of porosity is about 11  $\mu\text{m}$  in both isothermal and cyclic sintering “condition 1”, while a higher average pore size of about 17  $\mu\text{m}$  is observed in the sample sintered following “condition 2” for the same sintering time (5.4 hrs) and average sintering temperature (1010°C). The residual volume fraction porosity obtained from image analysis showed 1.9%, 1.2% and 1.3% for cyclic “condition 2”, “condition 1” and isothermal sintering, respectively. This means that sintering close to the phase transformation temperature can lead to a relatively lower level of porosity with relatively finer pore sizes. As discussed in section 7.3.1, the reduced porosity and the smaller average pore size in sample sintering close to the phase transition are due to accelerated sintering in the anomalous diffusion region.

### **7.3.3 Tensile Properties**

The stress-strain curves for the PM Ti-6Al-4V alloy for various processing conditions are shown in Figure 7.8. The fracture of the samples is indicated by the crosses on the curves. As expected, the yield (YS) or tensile strength (UTS) and elongation of PM Ti-6Al-4V alloy increased with an increase in sintering time. Improved tensile behavior of the alloy can be attributed to reduced porosity level in the microstructure with an increase in sintering time. Presence of porosity reduces the load bearing cross-sectional area.

Therefore, when a load is applied to the material, the effective stress is increased which leads to a reduction in yield and tensile strength [33,34]. The tensile properties of the PM Ti-6Al-4V alloy are summarized in Table 7.3. Tensile properties of the samples processed by varying processing conditions are compared in Figure 7.8. Similar to isothermal sintering, both tensile strength and ductility in terms of % elongation were found to increase with sintering time (increased density) in all sintering conditions (Figure 7.8c). It is clear that the presence of porosity introduce two factors: (i) local strain concentration and (ii) reduction in the macroscopic flow stress. Ligaments in the sintered specimen are considered as the individual miniature tensile specimen, and during tensile loading most of the deformation occurs within the narrower parts of the ligaments [35]. Therefore, maximum strain localization takes place at the shortest distance between the pores. Inhomogeneous deformation causes crack initiation at lower stress, leading to a reduction in strength and the ductility of the materials. Thus, increased tensile strength and ductility of the PM Ti-6Al-4V alloys with sintering time can be explained.

When compared, no significant difference in yield strength (YS) or tensile strength (TS) behavior in the samples processed through isothermal and cyclic sintering conditions (Figure 7.9 (a & b)) was observed. It has been shown earlier that small variation in the volume fraction porosity does not necessarily change the strength of the materials [36,37]. For example, Yan et al. [37] showed similar strength for PM Ti-6Al-4V alloy, even when the volume fraction porosity difference was about 4%. In the present study, the difference in density of a sample at a given sintering time is not significant (< 1%). Therefore, porosity in the form of their volume fraction in the bulk does not significantly affect the strength levels of the samples processed through varying sintering

conditions.

However, difference in elongation behavior between the samples processed through varying sintering conditions was observed. Similar to densification behavior, tensile elongation curve diverges after sintering for about 3 hours (Figure 7.9c). Among all sintering conditions, the isothermal sintering of PM Ti-6Al-4V alloy shows the best ductility behavior, and the reason is obvious from the densification curve (Figure 7.9c). Improvement in tensile ductility of isothermally sintered samples can only be attributed to the reduction in the amount of porosity or increased density in isothermally sintered samples.

From the present results, it can be inferred that the tensile ductility of PM Ti-6Al-4V alloy is sensitive to small changes in the amount of residual porosity, but not tensile strength. The ductility of PM Ti-6Al-4V alloy is also sensitive to size/shape of individual pores along with the residual volume fraction porosity [38,39]. Considering the sintering time of 5.4 hrs in present study, microstructure analysis showed a relatively large number of large pores was present in the microstructure of “condition 2” compared to isothermal sintered samples. The average size of the pores was about 17  $\mu\text{m}$  and 11  $\mu\text{m}$ , observed for “condition 2” sintering and isothermal sintering, respectively. It was reported that a large amount of strain intensification can occur at the single large pore/cluster. Inhomogeneous deformation around a large pore acts as a crack-initiating site during the tensile loading [33]. The amount of strain in the pore vicinity dictates the crack initiation and propagation, which limits the total macroscopic elongation. The strain in the pore vicinity depends on the size of the pore – larger pore, more strain generates in the pore vicinity. Also, a low strain hardening exponent ( $n$ ) aggravates the sensitivity of local

deformation adjacent to the discontinuities, such as pores in Ti-6Al-4V alloy [40]. Thus, the presence of relatively large volume fraction porosity and large average pore size in the microstructure can lead to large strain intensification in the material, thus limiting the elongation in PM Ti-6Al-4V alloy sintered following “condition 2”.

### 7.3.4 Fatigue Performance

The fatigue tests were performed on the samples prepared using isothermal sintering at phase transition temperature (1010°C) for 5.4 hours. The choice was made for two reasons. First, samples obtained with this condition showed better density and ductility behavior. Secondly, samples obtained from another set of sintering conditions yield density equivalent to or less than those obtained for isothermally sintered samples at 1010°C for 5.4 hrs, and fatigue performance of such samples was deemed unlikely to be superior to that achieved for later samples, owing to the similar microstructures across all conditions. Hence, the fatigue tests for samples made by condition 1 and condition 2 were not pursued. The S-N fatigue data, plotted in terms of maximum cyclic stress ( $\sigma_{\max}$ ) versus the number of cycles to failure ( $N_f$ ) for isothermal sintered Ti-6Al-4V alloy, are shown in Figure 7.10. The fatigue data of PM Ti-6Al-4V alloy from literature are also included for fatigue performance comparison. The processed samples in the present study have the same microstructure characteristics, i.e., lamellar, though their porosity levels are different. Therefore, any difference in the fatigue property will be largely due to a difference in porosity level.

Generally, the fatigue strength indicates the fatigue performance, i.e., the higher the fatigue strength, the better the fatigue performance. Here, fatigue strength is defined as

the maximum stress at which the sample withstands for  $10^7$  cycles. The fatigue strength of the PM alloy is  $\sim 300$  MPa (Figure 7.10), which is slightly better than the previous reported values for similar press and sintered alloy. The improvement is clearly evident when the data are examined at the stress level between 500 MPa and 600 MPa. In this stress range, the average fatigue life was  $10^5$  cycles, whereas the maximum reported fatigue cycle was  $10^3$  cycles [41]. Also, the low to intermediate cycle fatigue performance of the present sample is significantly higher than as reported in the literature. This significant improvement in fatigue performance can be attributed to a reduction in volume fraction porosity, and especially a reduction in crack-initiating large pores, in the samples.

The SEM fractograph of fatigue-fractured surfaces taken from high- and low-cycle specimens are shown in Figure 7.11 and Figure 7.12, respectively. It can be seen that the apparent crack initiation site is from subsurface for both high-cycle and low-cycle fatigue fracture. At higher magnification, a rough morphology with multiple facets can be seen at the fracture initiation site. This crack initiation characteristic is similar to cast/wrought alloy of similar microstructure [42–44]. No pores or inclusions were seen at the initiation site, which is typical of PM samples. The size of a facet corresponds to the size of an  $\alpha$ -colony in the microstructure. Various studies have reported the crack initiation from the facet in fatigue fracture in cast, wrought and PM Ti-6Al-4V alloy. Ferri et al. [45] studied the fatigue failure mechanism in MIM Ti-6Al-4V alloy, and reported that the large slip length of an  $\alpha$  colony can lead to dislocation pile-ups, and results in the formation of facets. A similar hypothesis was reported in the work of Cao et al. [12] - larger slip length in coarse  $\alpha$  facets requires relatively lower stress level in initiating fatigue crack.

In general, fatigue failure in PM titanium alloys is dominated by the presence of residual porosity [37,41]. The random presence of crack-initiating pores of varying size in PM titanium alloys causes a large scatter in the fatigue data. Cao et al. [46] showed the size and/or location (surface and interior) has significant effect on the fatigue life of PM Ti-6Al-4V alloy. However, the fatigue crack initiation is determined by the competition between the extreme-sized pores and the size of  $\alpha$  grain in the microstructure in PM titanium alloy. If the size of  $\alpha$  grain is larger than the pore present, the  $\alpha$  grain (or facet) will act as fatigue crack initiator in the specimen. This phenomenon of fatigue failure in PM titanium alloy is reported in a recent study [12]. The study showed that, as the residual pore decreased, facets become the dominant mechanism in initiating the fatigue crack. These facets are thought to correspond to the coarse  $\alpha$  phase region in the microstructure. A significant increase in fatigue strength (about 550 MPa) was reported by refining  $\alpha$  grains in PM Ti-6Al-4V alloy [12].

Thus, based on the above discussion, it can be concluded that the dominant failure mechanism in fatigue is due to the coarse  $\alpha$  laths in the microstructure of vacuum sintered PM Ti-6Al-4V alloy. This implies that fatigue performance of the present PM titanium alloy can be further increased by reducing  $\alpha$  colony size.

## 7.4 Conclusion

Densification of TiH<sub>2</sub>-(60Al//40Al V) blends during pressure-less sintering subjected to a constant temperature (phase-transition temperature (1010°C )) and thermal cyclic across 1010°C were investigated. The salient conclusions are:

1. Density as high as 98% of theoretical density of PM Ti-6Al-4V alloy can be

achieved with temperature about 200°C lower than conventionally used sintering temperature by thermal cycling through phase transformation of Ti-6Al-4V alloy. The densification process of powder blends is thought to be accelerated by the strain generation due to phase volume mismatch.

2. Isothermal sintering close to the phase-transition temperature (1010°C) of PM Ti-6Al-4V alloy enhances the densification process. This enhancement is attributed to the anomalously high diffusivity at the transition temperature.

3. The enhanced diffusion in anomalous diffusion temperature range is more effected in sintering of PM Ti-6Al-4V alloy than by the strain generation due to phase transformation induced by thermal cycling.

4. PM Ti-6Al-4V alloy with good ductility (~ 15%) and strength (~ 900 MPa), which is comparable to a wrought Ti-6Al-4V alloy, can be achieved by sintering close to the phase transition temperature.

5. A fatigue strength (defined at  $10^7$  cycles) of about 300 MPa can be achieved by pressing and sintering at phase transformation temperature of PM Ti-6Al-4V alloy, which is equivalent to conventional press + sinter process. However, when compared, significantly improved fatigue strength in low to intermediate cycles is achieved relative to the conventional powder metallurgical approaches using blended elements. This improvement in the fatigue performance is attributed to the elimination of large pore/pore clusters from the microstructure.

Table 7.1 Chemical composition of vacuum-sintered PM Ti-6Al-4V

<b>Composition</b>	<b>Al</b>	<b>V</b>	<b>O</b>	<b>C</b>	<b>N</b>	<b>Ti</b>
<b>Wt.%</b>	6.09	4.15	0.23	< 0.03	0.01	Balance

Table 7.2 Density of PM Ti-6Al-4V alloy obtained in three different conditions

<b>Time* (hrs.)</b>	<b>Isothermal</b>	<b>Condition 1</b>	<b>Condition 2</b>
	<b>Density (%)</b>	<b>Density (%)</b>	<b>Density (%)</b>
0.9	94.75	94.12	94.25
1.3	94.40	94.43	-
2.7	96.06	95.98	96.25
5.4	97.80	97.42	97.05
10.0	98.50	-	-
10.8	-	-	98.08

\* Time indicate total time of sintering



Table 7.3 Summary of tensile properties obtained in isothermal sintering compared with cyclic sintering of PM Ti-6Al-4V alloy

<b>Time*</b> <b>(hrs.)</b>	<b>1010°C</b>			<b>1000-1020°C</b>			<b>990-1030°C</b>		
	<b><math>\sigma_{YS}</math></b> <b>(MPa)</b>	<b><math>\sigma_{UTS}</math></b> <b>(MPa)</b>	<b>%</b> <b>El.</b>	<b><math>\sigma_{YS}</math></b> <b>(MPa)</b>	<b><math>\sigma_{UTS}</math></b> <b>(MPa)</b>	<b>%</b> <b>El.</b>	<b><math>\sigma_{YS}</math></b> <b>(MPa)</b>	<b><math>\sigma_{UTS}</math></b> <b>(MPa)</b>	<b>%</b> <b>El.</b>
0.9	674	774	6.7	662	758	5.72	680	773	6.3
1.3	696	798	7.2	710	800	7.56	-	-	-
2.7	752	850	10.5	755	854	9.74	760	852	10.8
5.4	815	908	15.0	803	907	13.6	786	885	12.7
10	833	933	16.0	-	-	-	-	-	-
10.8	-	-	-	-	-	-	816	918	14.5

\*Time indicate total time of sintering

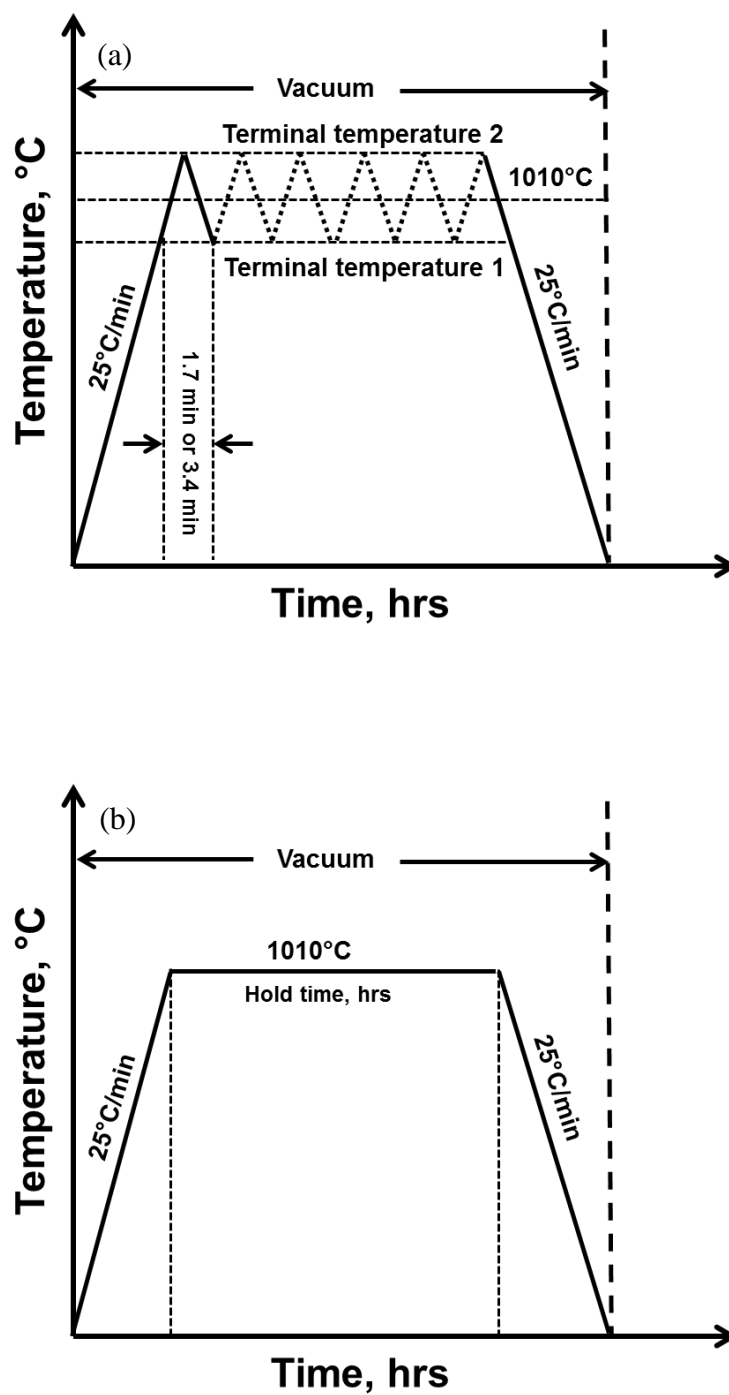


Figure. 7.1 Schematic of temperature and time profile of (a) thermal cyclic sintering and (b) isothermal sintering for making PM Ti-6Al-4V alloy

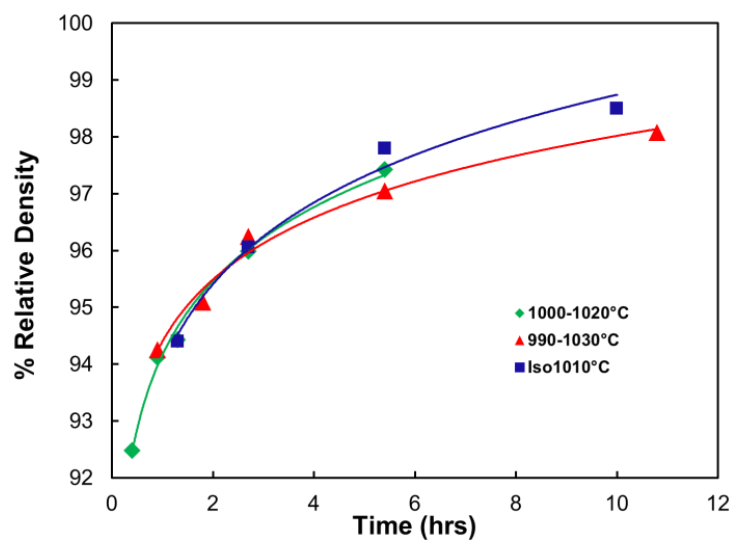


Figure 7.2 Densification curves for various sintering conditions

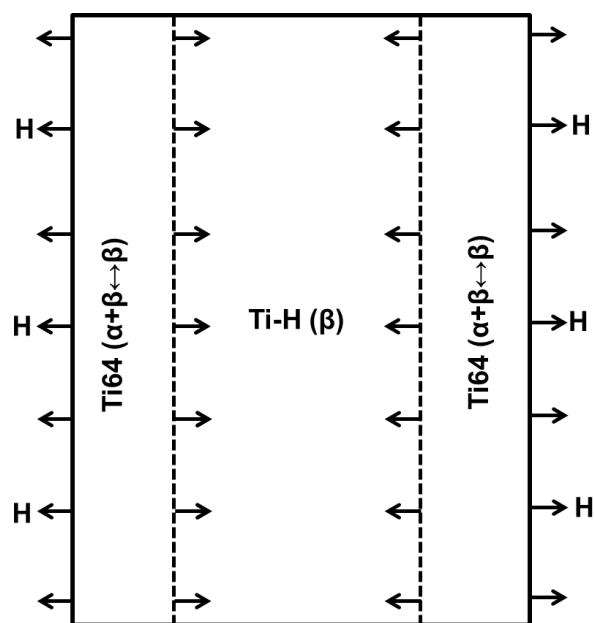


Figure 7.3 Schematic diagram indicating the progress of sintering during dehydrogenation of  $\text{TiH}_2$  powders.

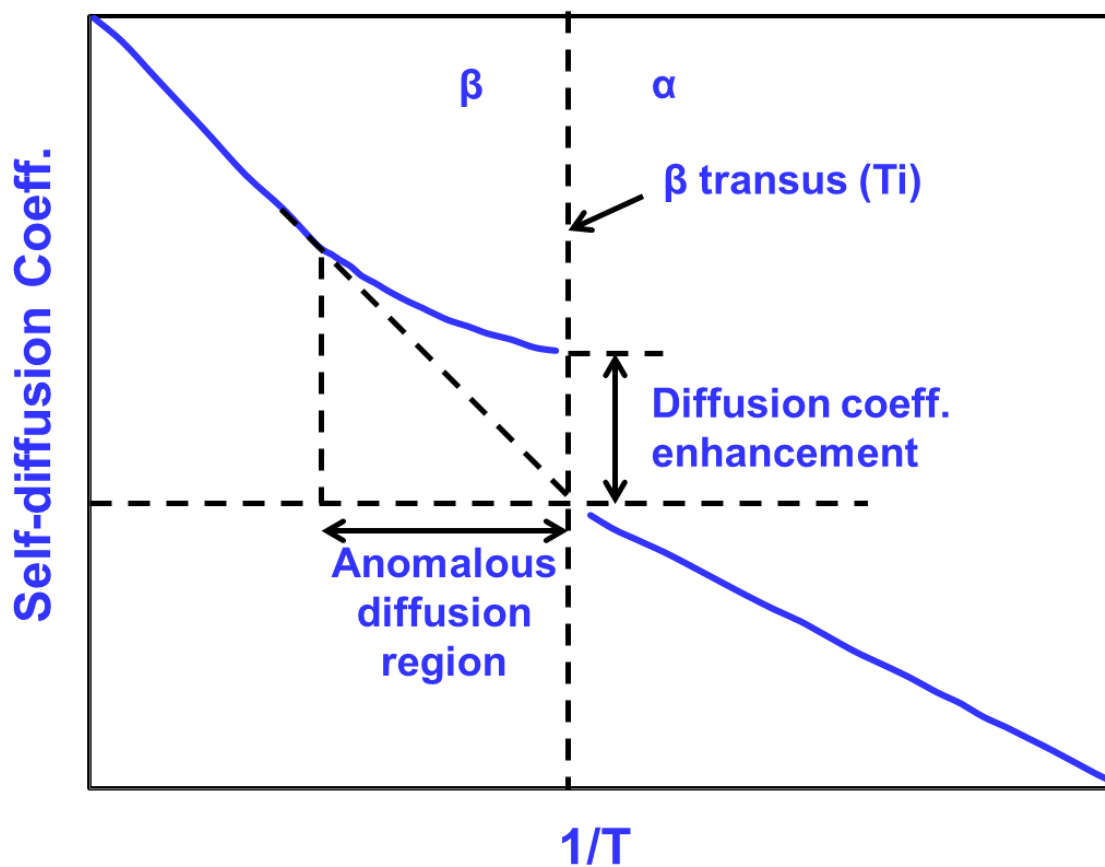


Figure 7.4 Schematic diagram illustrating the enhanced self-diffusion and the anomalous diffusion region in titanium [32]

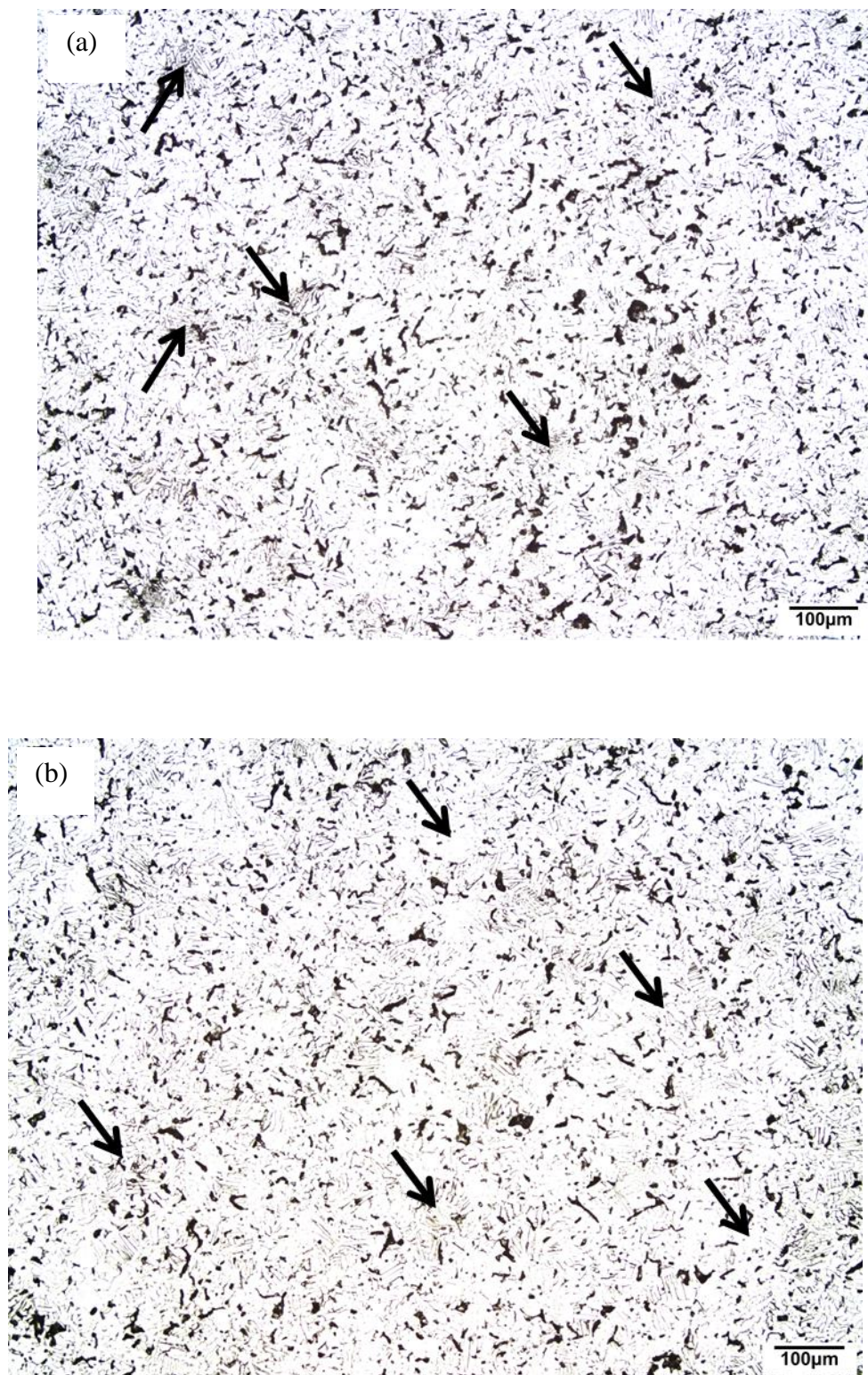


Figure 7.5 Microstructure of samples isothermally sintered at 1010°C for (a) 0.9 hours, (b) 1.3 hours (c) 2.7 hours, (d) 5.4 hours, and (e) 10 hours. Arrows in (a) and (b) indicate Al-V alloy particles



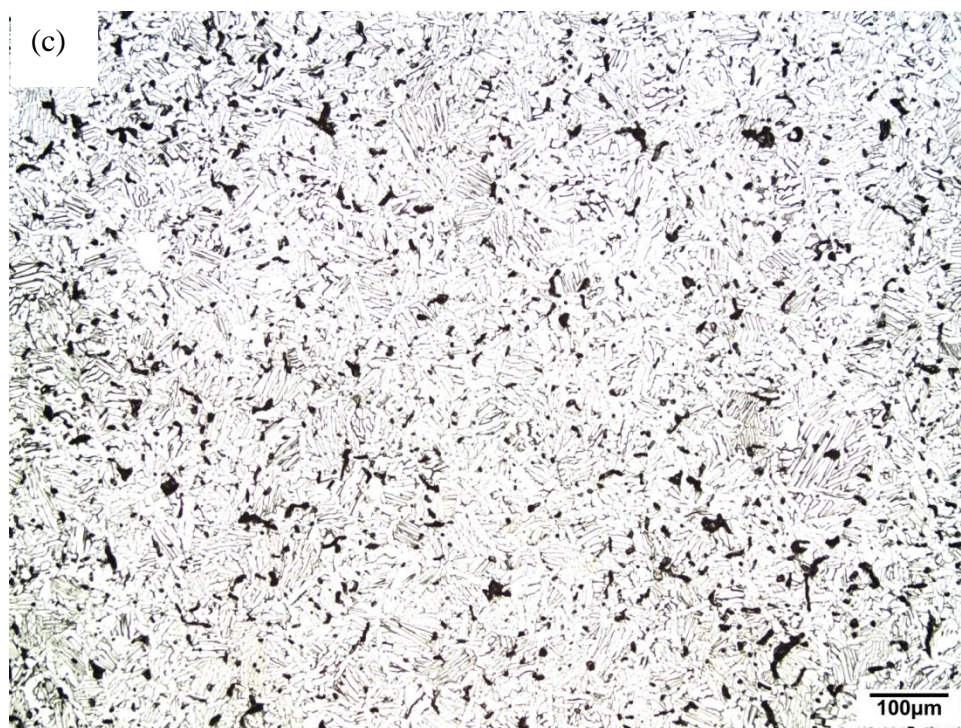


Figure 7.5 Continued





Figure 7.5 Continued



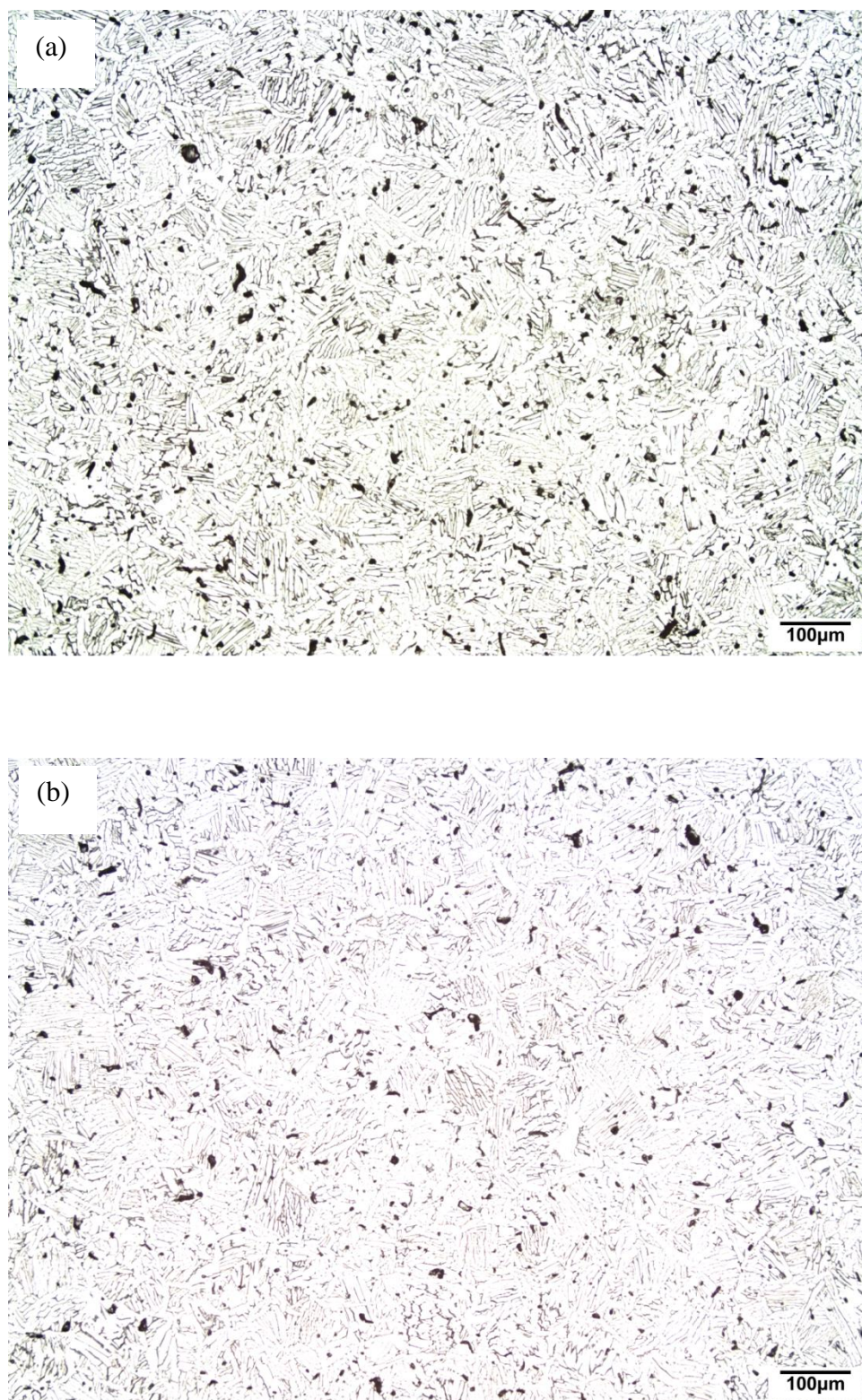


Figure 7.6 Microstructure of samples sintered through (a) isothermal (b) condition 1, and (c) condition 2 for 5.4 hrs



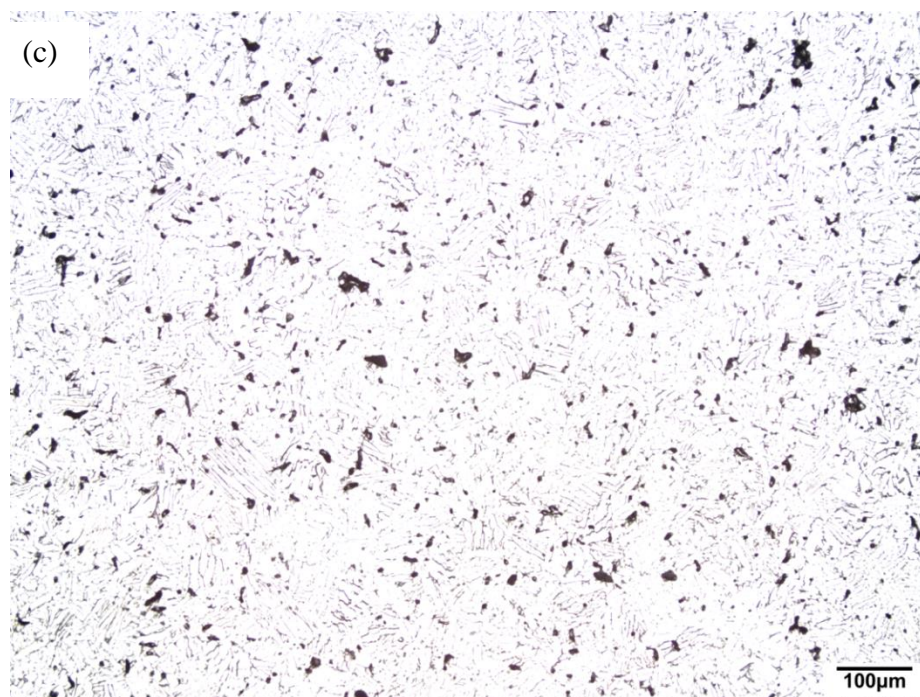


Figure 7.6 Continued

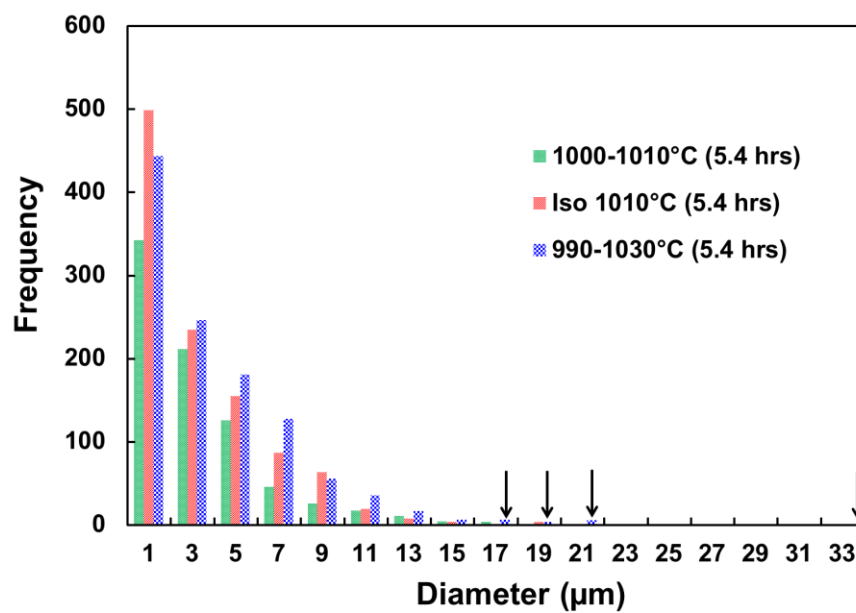


Figure 7.7 Frequency of occurrence of pores in microstructure. Arrows indicate the larger sizes of pores observed in 990-1030°C sintering

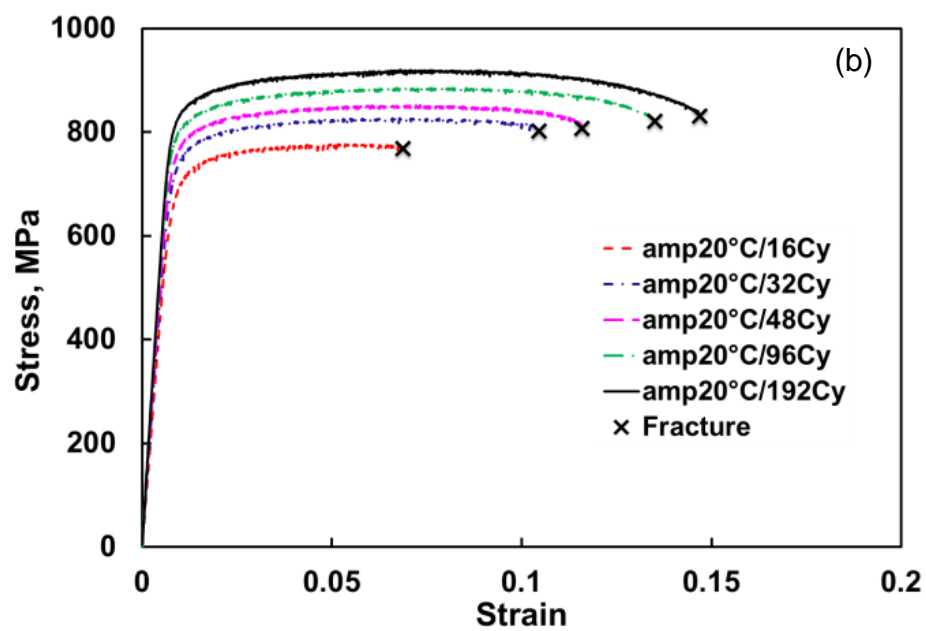
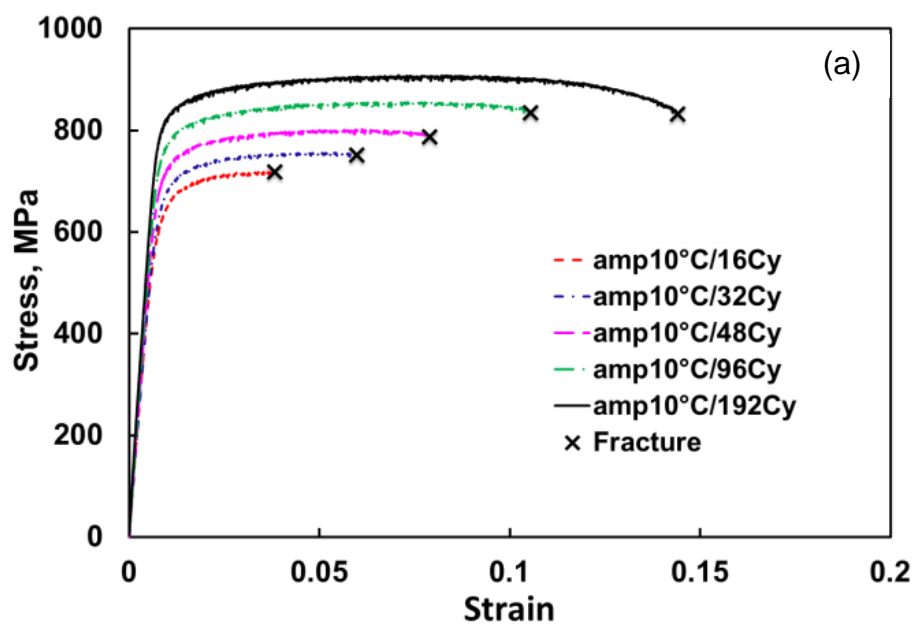


Figure 7.8 Stress-strain curves of PM Ti-6Al-4V alloy sintered following (a) condition 1 (b) condition 2 (c) isothermally at 1010°C

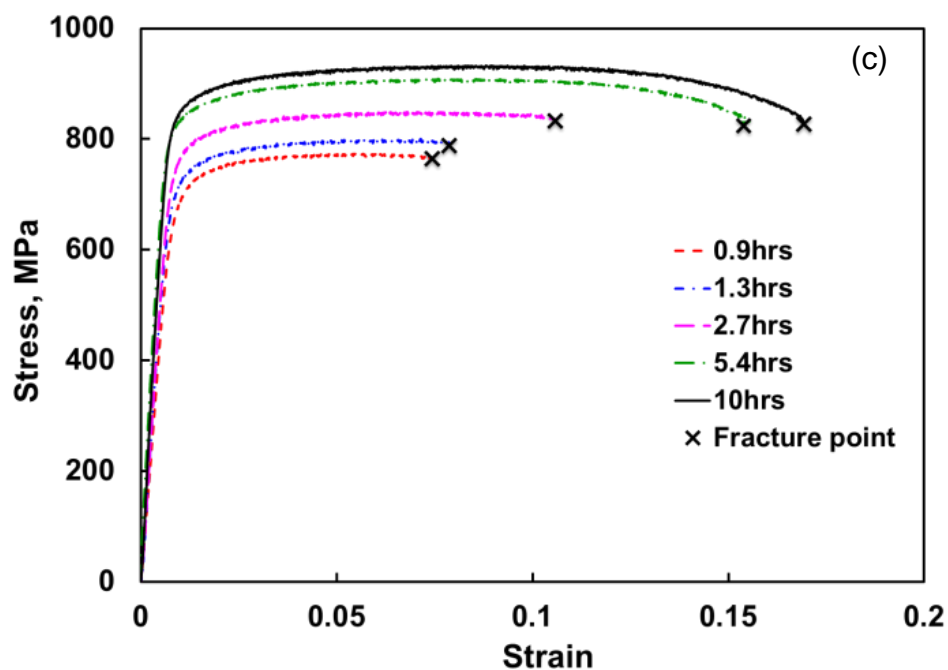


Figure 7.8 Continued

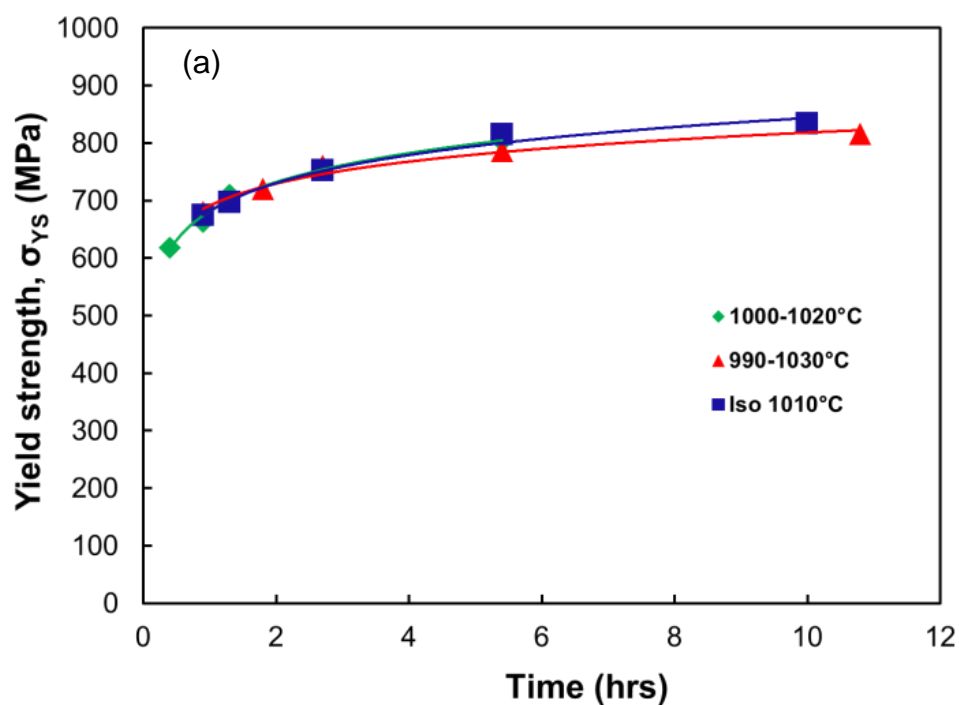


Figure 7.9 (a) through (c) show the variation of yield strength, tensile strength and % elongation as a function of total sintering time processed through isothermal and cyclic sintering conditions

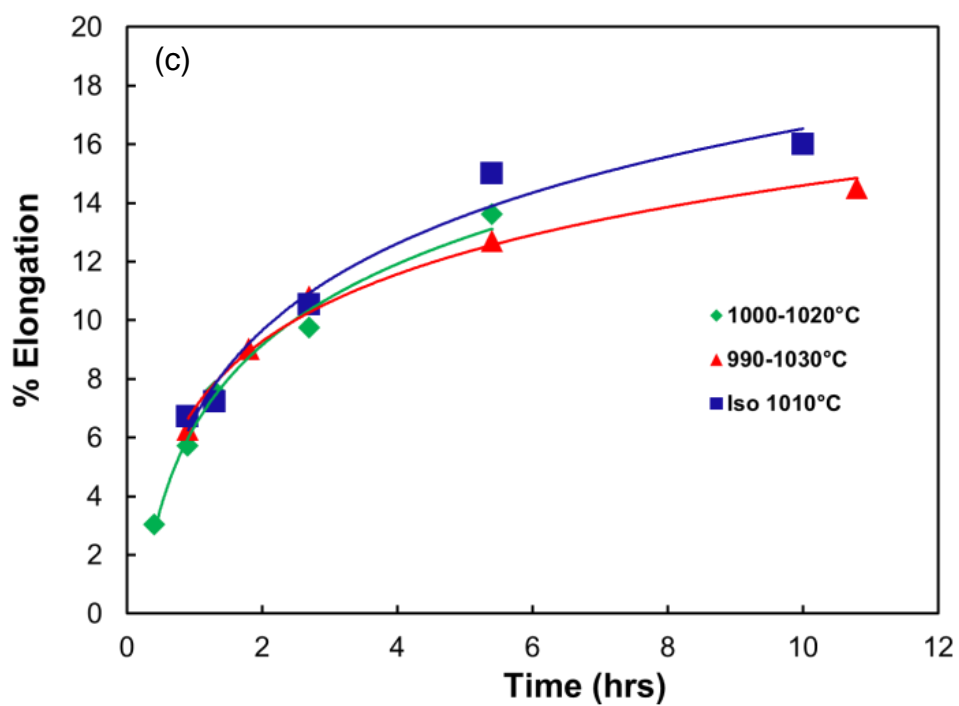
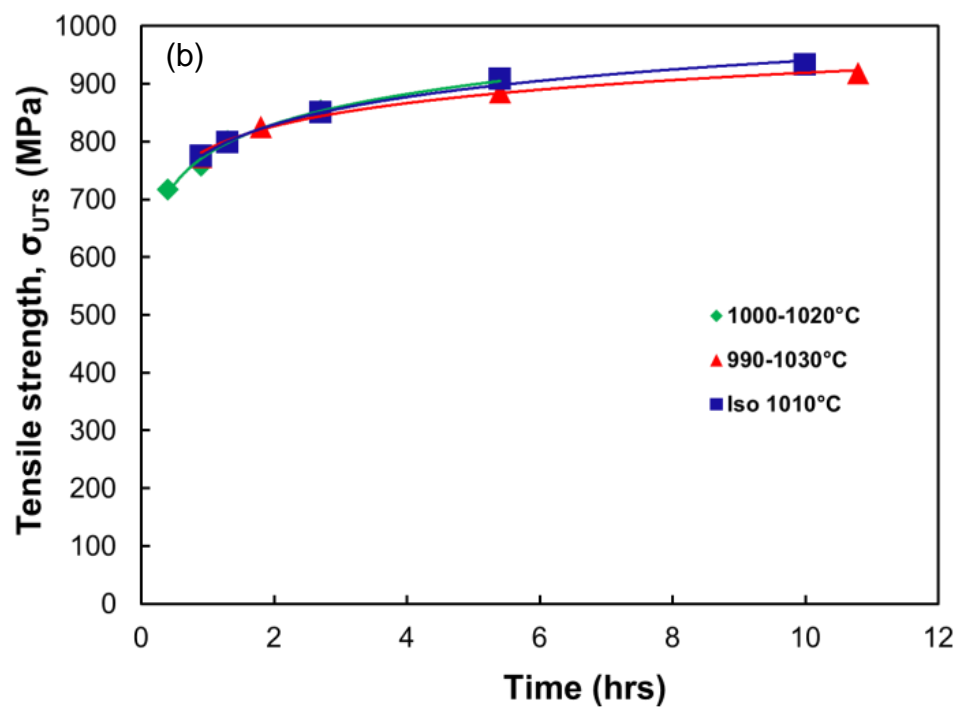


Figure 7.9 Continued

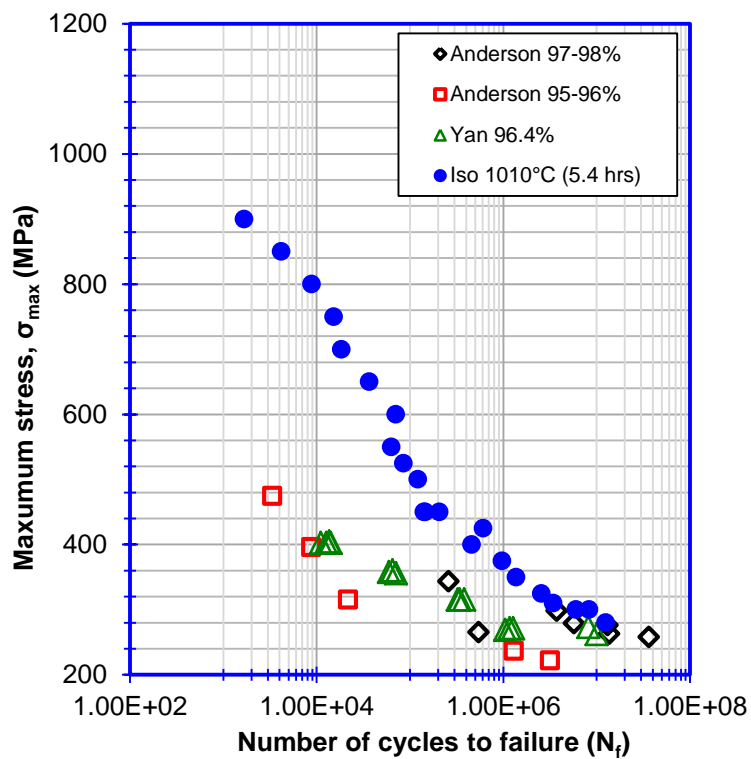


Figure 7.10 Comparison of S-N curve of PM Ti-6Al-4V alloy made by vacuum sintering of  $\text{TiH}_2$  at  $1010^\circ\text{C}$ , and by other vacuum-sintering processes

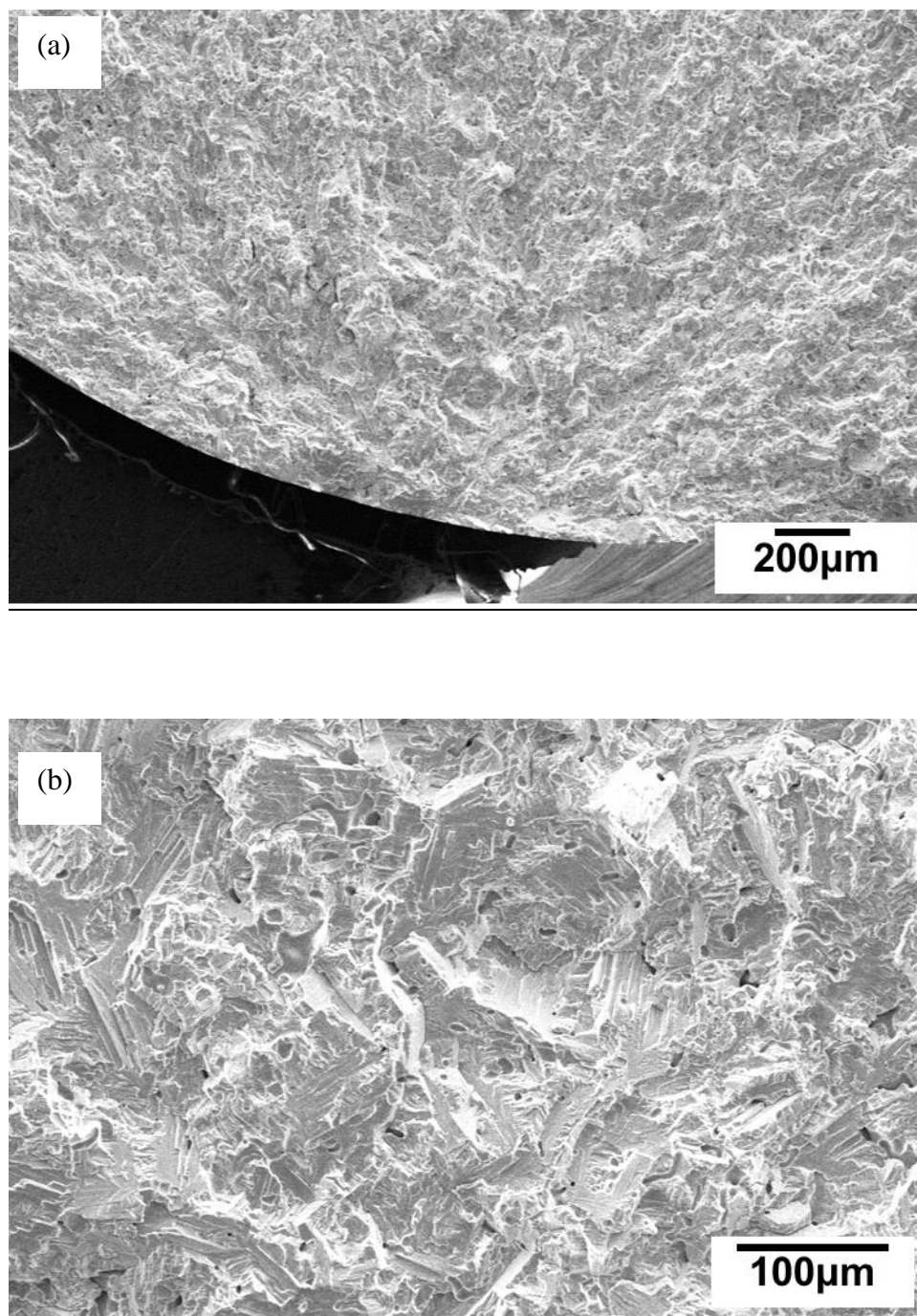


Figure 7.11 Fractographs of fatigue fracture at  $\sigma_{\max} = 425$  MPa,  $N_f = 6.05 \times 10^5$  cycles (a) whole view (b) higher magnification

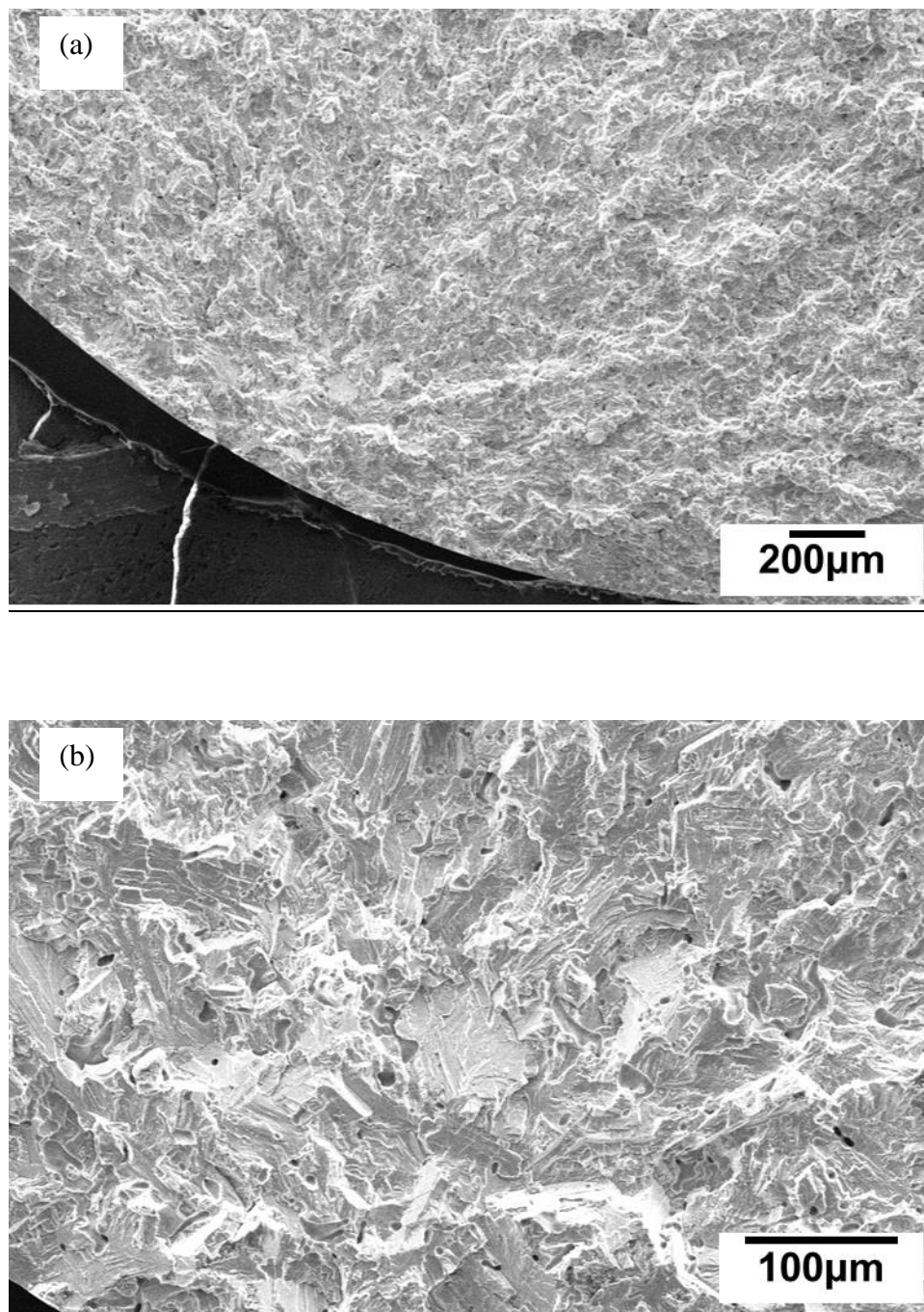


Figure 7.12 Fractographs of fatigue fracture at  $\sigma_{\max} = 550$  MPa,  $N_f = 6.2 \times 10^4$  cycles (a) whole view (b) higher magnification

## 7.5 References

- [1] J. Zhu, A. Kamiya, T. Yamada, W. Shi, K. Naganuma, Influence of boron addition on microstructure and mechanical properties of dental cast titanium alloys, *Mater. Sci. Eng. A.* 339 (2003) 53–62. doi:10.1016/S0921-5093(02)00102-8.
- [2] S. Tamirisakandala, R.B. Bhat, J.S. Tiley, D.B. Miracle, Grain refinement of cast titanium alloys via trace boron addition, *Scr. Mater.* 53 (2005) 1421–1426. doi:10.1016/j.scriptamat.2005.08.020.
- [3] F.H. Froes, S.J. Mashl, J.C. Hebeisen, V.S. Moxson, V. a. Duz, The technologies of titanium powder metallurgy, *Jom.* 56 (2004) 46–48. doi:10.1007/s11837-004-0252-x.
- [4] F.H. Froes, C. Suryanarayana, Powder Processing of Titanium Alloys, *Rev. Part. Mater.* 1 (1993) 223–275.
- [5] F.H. Froes, D. Eylon, Powder metallurgy of titanium alloys, *Int. Mater. Rev.* 35 (1990) 162–184. doi:10.1179/095066090790323984.
- [6] O.M. Ivasishin, D.G. Savvakina, F.H. Froes, V.S. Mokson, K. Bondareva, Synthesis of the Ti-6 Al-4 V alloy having low residual porosity by powder metallurgy method, *Poroshkovaya Metall.* 7 (2002) 54–64.
- [7] A. Carman, L.C. Zhang, O.M. Ivasishin, D.G. Savvakina, M.V. Matviychuk, E.V. Pereloma, Role of alloying elements in microstructure evolution and alloying elements behaviour during sintering of a near- $\beta$  titanium alloy, *Mater. Sci. Eng. A.* 528 (2011) 1686–1693. doi:10.1016/j.msea.2010.11.004.
- [8] O.M. Ivasishin, D.G. Savvakina, The Impact of Diffusion on Synthesis of High-Strength Titanium Alloys from Elemental Powder Blends, *Key Eng. Mater.* 436 (2010) 113–121. doi:10.4028/www.scientific.net/KEM.436.113.
- [9] V. V. Joshi, C. Lavender, V. Moxon, V. Duz, E. Nyberg, K.S. Weil, Development of Ti-6Al-4V and Ti-1Al-8V-5Fe Alloys Using Low-Cost TiH<sub>2</sub> Powder Feedstock, *J. Mater. Eng. Perform.* 22 (2013) 995–1003. doi:10.1007/s11665-012-0386-x.
- [10] M. Hagiwara, Y. Kaieda, Y. Kawabe, S. Miura, Fatigue Property Enhancement of .ALPHA.-.BETA. Titanium Alloys by Blended Elemental P/M Approach., *ISIJ Int.* 31 (1991) 922–930. doi:10.2355/isijinternational.31.922.
- [11] Y. Liu, L.F. Chen, H.P. Tang, C.T. Liu, B. Liu, B.Y. Huang, Design of powder metallurgy titanium alloys and composites, *Mater. Sci. Eng. A.* 418 (2006) 25–35. doi:10.1016/j.msea.2005.10.057.
- [12] F. Cao, K.S. Ravi Chandran, P. Kumar, P. Sun, Z. Zak Fang, M. Koopman, New



- Powder Metallurgical Approach to Achieve High Fatigue Strength in Ti-6Al-4V Alloy, *Metall. Mater. Trans. A.* (2016). doi:10.1007/s11661-016-3409-7.
- [13] N. Taylor, D.C. Dunand, A. Mortensen, Initial stage hot pressing of monosized Ti and 90% Ti-10% TiC powders, *Acta Metall. Mater.* 41 (1993) 955–965. doi:10.1016/0956-7151(93)90030-V.
  - [14] C. Schuh, P. Noël, D.C. Dunand, Enhanced densification of metal powders by transformation-mismatch plasticity, *Acta Mater.* 48 (2000) 1639–1653. doi:10.1016/S1359-6454(00)00018-5.
  - [15] C. Schuh, D.C. Dunand, Non-isothermal transformation-mismatch plasticity: modeling and experiments on Ti–6Al–4V, *Acta Mater.* 49 (2001) 199–210. doi:10.1016/S1359-6454(00)00318-9.
  - [16] Q. Li, E.Y. Chen, D.R. Bice, D.C. Dunand, Transformation Superplasticity of Cast Titanium and Ti-6Al-4V, *Metall. Mater. Trans. A.* 38 (2007) 44–53. doi:10.1007/s11661-006-9020-6.
  - [17] B. Ye, M.R. Matsen, D.C. Dunand, Enhanced densification of Ti–6Al–4V powders by transformation-mismatch plasticity, *Acta Mater.* 58 (2010) 3851–3859. doi:10.1016/j.actamat.2010.03.047.
  - [18] D.C. Dunand, C.M. Bedell, Transformation-mismatch superplasticity in reinforced and unreinforced titanium, *Acta Mater.* 44 (1996) 1063–1076. doi:10.1016/1359-6454(95)00224-3.
  - [19] S. Kohara, Effect of repeated allotropic transformation on sintering of iron powder, *Metall. Trans. A.* 7 (1976) 1239–1241. doi:10.1007/BF02656611.
  - [20] D. Leriche, E. Gautier, A. Simon, No Title, in: P. Lacombe, R. Tricot, G. Beranger (Eds.), *Sixth World Conf. Titan.*, Cannes, France, 1988: pp. 1295–1300. <http://classify.oclc.org/classify2/ClassifyDemo?owi=498207126>.
  - [21] H.H. Hausner, Proc. Int. Symposium on Reactivity of Solids, in: *Int. Symp. React. Solids*, Gothenburg, 1952: pp. 1951–1954.
  - [22] G. Cizeron, P. Lacombe, No Title, *Rev. Met.* 53 (1956) 819–830.
  - [23] R.A. Powell, F. Arsenal, Cycling sintering of Metals, in: *Prog. Powder Metall.* 1964, Frankford Arsenal, Philadelphia, 1964: pp. 139–144.
  - [24] B. Sarma, PhD Thesis, University of Utah, 2011.
  - [25] A. Seeger, The mechanisms of diffusion in metals and alloys, *J. Less Common Met.* 28 (1972) 387–418. doi:10.1016/0022-5088(72)90135-X.
  - [26] J.I. Qazi, J. Rahim, F.H. (SAM) Fores, O.N. Senkov, A. Genc, Phase

- transformations in Ti-6Al-4V-xH alloys, *Metall. Mater. Trans. A.* 32 (n.d.) 2453–2463. doi:10.1007/s11661-001-0035-8.
- [27] P. Sun, Z.Z. Fang, M. Koopman, J. Paramore, K.S.R. Chandran, Y. Ren, J. Lu, An experimental study of the (Ti–6Al–4V)–xH phase diagram using in situ synchrotron XRD and TGA/DSC techniques, *Acta Mater.* 84 (2015) 29–41. doi:10.1016/j.actamat.2014.10.045.
- [28] Y. Oshida, An Application of Superplasticity to Powder Metallurgy, *J. Japan Soc. Powder Metall.* (1975) 147–153.
- [29] O.A. Ruano, J. Wadsworth, O.D. Sherby, Enhanced densification of white cast iron powders by cyclic phase transformations under stress, *Metall. Trans. A.* 13 (n.d.) 355–361. doi:10.1007/BF02643344.
- [30] W. Szkliniarz, G. Smółka, Analysis of volume effects of phase transformation in titanium alloys, *J. Mater. Process. Technol.* 53 (1995) 413–422. doi:10.1016/0924-0136(95)01998-T.
- [31] C. Schuh, Contributions to transformation superplasticity of titanium from rigid particles and pressurized pores, *Scr. Mater.* 40 (1999) 1305–1312. doi:10.1016/S1359-6462(99)00068-8.
- [32] B. Sarma, K.S. Ravi Chandran, Accelerated kinetics of surface hardening by diffusion near phase transition temperature: Mechanism of growth of boride layers on titanium, *Acta Mater.* 59 (2011) 4216–4228. doi:10.1016/j.actamat.2011.03.046.
- [33] N. Chawla, X. Deng, Microstructure and mechanical behavior of porous sintered steels, *Mater. Sci. Eng. A.* 390 (2005) 98–112. doi:10.1016/j.msea.2004.08.046.
- [34] A. Hadrboletz, B. Weiss, Fatigue behaviour of iron based sintered material: a review, *Int. Mater. Rev.* 42 (1997) 1–44. doi:10.1179/imr.1997.42.1.1.
- [35] R. Haynes, A study of the effect of porosity content on the ductility of sintered metals, *Powder Metall.* 20 (1977) 17–20.
- [36] G.W. Mugica, D.O. Tovio, J.C. Cuyas, A.C. González, Effect of porosity on the tensile properties of low ductility aluminum alloys, *Mater. Res.* 7 (2004) 221–229. doi:10.1590/S1516-14392004000200002.
- [37] Y. Yan, G.L. Nash, P. Nash, Effect of density and pore morphology on fatigue properties of sintered Ti–6Al–4V, *Int. J. Fatigue.* 55 (2013) 81–91. doi:10.1016/j.ijfatigue.2013.05.015.
- [38] P. Kumar, K.S. Ravi Chandran, F. Cao, M. Koopman, Z.Z. Fang, The Nature of Tensile Ductility as Controlled by Extreme-Sized Pores in Powder Metallurgy Ti-6Al-4V Alloy, *Metall. Mater. Trans. A.* (2016). doi:10.1007/s11661-016-

3419-5.

- [39] P. Kumar, K.S. Ravi Chandran, A quantitative relationship to predict the effect of Extreme-sized pores on Tensile Ductility of Powder Metallurgy Ti-6Al-4V alloy, in: *Titanium-2015*, The Minerals, Metals and Materials Society, San Diego, CA, 2015.
- [40] R.J. Bourcier, D.A. Koss, R.E. Smelser, O. Richmond, The influence of porosity on the deformation and fracture of alloys, *Acta Metall.* 34 (1986) 2443–2453. doi:10.1016/0001-6160(86)90147-1.
- [41] P.J. Andersen, V.M. Svoiatytsky, F.H. Froes, Y. Mahajan, D. Eylon, Fracture behavior of blended elemental P/M titanium alloys, in: *Mod. Dev. Powder Metall.*, 1981: pp. 537–549.
- [42] M. Hagiwara, T. Kitaura, Y. Ono, T. Yuri, T. Ogata, O. Kanou, High Cycle Fatigue Properties of a Minor Boron-Modified Ti-6Al-4V Alloy, *Mater. Trans.* 53 (2012) 1486–1494. doi:10.2320/matertrans.M2012104.
- [43] A. Atrens, W. Hoffelner, T.. Duerig, J.. Allison, Subsurface crack initiation in high cycle fatigue in Ti6Al4V and in a typical martensitic stainless steel, *Scr. Metall.* 17 (1983) 601–606. doi:10.1016/0036-9748(83)90385-X.
- [44] X. Liu, C. Sun, Y. Hong, Effects of stress ratio on high-cycle and very-high-cycle fatigue behavior of a Ti-6Al-4V alloy, *Mater. Sci. Eng. A.* 622 (2015). doi:10.1016/j.msea.2014.09.115.
- [45] O.M. Ferri, T. Ebel, R. Bormann, The Influence of a Small Boron Addition on the Microstructure and Mechanical Properties of Ti-6Al-4V Fabricated by Metal Injection Moulding, *Adv. Eng. Mater.* 13 (2011) 436–447. doi:10.1002/adem.201000280.
- [46] F. Cao, P. Kumar, M. Koopman, C. Lin, Z.Z. Fang, K.S.R. Chandran, Understanding competing fatigue mechanisms in powder metallurgy Ti-6Al-4V alloy: Role of crack initiation and duality of fatigue response, *Mater. Sci. Eng. A.* 630 (2015) 139–145. doi:10.1016/j.msea.2015.02.028.

## **CHAPTER 8**

## **CONCLUSIONS**

Based on powder processing and sintering study, the following conclusions can be drawn:

1. Hydrogen sintering and phase transformation (HSPT) is a viable method to produce PM Ti-6Al-4V alloy with a tensile properties equivalent to that of wrought counter parts. Particularly, the tensile strength level of the alloy processed following HSPT process, exceeds the level of tensile strength that are typically found in wrought alloy.

2. Relatively high density can be achieved with finer starting powder, but increased oxygen contamination in finer particles drastically reduces the tensile ductility of the alloy. Thus, there is an optimum milling time for size reduction of powders to achieve acceptable level of tensile strength and ductility.

Analytical model developed based on stress concentration predicated the pore size effect on the tensile ductility of low porosity materials well with the experiments. Based on the experiment and modeling work, the specific conclusions are:

3. The largest size pore (extreme-sized pore) in test volume drastically reduces the ductility without affecting the tensile strength of the materials. The shape of the extreme-sized pore also seems to play unique role in reducing the tensile ductility of the materials.

4. A mechanism based on stress concentration is proposed to correlate the ductility of the material to extreme size pore. The study revealed that, variation in ductility as a function of pore size is depend on the strain hardening characteristic of the material.

Vacuum sintering close to the phase transition temperature resulted in densification similar to that obtained at relatively higher temperature. The specific conclusions that can be drawn are:

5. Density close to the theoretical density was achieved at temperature about 200°C lower than conventionally used. The increased density was attributed to the anomalously high diffusivity close to the phase transition temperature and the strain from the phase volume mismatch.

6. Tensile property comparable to wrought was achieved. A significant improvement in low to intermediate fatigue cycle relative to conventional PM Ti-6Al-4V alloy was shown. The improvement in fatigue was attributed to the reduction of large pores or clusters in the samples.